Australian Institute of Nuclear Science and Engineering

15th Australian Conference on Nuclear and Complementary Techniques of Analysis & 9th Vacuum Society of Australia Congress

The University of Melbourne
21st - 23rd November 2007

PROCEEDINGS

Australian Government
Australian Research Council

ThermoFisher SCIENTIFIC
The world leader in serving science

JAVAC — The Vacuum Specialists

JAVAC

SCREWLINE – Specifically developed for covering the requirements of industrial and difficult applications, the innovative and modular design of the SCREWLINE vacuum pumps is ideal in all cases where reliable, compact and low maintenance vacuum technology is demanded. They are suited for all applications with high requirements regarding the backing pump, like processes involving particles or in rough everyday production.

The SCREWLINE pumps offer numerous advantages to the user:

- Minimum downtimes, maximum availability, highly rugged
- Low cost of ownership
- Long maintenance intervals and low servicing complexity
- Highly flexible
- High pumping speed at low ultimate pressure
- Excellent suitability for the short cycles of load lock chambers or similar applications.

SCREWLINE — The Dry Vacuum Solution

SOGEVAC Rotary Vane Vacuum Pumps

Many years of experience in vacuum engineering and the latest developments in pump technology combine in the SOGEVAC range the capability to adapt to the requirements of both the industry and the environment. The comprehensive range (pumping speeds ranging from 10 to 1200 $m^3 \times h^{-1}$ (5.8 to 707 cfm)) allows every customer to select the right pump for their particular needs.

- Continuous operation from atmospheric pressure to ultimate pressure
- Low noise level
- Low vibrations
- Integrated exhaust filter, better than 99.9% efficient
- High water vapour tolerance

Sogevac Prices Reduced By a Further 30%

Sogevac SV65B – Compact, Quiet & Robust

Sogevac — World Renowned Industrial Products

... Now A Cost Effective Solution for Every Application

For more information visit www.javac.com.au

or Free Call 1300 786 771

Quality Endorsed Company

SIIS STANTON SCIENTIFIC SIIS

Vacuum Science Products

A & N Vacuum components
meeting all international standard specifications. CF, ISO, KF, ASA and other conventions in the broadest of configurations, Custom Chambers

Aalborg Mass Flow Meters and Controllers

Electron Multipliers and Channeltron Detectors

ADVANCED ENERGY
Power Supplies RF and DC
for Thin film deposition, also components and Networks for Plasma loads

ADVANCED ENERGY®

Ion sources and Magnetron sources
For Thin Film, Surface Science and sample preparation applications

Ceramaseal
A division of CeramTec

HV and UHV feedthroughs
Ceramaseal as used by major instrumentation companies and world class research projects alike

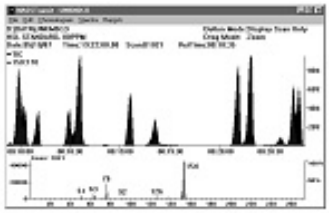

RHK Technology
Imaging the Future of Nanoscience

Granville Phillips Vacuum Gauges

Thickness Monitors Quartz Crystal monitoring systems 0.1 Angstrom resolution. Piezo electric valves

Mass Spectral data bases N.I.S.T. (USA) and Wiley Mass Spectral Library

SIMION Ion Optics Software

PHYSICAL ELECTRONICS

Diener Plasma Systems

Ion Pumps from Gamma Vacuum

Electron Guns and Power Supplies from TFI Telemark an established standard in the Field of *Vacuum Deposition* Processes

SPECS®

Surface ScienceSystems & Components

www.stantonscientific.com email : bill@stantonscientific.com

Ph. 02 66856902 Fax 02 66858530

AP Instruments Pty Ltd

Andre Peters ***33 Hunter Ave St Ives 2075 NSW***
02 91446600 0448 750 885 andrepeters@optusnet.com.au

PREVAC *www.prevac.eu*

- Ultra High Vacuum and High Vacuum System
- Manipulators, Goniometers and Mechanical Feedthroughs
- Chambers and Mechanisms
- Sample Holders
- X-Ray , Electron, Ion sources
- **Accessories**
  Bakeout equipment, Load locks, Vacuum doors, Mass flow controllers, Water cooling devices, vacuum fittings, Titanium sublimation pumps etc.
- Eelectronics

Pressure measurements, Stepping motors controls, Emission regulators, Electron beam evaporator PS, Electron and Ion source PS, Bakeout control units. etc

- Software

TOF acquisition applications, Space simulator control appl. , Dedicated software for Customer's systems and devices, Pressure control appl. , Thermal desorption Spectroscopy Control, Automatisation of sample transfers, etc.

TOYAMA www.toyama-jp.com

Synchrotron Radiation (SR) Beam Line and Related Systems

Total Beam Line Systems
Branch Beam Shutters
Absorbers
Mirror Positioning Systems(3-7 axes,Bent type)
Monochromators(VUV,Soft X-ray,Photoelectron)
Analysis Instruments
Beam Monitors
Beam Ducts
Slits
Pumping Units for Vacuums

Particle Accelerators and Related Devices

Magnets(Bending,Quadrupole,Multipole,Steering,etc.)
Monitors(Profile Monitors,Core Monitors,Current Monitors,etc.)
Ion Sources
Electron Guns
Infectors,Deflectors
Accelerating Electrodes
Beam Ducts
Pumping Units for Vacuums
Analyzers

Other Systems and Components

Experiment Systems and Instruments for Space Development,
Condensed Matter Physics and Electrical Engineerings

Systems and Instruments for Nuclear Fusion and Nuclear Engineering

Ion Source Drawing Electrodes
Calibration Spectroscopes for Plasma
Measuring Instruments
High-Frequency Antennas for Plasma Heating
Beam Dumps
Fixed/Movable Limiters
Calorimeters
Collimators
Manipulator Tongs

Vacuum Experiment Systems and Instruments

Vacuum Chambers(Low to Ultra-High Vacuum(LV-UHV) in various configurations for all types of applications)
Instruments for Plasma Experiments
Pumping Units for Vacuums

Various Parts & Components for Vacuum Experiments

Fittings
Feed Throughs
Linear/Rotary Motion Drivers,Linear Motion Thimbles
Magnet Couplings,Manipulators
Current Conductors,Electrical Isolators;
Goniometers

25% Discount*

Great VG Scienta Discounts

Up to 25% discount on selected vacuum components

VG Scienta are offering up to 25% discount on selected vacuum components for all ThermoFisher customers.

Discounted components include;

- all metal / viton right angle valves
- pumped rotary feedthroughs
- linear drives
- leak valves
- mechanical hands
- magnetic probes
- high power magnetic probes
- rack & pinion drives
- viewports
- wobble sticks

and more!

For full details of this offer and further information on VG Scienta's range of quality HV & UHV components, please contact ThermoFisher directly or visit www.vgscienta.com.

Thermo Fisher Scientific
Unit 14, 38-46 South Street
Rydalmere, NSW 2116, Australia

Dominic Gomez
Tel: +61 2 8844 9500
Mobile: +61 411 676 007
Fax: +61 2 8844 9599
Email: dominic.gomez@thermofisher.com

Andre Peters
Tel: +61 2 8844 9500
Mobile: +61 448 750 885
Fax: +61 2 8844 9599
Email: andre.peters@thermofisher.com

* selected products until 31st December 2007

VG Scienta brings over 40 years' experience, innovation and expertise in providing UHV components and high performance instruments for surface science.

Maunsell Road, Castleham Industrial Estate, Hastings TN38 9NN, UK
Phone: +44 (0) 1424 851 291 Fax +44 (0) 1424 851 489
E-mail: sales@vgscienta.com Web: www.vgscienta.com

VG SCIENTA
a gammadata company

scitek
australia

Scitek Australia Pty Ltd was originally called Balzers Australia. We changed our name six years ago after changes to our parent organization. In keeping with our policy for providing quality products and services, we have aligned our organization with the world's leading names of the industry that is involved in the vacuum industry.

Scitek is "your partner in Vacuum!"

Our Products and Services

Sales

Vacuum pumps
Vacuum measurements
Gauges and Leak Detectors
Mass Spectrometers
Thin Film Coatings
Valves
HV and UHV Components
Field portable GCMS
Portable Explosive Detection
RAC charging/testing equipment
Fast cycle water vapour cryo pumps

Service

In-house Services:
Mass spectrometers (incl. calibration)
Turbo molecular pumps
Vacuum gauge heads
Leak detectors
Gas analyzers
Hapsites

Onsite Services:
Trouble shooting on vacuum systems
Vacuum leak detection with Helium
Onsite Training

Parts
Parts available on all of our products.

For more details

CALL
1800 023 467

EVAC
Quick Release Flange Coupling

UMICORE
Evaporation & Sputtering Materials

Austin Scientific
Cryo Pumps

Pfeiffer Vacuum
High Vacuum pumps, Mass Spectrometer, Leak detectors,

VAT Vacuum Valves
Vacuum Valves

Advanced Research Systems

Suite 1B, 10-18 Cliff Street
Milsons Point
Sydney NSW 2061

PO BOX:
355 Milsons Point
Sydney NSW 1565

Toll Free : 1800 023 467
Phone : 02 9954 1925
Fax : 02 9954 1939
E-mail : contact@scitek.com.au
Web : www.scitek.com.au

scitek
australia

Program
Tuesday 20th November 2007

16:30 - 18:30	Registration
17:30 - 19:30	Welcome and light refreshments

Wednesday 21st November 2007

		Page
08:15 - 09:15	Registration	
09:15 - 09:40	Welcome	
Session 1	**Environment and Bioscience (1)** **Chair: Jeff McCallum**	
09:40 -10:20	David Paterson, Australian Synchrotron Microanalysis capabilities of the microspectroscopy beamline at the Australian Synchrotron	16
10:20 - 10:40	Samuel Marx, University of Queensland Evidence of enhanced El Niño activity in the mid Holocene inferred from records of Australian dust deposition in New Zealand.	18
10:40 - 11:00	Dora Pearce, University of Ballarat Toenails: they know where you've been!	22
11:00 - 11:30	Morning Tea	
Session 2	**Advanced Materials and Analysis** **Chair: Rob Elliman**	
11:30 - 12:00	Daniel Riley, University of Melbourne Use of ultra-fast diffraction in the design of novel materials	28
12:00 - 12:20	Imam Kambali, University of Newcastle Determination of hydrogen adsorption site on palladium(100) using low energy ion scattering spectroscopy	34
12:20 - 12:40	Babs Fairchild, University of Melbourne Fabrication of sub micron layers in single-crystal diamond	37
12:40 - 13:10	Claudia Schnohr, Australian National University Comparison of the atomic structure in InP amorphised by electronic or nuclear ion-energy-loss processes	38
13:10 - 14:30	Lunch	
Session 3	**Environment, Bioscience (2) and Nanotechnology (1)** **Chair: Peter Johnston**	
14:30 - 15:00	Paul Pigram, Latrobe University Detecting oligonucleotide immobilization and hybridisation using TOF-SIMS	43
15:00 - 15:20	Robert Haworth, University of New England Blending lead-210 and AMS age profiles from estuarine sediment cores to reconstruct Holocene climate change in the Sydney Region	44

15:20 - 15:40	Andreas Markwitz, GNS Low energy lead implantation into Si for novel group IV nanomaterials	47
15:40 - 16:00	Michael Gladys, University of Newcastle Bridging the gap between the nano-particle and single crystal surface science	51
16:00 - 16:30	Paul Munroe, University of NSW Application of focused ion beam systems to materials analysis	54
16.30 – 18.30	**Poster Session 1** and Afternoon Tea	
18:00 onwards	BBQ	

Thursday 22nd November 2007

Session 4	**Environment and Bioscience (3)** **Chair: David Cohen**	
09:00 - 09:30	James Robertson, AFP Nuclear science and forensic science - complementary sciences!	58
09:30 - 09:50	Serena Abbondante, University of Canberra Radiologically contaminated evidence: extraction procedures and the effect of radioactive materials on forensic DNA profiling	59
09:50 - 10:10	Laura Gladkis, ADFA@UNSW A new methodology in prosthesis research: radioisotope tracing of knee implant wear	61
10:10 - 10:30	Amy Ziebell, University of Wollongong Cylindrical silicon-on-insulator microdosimeter: charge collection characteristics	66
10:30 - 11:00	Julian Adams, Australian Synchrotron Protein crystallography using the Australian Synchrotron	69
11:00 - 11:30	Morning Tea	
Session 5	**Nanotechnology (2)** **Chair: Andreas Markwitz**	
11:30 - 12:00	Matt Kilburn, University of Western Australia NanoSIMS: Recent advances and new applications in SIMS	69
12:00 - 12:20	Damian Carder, GNS Ion-beam sputtered germanium thin films – self-assembly of surface nanostructure using post growth annealing	70
12:20 - 12:40	Michael Dunn, University of Melbourne Interface trap density reduction in thin silicon oxides using ion Implantation	74
12:40 - 13:00	Dinesh Venkatachalam, RMIT Surface fraction statistics of gold nanoclusters of dissimilar sizes determined by RBS	78

13:00 - 13:30	Rob Elliman, Australian National University Photonic nanostructures and their influence on Er luminescence	82
13:30 - 14:30	Lunch	
14:30 – 18:30	**Conference Tour of Synchrotron**	
19:00 - 22:30	**Conference Dinner at Treetops Restaurant, Melbourne Museum**	

Friday 23rd November 2007

09:00	**Session 6: Advanced Materials, Devices and Analysis** **Chair: Chris Ryan**	
09:00 - 09:30	John Kennedy, GNS Unravelling the mystery of zinc oxide	86
09:30 - 09:50	Julius Orwa, University of Melbourne Towards a formula for optimized production of single NV centres in diamond by ion implantation	90
09:50 - 10:10	Kane O'Donnell, University of Newcastle Neutral atom microscopy: a non-destructive, high-resolution surface analysis technique	90
10:10 - 10:30	Andrew Baloglow, University of Wollongong Characterization of silicon detectors utilized in an on-line dosimetry system for microbeam radiation therapy	91
10:30 - 10:50	Perry Davy, GNS Diffusion characteristics of silicon implanted with group IV elements	95
10:50 - 11:20	Rachel Caruso, University of Melbourne Porous titanium dioxide materials fabricated by using templating techniques	98
11:10 - 11:30	Morning Tea	
11:30 -13:00	**Poster Session 2**	
13:00 - 14:00	Lunch	
14:00 - 16:30	**Session 7: Ion Beam Science and Advances in Analysis** **Chair: David Jamieson**	
14:00 - 14:30	John O'Connor, University of Newcastle Helium ion microscope – high resolution, high contrast microscopy for nanotechnology	100

14:30 - 14:50	Chris Ryan, CSIRO Next generation x-ray microspectroscopy: towards full-spectral XANES and high throughput fluorescence imaging using massively parallel detector arrays and realtime spectral deconvolution	101
14:50 - 15:10	Michael Went, Australian National University Extended interface analysis using high energy electron scattering	105
15:10 - 15:30	Changyi Yang, University of Melbourne Avalanche detector technology for keV single ion detection and implantation for quantum bits construction	109
15:30 - 15:50	David Cohen, ANSTO Towards a better understanding and prediction of the bremsstrahlung background in PIXE spectra	112
15:50 – 16:10	Andrew Gleadow, University of Melbourne Fully-automated counting of fission tracks in natural minerals for fission track dating and thermochronology	117
16:10 - 16:40	David Belton, CSIRO PIXE imaging of a developing corrosion front beneath a protective coating on galvanized steel	120

16:40 - 17:00 Closing Remarks and Award of Prizes

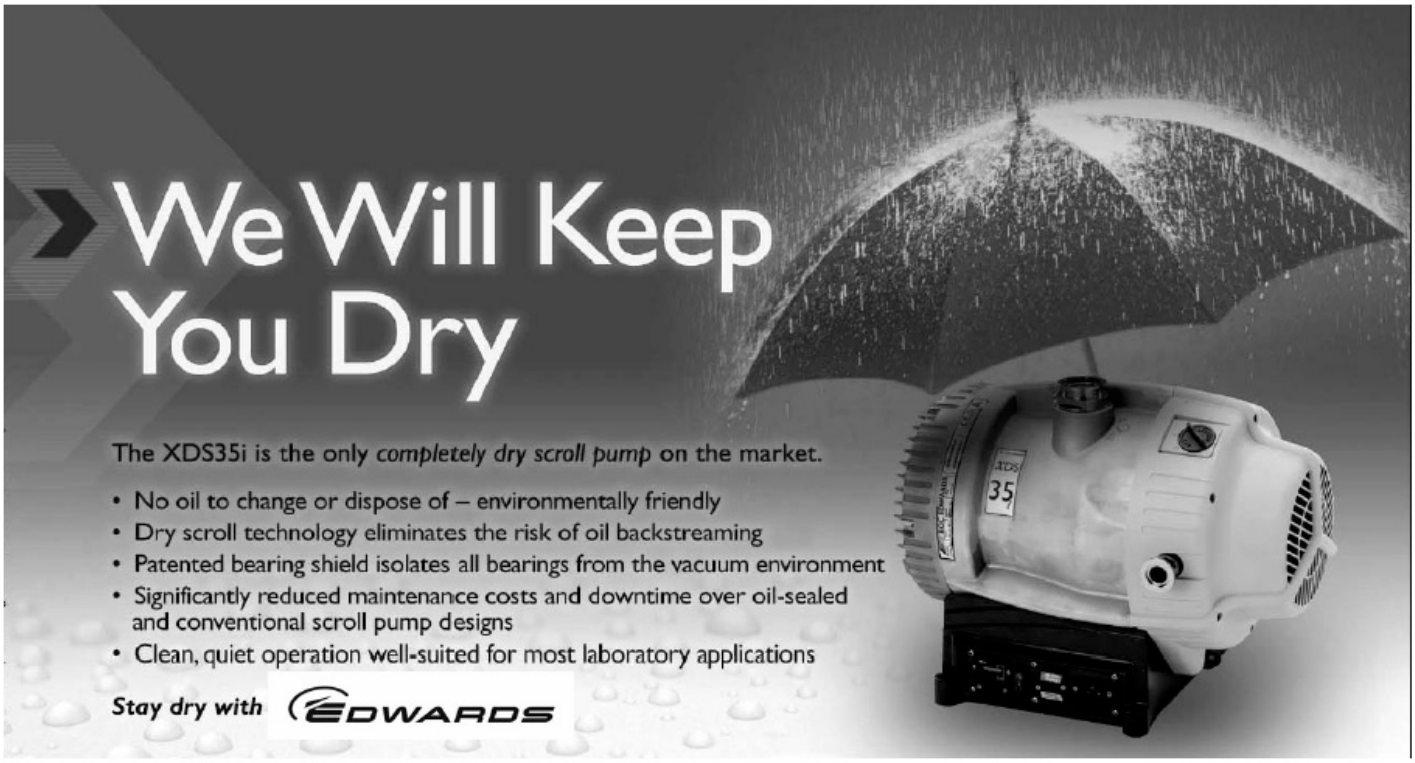

AVT Services Pty Limited
ABN 34 056 503 461 ACN 056 503 461
Vacuum & Cryogenics

To arrange a FREE demo please contact:
AVT Services
Sydney – Melbourne – Brisbane
Perth – Adelaide
Free call: 1800 55 99 88
Email: info@avtservices.com.au

Posters index

Microanalysis capabilities of the microspectroscopy beamline at the Australian Synchrotron

D. Paterson
Australian Synchrotron, Clayton VIC, Australia

Introduction

This highly specialised beamline at the Australian Synchrotron [1] will provide sub-micron spatial resolution with the highest flux possible and an energy tuning range of 4.5–25 keV using an in-vacuum undulator source. It will combine 2D mapping with μ-XRF, μ-XANES and μ-XAFS for elemental and chemical microanalysis to solve problems requiring micron and sub-micron resolutions.

Performance goals and design

The primary beamline goal is to achieve sub-micron spatial resolution, 100–200 nm, at energy resolutions approaching 1/10,000 [2]. This spatial resolution will be achieved without compromising flux, as the beamline will simultaneously achieve detection sensitivities to sub-ppm levels. The beamline will have the flexibility to trade-off one parameter against gains in certain attributes, as dictated by the application. For example, gains in sensitivity will be achieved for certain fluorescence applications by reduced spatial and/or energy resolution. Options for trading flux and spatial resolution will include swapping between Fresnel zone plates and Kirkpatrick-Baez (KB) mirrors see Figure 1. Fresnel zone plates are intended for the highest resolution applications, while the KB mirrors shall be used for applications where achromatic focusing and highest sensitivity are required.

Microanalysis capabilities

The beamline will accommodate a diverse range of materials, environmental and biological science applications with greatly contrasting sample formats, sample composition and anticipated detector count rates. Many applications, such as cell biology, medicine and plant biology, will tend to have samples with a low areal density and adequate sensitivity will be attained by the highest possible photon fluxes. In some cases high flux will be attained without compromising the desired spatial resolution by lowering the incident energy resolution.

Detectors

State-of-the-art detectors will be used including a new spectroscopy detector system under development by BNL and CSIRO that combines a large planar silicon detector array, custom pulse-processing, and a pipelined, parallel processor with embedded dynamic analysis image projection [3]. A feasibility and design study has been completed for a 384 element detector which aims at large solid-angle, close coupling to stage control and count-rates approaching 10^8 events/second, with full real-time processing and deconvoluted image projection [4].

Conclusions

The Microspectroscopy Beamline will commence operation in mid 2008. The anticipated performance of the beamline will be presented and some research applications relevant to the Australian research and microanalysis communities will be discussed.

References

[1] See http://www.synchrotron.vic.gov.au

[2] J. Boldeman, C. Ryan and D. Cohen. Conceptual Design for the High Performance Microspectroscopy Beamline 9 on the Australian Synchrotron, ANSTO External Report E-759, ISBN No 1 920791 07 8, September 2005.

[3] C.G. Ryan, "Quantitative Trace Element Imaging using PIXE and the Nuclear Microprobe", Int. J. Imaging Systems and Technology, 11 (2000) 219-230.

[4] D. P. Siddons, A. Dragone, G. De Geronimo, A. Kuczewski, J. Kuczewski, P. O'Connor, Z. Li, C. G. Ryan, G. Moorhead, R. Kirkham, P. Dunn, "A High-speed Detector System for X-ray Fluorescence Microprobes", proc. of the 2006 IEEE Nuclear Science Symposium, Medical Imaging Conference and Room Temperature Semiconductor Detector Workshop, San Diego,OcOctober 29 - November 4, 2006.

Figures

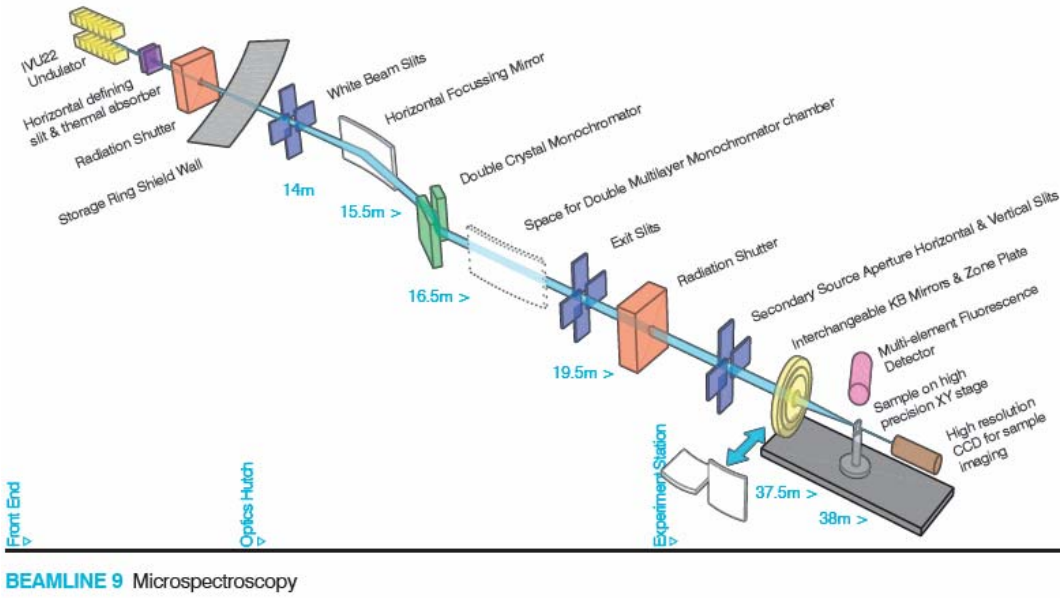

Fig. 1. Conceptual layout of the Microspectroscopy Beamline at the Australian Synchrotron

Evidence of enhanced El Niño activity in the mid Holocene inferred from records of Australian dust deposition in New Zealand

Samuel K. Marx [a], Hamish A. McGowan [a] and Balz S. Kamber [b]

[a] *School of Geography, Planning and Architecture, The University of Queensland, St Lucia, Brisbane, Qld, 4072, Australia*

[b] *Department of Earth Sciences, Laurentian University, Sudbury, Ontario, P3E2C6, Canada*

Introduction

Rates of mineral dust deposition act as a sensitive proxy of palaeo-climate because dust emissions respond rapidly to changes in source area conditions, such as drought. In Australia the occurrence of dust storms has been found to be controlled largely by rainfall and soil moisture (McTainsh et al., 1998). Up to 40% of annual rainfall variability in northern and eastern Australia is linked to ENSO (El Niño Southern Oscillation) cycles (McBride and Nickolls, 1983). As a result, increased erosion and dust events occur during dry El Niño phases of the Southern Oscillation, while these are suppressed during wet La Niña phases when the activity of the Australian summer monsoon is enhanced. In New Zealand, Australian dust has been reported being deposited on numerous occasions over the last 100 years, typically following prolonged drought episodes associated with ENSO events (Marx and McGowan, 2005). Therefore, it was hypothesised that chronologies of Australian dust deposition in New Zealand would serve as a measure of climate, and in particular ENSO, variability through time. In this study we present a 7000 year record of Australian dust deposition in New Zealand. Changes in the rates of dust deposition through time are used to map ENSO-type variability in the climate of the Australian region over this period.

Method

A 60cm peat core was extracted from an ombrotrophic (rainfall fed) peat bog located on the ridge crest of the Old Man Range, Central Otago, South Island, New Zealand.

The core was dissected at 2 mm intervals. A sub-sample of each section was ashed in a high temperature oven; this had the effect of destroying the organic (peat) component, while the mineral (dust) component was retained. The trace element content of the mineral component of 27 samples was then analysed for 44 elements by ICP-MS according to the procedure of Marx et al. (2005a). Samples of the organic peat from various depths through the core were dated by ^{14}C AMS at the ANTARES laboratories, ANSTO.

The source area provenance of the dust samples deposited in the core was established using the method of Marx et al. (2005b). This method compares the trace element chemistry of the dust with that of potential source sediments. The closer the chemistry of the dust to that of a particular source area sediment, the more likely it is that the source area sediment is the source of the dust (Fig. 1).

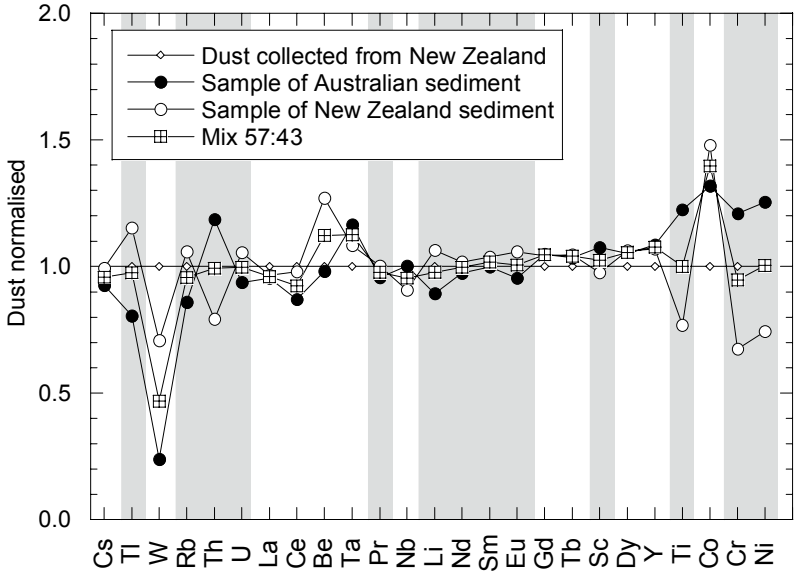

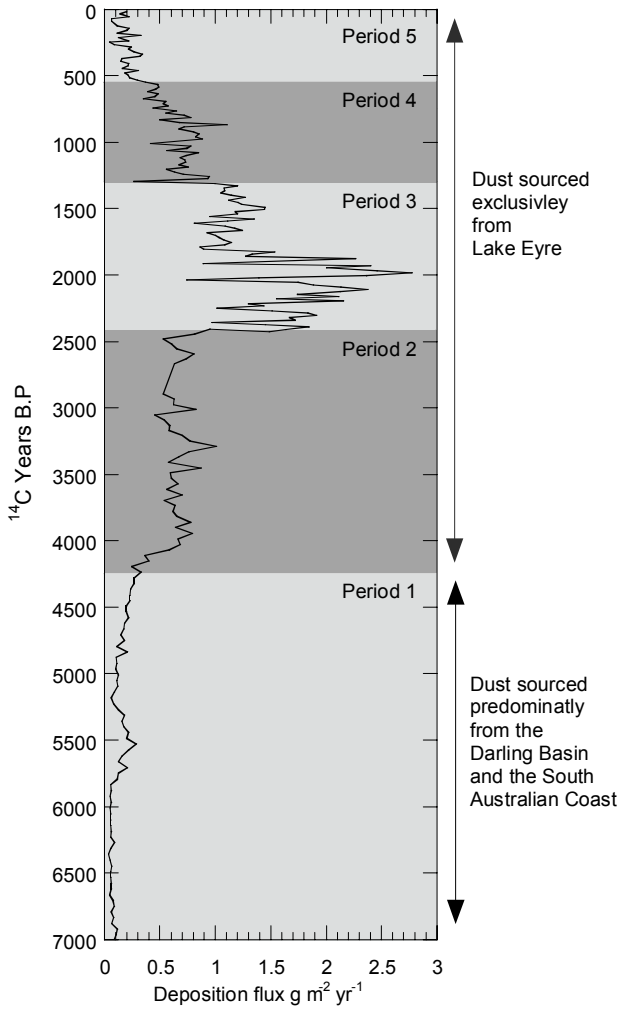

Fig. 2. Australian dust deposition rates recorded in New Zealand.

This figure shows an example of the provenance method. Potential dust source sediments are shown normalised against a dust sample (shown by the straight line). The chemistry of the Australian sediment more closely resembles the dust than the sediment from New Zealand and this indicates that it is more likely to be the source of the dust. The abundance of many elements in the dust however, is in between that of the two potential source sediment samples (shown by the shaded bars). This implies that the dust may be a mixture of these different source areas. Mixing the two sediments therefore gives a better approximation of the dust chemistry than either sediment singularly (shown by the crossed squares). In this example, a mixture of 57% Australian sediment and 43% New Zealand sediment was found most likely to be the source of the dust. By this approach the contribution of up to 3 different source sediments could be determined for a given sample.

An extensive 'library' of potential dust source sediments was collected widely from within known dust source areas in Australia, such as the Lake Eyre Basin and the Murray-Darling Basin. Similarly, samples of New Zealand sediments were collected from loess and alluvial deposits for comparison with the dust samples extracted from the core.

Results

The Australian dust record through the core is shown in Fig. 2. Five distinctive periods of dust deposition were identified through the core: 1) low deposition, averaging 0.142 g m^{-2} yr^{-1} occurred from the bottom of the core, 7000 B.P, until 4200 B.P when Australian dust deposition increased four fold to 0.58 g m^{-2} yr^{-1}; 2) this rate continued through to 2400 B.P when dust deposition again rose markedly, averaging 1.56 g m^{-2} yr^{-1}; 3) high dust deposition continued through to approximately 1300 B.P., where deposition rates fell to levels similar to those recorded during period 2; 5) from 700 B.P. to the present dust deposition decreased significantly, approaching the rates recorded during period 1 from 7000-4200 B.P.

Discussion and conclusions

During the period between 7000-4200 B.P. (period 1) Australian dust in the core showed the most varied provenance, with dust sourced from regions in southern South Australia, the Murray-Darling Basin, and the Lake Eyre Basin. From 4200 B.P. to the present, dust was provenanced almost exclusively from the Lake Eyre Basin, particularly Lake Eyre itself. Comparison with other palaeo-environmental records shows that Lake Eyre was in a lacustral (wet) phase from 12000 B.P. through to 4000 B.P. (Gillespie et al., 1991; Magee et al., 2004). This was caused by extended La Niña type conditions resulting in an enhanced Australian monsoon and regular flow along the Channel Country Rivers which feed Lake Eyre. Consequently, Lake Eyre was too wet to act as a dust source at this time, so dust was sourced from other regions in Australia.

After 4000 B.P. the hydrology of Lake Eyre changed and the lake entered its modern ephemeral phase (Magee et al., 2004). Climate records from around the globe suggest that El Niño-type conditions began at this time, suggesting climate was more variable. Following this change in conditions, dust provenance in the core switched almost exclusively to Lake Eyre as the Lake became dry for long periods and switched on as a dust source.

At 2400 B.P. (period 3) the climate again changed significantly, evidenced by increased dust flux. We believe the increase in dust flux at this time was driven by extreme oscillations between La Niña and El Niño conditions. During La Niña conditions Lake Eyre would fill and supplies of fine sediment would be deposited on the lake bed. A switch to El Niño conditions would result in drying of the lake, during which these sediments became available for aeolian entrainment. This is supported by Coral $\delta^{18}O$ records of precipitation (interpreted as ENSO) at Christmas Island where from 2500 to 1700 B.P precipitation reached or exceeded modern values (Woodruff et al., 2003; Woodruff and Gagen, 2000). Models of ENSO also suggest maximum variability at this time (Clement et al., 2000), while beach ridges at Lake Eyre suggest flood peaks were higher (Dulhunty, 1975). After 1200 B.P. dust flux decreased toward the present, suggesting climate was less variable in comparison to the middle Holocene.

Clement, A.C., Seager, R. and Cane, M.A., 2000. Suppression of El Niño during the mid-Holocene by changes in the Earth's orbit. Paleoceanography, 15: 731-737.

Dulhunty, J.A., 1975. Shoreline shingle terraces and prehistoric fillings of Lake Eyre, arid central Australia. Royal Society of South Australia Transactions, 99: 183-188.

Gillespie, R. et al., 1991. AMS radiocarbon dating in the study of arid environments: Examples from Lake Eyre, South Australia. Palaeogeography Palaeoclimatology Palaeoecology, 84: 333-338.

Magee, J.W., Miller, G.H., Spooner, N.A. and Questiaux, D., 2004. Continuous 150 ky monsoon record from Lake Eyre, Australia: Insolation-forcing implications and unexpected Holocene failure. Geology, 32: 885-888.

Marx, S.K., Kamber, B.S. and McGowan, H.A., 2005a. Estimates of Australian dust flux into New Zealand: Quantifying the eastern Australian dust plume pathway using trace element calibrated ^{210}Pb as a monitor. Earth and Planetary Science Letters, 239: 336-351.

Marx, S.K., Kamber, B.S. and McGowan, H.A., 2005b. Provenance of long travelled dust determined with ultra trace element composition: A pilot study with samples from New Zealand glaciers. Earth Surface Processes and Landforms, 30: 699-716.

Marx, S.K. and McGowan, H.A., 2005. A re-examination of the 1928 trans-Tasman dust transport event. Weather and Climate, 24: 35-55.

McBride, J. and Nickolls, N., 1983. Seasonal relationships between Australian rainfall and the Southern Oscillation Monthly Weather Review, 111: 1998-2004.

McTainsh, G.H., Lynch, A.W. and Tews, E.K., 1998. Climatic controls upon dust storm occurrence in eastern Australia. Journal of Arid Environments, 39(3): 457-466.

Woodruff, C.D., Beech, M. and Gagan, M.K., 2003. Mid-late Holocene El Niño variability in the equatorial Pacific from coral micro atolls. Geophysical Research Letters, 30: 1358.

Woodruff, C.D. and Gagen, M.K., 2000. Coral micro atolls from the central Pacific record late Holocene El Niño. Geophysical Research Letters, 27: 1511-1514.

Toenails: they know where you've been!

Dora C Pearce [1], Kim Dowling [1], Malcolm R Sim [2],
Gordon McOrist [3], Robert Russell [4]
[1]*School of Science and Engineering, University of Ballarat*
[2]*Monash Centre for occupational & Environmental Health, Monash University*
[3]*ANSTO Minerals*
[4]*ANSTO Institute for Environmental Research.*

Abstract

Use of children's toenail clippings as a biomarker of exposure may be problematic when the quantity of material available for analysis is small and surface contamination from outdoor play activity is present. In this study, depth profiling using secondary ion mass spectrometry indicated arsenic was present within the nail matrix and surface contamination was not a major contributor to total arsenic concentration after clippings were cleaned using sonication. The utility and convenience of neutron activation analysis in measuring arsenic in both biological and geological samples has facilitated this research, which found that the transformed clipping and residential soil arsenic concentrations were significantly correlated (Pearson's $r = 0.42$, $p = 0.023$) when residential soil arsenic concentrations for each participant were treated as independent. Systemic absorption of arsenic from soil remains an ongoing problem in the goldfields region of Victoria, with males more likely to play on mine waste than females, thus increasing their exposure risk.

Introduction

Risk assessment is complex due to the need to consider population heterogeneity in susceptibility and lifestyle, source, frequency and duration of exposures (Department of Health and Ageing and Health Council 2002). Biomarkers of exposure are often used to reflect individual variation in uptake by providing an indication of the amount of a toxicant, or its metabolites, present in body fluids or tissues (Bearer 1998). For recent exposures, urine is typically used for arsenic quantification and speciation (Concha *et al.* 1998; Hinwood *et al.* 2004). However, nail arsenic concentration is reflective of a longer term exposure (Chen *et al.* 1999), and toenails represent a longer exposure period than fingernails (Bean 1953). Evidence of exposure to arsenic in soil has been demonstrated in some parts of Australia, although uncertainty remains as to whether the elevated arsenic concentrations observed in toenail clippings were due primarily to systemic absorption of arsenic or external contamination of samples (Hinwood *et al.* 2003).

We sought to investigate arsenic uptake from soil by children living in mining affected areas. Use of children's toenail clippings as biomarker is problematic, however, when the quantity of material available for analysis is small. The utility and convenience of instrumental neutron activation analysis (INAA) in measuring arsenic in small samples, and its sensitivity in quantifying trace elements (Glascock n.d.), has facilitated this research project. An additional advantage is that INAA is also applicable to geological samples, enabling investigation of the association between soil and toenail arsenic levels.

A further complication in the use of children's toenail clippings as biomarker is the potential for surface contamination from outdoor play activity. Depth profiling using secondary ion mass spectrometry (SIMS) was applied to investigate the presence of

surface contamination after clippings were cleaned using sonication in a standard protocol (Karagas *et al.* 2000).

Methods

Study population: Approvals for this research were granted by the Human Research Ethics Committee of the University of Ballarat and the Department of Education and Training Victoria. Two Primary School communities located in gold mining affected areas were involved, commencing in 2006. Plain language statements were distributed to parents/guardians of enrolled students. Residential soil arsenic testing was offered in conjunction with collection of children's toenail clippings for arsenic quantification and completion of a questionnaire. Parental informed written consent for each child participant was required prior to study commencement. Children's plain language statements were also provided at two levels of detail with appropriate language styles deemed suitable for younger (5-7 y) and older students (8-12 y). Children could therefore provide written consent if they wished. On receipt of completed consent forms, labelled collection bags for toenail clippings and questionnaires were distributed.

Toenail clippings as biomarker: Clippings were cleaned using a procedure based on a standard protocol (Karagas *et al.* 2000) to remove surface contamination. Briefly, clippings were sonicated for two 15 min periods in deionised water, rinsed, collected by vacuum filtration, and dried in an incubator at 10ºC.

Soil samples: Composite soil samples, derived from five strategic locations using a 3.8 cm bore auger, were obtained from each residential site where children most frequently played. Soil was mixed, oven dried at 39-43°C for 3 days and where necessary, crushed using a pestle and mortar before approximately 30 gm was sieved to < 2 mm.

Instrumental Neutron Activation Analysis (INAA): INAA was used to quantify arsenic concentration in clipping and soil samples. Clippings were weighed into polythene irradiation containers. Arsenic standards were prepared from 1000ppm As ICP standard solutions (High-Purity Standards) and certified reference materials (CRM's) were included in the analysis. Approximately 0.1 gram of each soil sample was weighed into polythene irradiation containers. Arsenic standards were prepared from similar amounts of CRM's containing known concentrations. Samples and standards were packed into polythene containers which enabled samples to be pneumatically transferred and irradiated with neutrons in the X-176 irradiation facility of HIFAR. Clippings were irradiated for 5 min and soil samples for 1 min. Following decay periods varying from 6 to 30 hours for clippings and 20 to 30 hours for soils, clippings and soils were counted for 60 min and 30 min, respectively, on a 20% Ortec HPGe detector. Arsenic concentrations were calculated using existing FORTRAN computer programs.

Secondary Ion Mass Spectrometry (SIMS): SIMS (ims-5f, Cameca, France) was used for depth profiling of clippings to ascertain if arsenic was present as a surface contaminant or bound within the toenail matrix. A subset of clippings, selected on the basis of quantity available, were sputter-coated with gold to approximately 20nm prior to analysis to alleviate charging. The primary beam used to bombard the surfaces of clippings was composed of Caesium ions (Cs+). The sputtered secondary ions collected were negative ions of C, O and As. Signals were normalised to a matrix

element, C. X-axis (time) relates to depth of analysis, but was not calibrated in this study. Depth profiles were collected predominantly from dorsal surfaces, and some ventral clipping surfaces. An analysis of arsenic signals was conducted to assess relative change with depth and to facilitate comparisons between samples. The first 100-200 s of data was removed due to variability in sputtering rates in the conducting gold layer and throughout stabilization of signals in the nail matrix material.

Questionnaire: Parents of participants completed a questionnaire pertaining to demography, sources of potential exposure to trace elements, activity patterns and diet, parental smoking and occupation.

Statistical analysis: Fisher's Exact test was used for dichotomous data and the Exact Mann-Whitney U test for group comparisons of skewed continuous data. For clipping arsenic concentrations below detection limits, half the detection limit for that sample was assigned. In cases (n = 2) where two sets of clipping samples were provided in larger quantities they were analysed separately. For each of these participants, measured arsenic concentrations above the sample detection limit were available in only one sample, which were subsequently used in the analysis (0.63 ± 0.37 μg/g versus < 0.51 μg/g, and 0.31 ± 0.20 μg/g versus < 0.64 μg/g). The highest recorded soil arsenic concentration was used where duplicate samples were analysed. Agreement between duplicate soil samples was assessed using the Exact Wilcoxon Signed Ranks test for matched pairs. Pearson's correlation coefficient was used to investigate correlations between natural logarithmic transforms of toenail clipping and soil arsenic concentrations, and clipping arsenic concentration and weight. A 2-tailed significance level of 0.05 was used in all analyses. Statistical analyses were performed using SPSS Version 12.0.1 for Windows.

Results

Response rate: In all, 23 households in community one, totalling 30 participants of 124 enrolled students (24%), and 7 households in community two, with 9 participants from 37 enrolled (24%), were involved. Collection of toenail clipping samples coincided with soil sampling, unless returned previously via the school liaison teacher. Toenail clippings were provided by a total of 30 children, 23 (77%) child participants in community one, and 7 (78%) children in community two. One sample from community one was insufficient (1.4 mg) for arsenic determination and was excluded from analyses, giving a total of 29 toenail samples with quantifiable arsenic concentrations, six with detection limits ≤ 0.82 mg/kg. Because participants in communities one and two were comparable on age (median (minimum, maximum) 8 (5, 13) years and 9 (7, 12) years, p = 0.478, respectively), and gender (11 (48%) and 3 (38%) males, p = 0.698, respectively), data were combined. Overall, 12 males and 17 females participated, aged 5 to 13 years (median age 9 years). Soil samples were obtained from all but one household (n = 29), and questionnaire data from 31participants.

Arsenic quantification by INAA of toenail clipping and soil samples: Clipping samples analysed by INAA ranged in weight from 5.4 mg to 150.8 mg (median 27.8 mg) and although small, the natural logarithmic transformed clipping weights and clipping arsenic concentrations were not significantly correlated (Pearson's r = -0.174, p = 0.367). Toenail arsenic concentrations ranged from 0.15 to 2.1 mg/kg (median 0.54 mg/kg), while residential soil arsenic concentrations from households where participants provided clippings for analysis (n = 22), were between 3.3 mg/kg and 130 mg/kg (median 6.9 mg/kg).

Quality control for INAA: NBS orchard leaves with a certified value of 10 ± 2 µg/g arsenic were analysed with each set of toenail clippings, with measured values ranging between 8.1 ± 0.3 µg/g and 11.6 ± 0.3 µg/g. Quality control samples for soil were also measured within the certified range of values: IAEA Soil-5 arsenic concentration 90 ± 13 µg/g [CRM 93.9 ± 7.5 µg/g] and IAEA SL-1 (lake sediment) 29 ± 4µg/g [CRM 27.5 ± 3.0 µg/g]. Replicate soil samples (n=6) were comparable (p = 1.00), indicating adequacy of soil sample preparation.

Risk factors for increased toenail clipping arsenic concentration: The transformed clipping and residential soil arsenic concentrations were significantly correlated (Pearson's r = 0.42, p =0.023) when residential soil arsenic concentrations for each participant were treated as independent. Although not significantly associated in univariate analysis, children who reportedly played occasionally on mine waste (n=4) tended to have higher toenail arsenic concentrations than those who did not (median (Q1, Q3) 0.71 (0.51, 1.31) mg/kg versus 0.50 (0.29, 0.72) mg/kg, p = 0.138). In some cases, these were siblings. Further, all those who reportedly played on mine waste were males aged between 6 and 11 years. No significant difference in clipping arsenic concentration was observed overall between males and females (median (Q1, Q3) 0.64 (0.42, 0.73) and 0.40 (0.26, 0.72), respectively, p = 0.278).

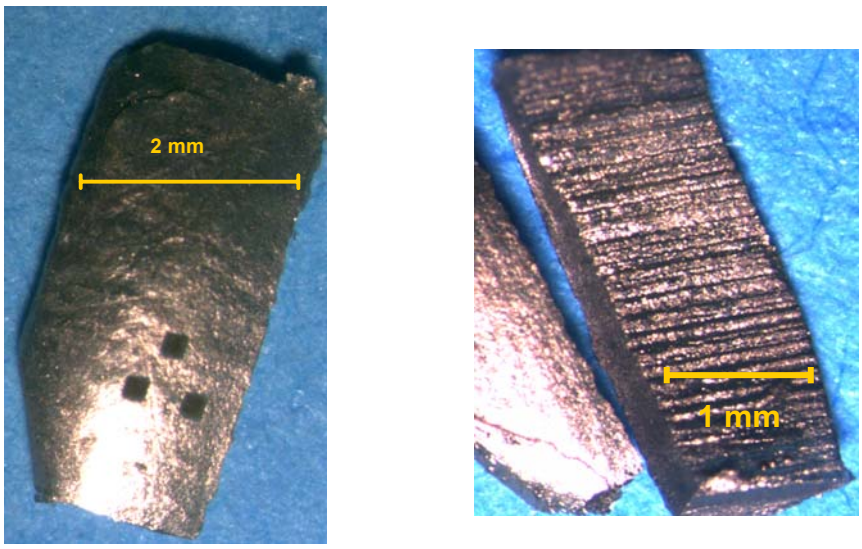

a. b.

Figure 1 Gold coated clipping segments showing a. sites of SIMS investigation through the dorsal layer; and b. ventral layer showing ridges in clipping surface.

Depth profiling by SIMS: Gold coated clipping segments after SIMS analyses show sputter craters on the dorsal surface (Figure 1a), which is smooth in contrast to the ridges evident in the ventral layer of a clipping segment (Figure 1b), making the ventral surface less suited to SIMS investigation. Replicate analyses of the dorsal surface of a clipping taken from a sample with total arsenic concentration of 0.73 mg/kg (Figures 2a and 2b) show variability in intensity of the arsenic signals at different locations. SIMS depth profiling of the dorsal surface of a clipping segment taken from a sample with total arsenic concentration of 0.77 mg/kg shows the arsenic signal deviating substantially from that of the carbon signal, demonstrating that the arsenic is present within the nail matrix, not as a surface contaminant (Figure 2c).

Discussion

Children may be particularly vulnerable to, and at increased risk of, environmental exposures (Bearer 1995; Buffler & Kyle 1999; Graeter & Mortensen 1996). The arsenic content of clippings reflects blood concentrations during nail formation several months prior (Bean 1953; Hopps 1977; Koons & Peters 1994), and the difference in arsenic intensity in the replicate SIMS analyses is consistent with intermittent exposure to arsenic. Importantly, the SIMS results suggest that the arsenic present is bound within the nail matrix, as surface contamination of samples could potentially influence the precision of concentration estimates (Slotnick & Nriagu 2006).

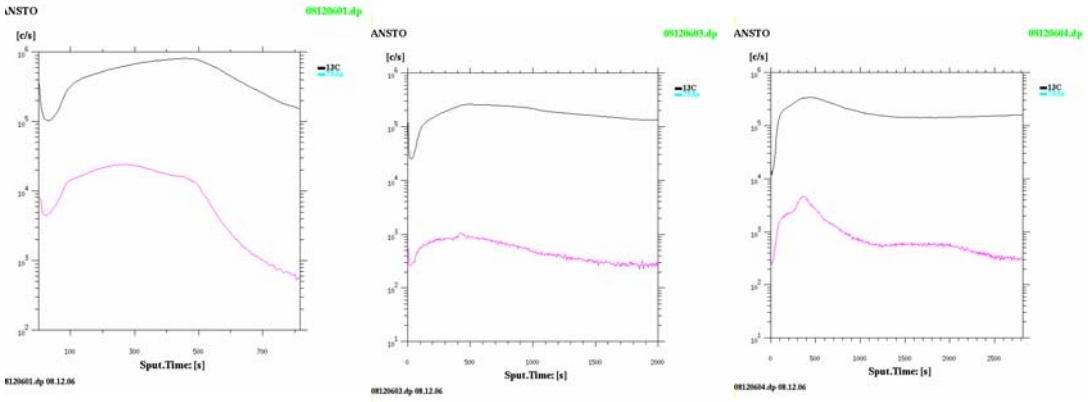

a. b. c.

Figure 2 SIMS curves from replicate analyses of the dorsal surface of a clipping from a sample with arsenic concentration of 0.73 mg/kg where a. shows an initially higher intensity followed by a drop in arsenic concentration within the sample and b. shows a lower intensity of arsenic signal; and c. shows SIMS curves from analysis of the dorsal surface of a clipping from a sample with arsenic concentration of 0.77 mg/kg, in which the arsenic signal deviates substantially from that of the carbon signal, demonstrating clearly that the arsenic is present within the nail matrix and not present as a surface contaminant.

Three (10%) of the 29 residences sampled were found to have soil arsenic concentrations of 100 mg/kg or more, equivalent to, or exceeding, the Australian health-based investigation level of 100 mg/kg for residential soil (enHealth Council 2001). To date, the relationship between arsenic concentration in soil and arsenic concentration in toenail clippings has not been well characterized. Thus it has not been possible to determine appropriate reference levels for arsenic concentrations in toenail clippings (Department of Human Services, Victoria, pers. com. September 24, 2007). However, since toenail clipping arsenic levels tend to increase with soil arsenic concentration, further research is required to ascertain health implications associated with current exposure levels. The application of INAA and SIMS to environmental epidemiological studies has the potential to provide a basis for health risk assessments.

References

Bean W. B. (1953) A note on fingernail growth. The Journal of Investigative Dermatology 20: 27-31.

Bearer C. F. (1995) How are children different from adults? Environmental Health Perspectives 103(Suppl 6): 7-12.

Bearer C. F. (1998) Biomarkers in paediatric environmental health: a cross-cutting issue. Environmental Health Perspectives 106: 813-816. Retrieved March 22, 2005.

Buffler P. A. & Kyle A. D. (1999) Carcinogen risk assessment guidelines and children. Environmental Health Perspectives 107: 286-288. Retrieved May 10, 2004.

Chen K.-L. B., Amarasiriwardena C. J. & Christiani D. C. (1999) Determination of total arsenic concentrations in nails by Inductively Coupled Plasma Mass Spectroscopy. Biological Trace Element Research 67: 109-125.

Concha G., Nermell B. & Vahter M. (1998) Metabolism of inorganic arsenic in children with chronic high arsenic exposure in Northern Argentina. Environmental Health Perspectives 106: 355-359.

Department of Health and Ageing and Health Council 2002 Environmental Health Risk Assessment: Guidelines for assessing human health risk from environmental hazards. Available from http://www.enhealth.nphp.gov.au/council/pubs/pdf/envhazards.pdf , Accessed August 24, 2007.

enHealth Council (2001) Health-based soil investigation levels. Retrieved September 28, 2004, from http://www.health.gov.au/pubhlth/publicat/document/env_soil.pdf.

Glascock MD(n.d.) An Overview of Neutron Activation Analysis Research Reactor Center, University of Missouri, Columbia, Available at http://www.missouri.edu/~glascock/naa_over.htm, Accessed September 22, 2005.

Graeter L. J. & Mortensen M. E. (1996) Kids are different: developmental variability in toxicology. Toxicology 111: 15-20.

Hinwood A. L., Sim M. R., Jolley D. et al. (2003) Hair and toenail arsenic concentrations of residents living in areas with high environmental arsenic concentrations. Environmental Health Perspectives 111: 187-193. Retrieved March 18, 2004.

Hinwood A. L., Sim M. R., Jolley D. et al. (2004) Exposure to inorganic arsenic in soil increases urinary inorganic arsenic concentrations of residents living in old mining areas. Environmental Geochemistry and Health 26: 27-36.

Hopps H. C. (1977) The biological base of using hair and nail for analysis of trace elements. Science of the Total Environment 7: 71-87.

Karagas M. R., Tosteson T. D., Blum J., et al. (2000) Measurement of low levels of arsenic exposure: a comparison of water and toenail concentrations. American Journal of Epidemiology 152: 84-90.

Koons R. D. & Peters C. A. (1994) Axial distribution of arsenic in individual human hairs by Solid Sampling Graphite Furnace AAS. Journal of Analytical Toxicology 18: 36-40.

Slotnick M. J. & Nriagu J. O. (2006) Validity of human nails as a biomarker of arsenic and selenium exposure: A review. Environmental Research 102: 125-139.

Use of ultra-fast diffraction in the design of novel materials

D.P. Riley [1], E.H. Kisi [2], T.C. Hansen [3], P.F. Henry [3]

[1] *Department of Mechanical Engineering, The University of Melbourne, Victoria, 3010, Australia*

[2] *School of Engineering, The University of Newcastle, NSW, 2308, Australia*

[3] *Institut Laue-Langevin, Grenoble, Cedex 9, France*

Abstract

Traditional techniques of developing novel materials often rely on systematic variance of chemical composition and processing parameters to optimise these properties—a time consuming and costly process. The commissioning of the OPAL Research Reactor and The Australian Synchrotron (AS) will change how materials suitable for these applications will be developed. Specifically, time-resolved, *in-situ* diffraction allows for rapid optimisation of materials synthesis by directly monitoring the phase fraction as a function of time/temperature. More importantly, concurrent analysis of thermal, occupancy and phase parameters allow for the role of intermediate phases to be accurately determined, which in higher order compounds often affect the course of the reaction sequence. Details of the high-flux neutron (OPAL) and X-ray (AS) *in-situ* systems will be provided, with an overview of recent developments using these techniques. In brief, ternary compounds of the $M_{n+1}AX_n$ *Phase* classification, have recently been developed using in-situ neutron diffraction to optimise the synthesis process— successfully lowering the synthesis temperature by 37.5% and reducing processing time by 50%.

1. Introduction

The development of novel materials will continue to increase as the demand for higher thermal, mechanical or chemical stability remains. Traditionally these materials have been developed through systematic exploration of composition, processing temperatures or mechanical/chemical post-processing. Although ultimately effective, these experimental methodologies often require considerable resources to optimise the synthesis of novel materials systems. Furthermore, as these techniques are inherently reliant on *ex-situ* analysis of reactants and products, they tend to remain extremely time consuming and often produce incomplete or inaccurate understanding. If materials are to be developed in a timely manner to meet the present and future demands of science and engineering, then new methodologies need to be explored that remove these inherent limitations and allow for concurrent experimental analysis. It is proposed that *in-situ* diffraction has the potential to meet these challenges, through strategic use of stroboscopic or continuous analysis and a considered instrumental design capable of variable fluxes and resolutions. The key to realising *in-situ* diffraction as a processing diagnostic has come from finding a balance between high diffracted intensity and maintenance of good d-spacing resolution. Furthermore, by accessing progressively finer time-resolutions, *in-situ* diffraction provides significant advantages over traditional methods of process diagnostic, most notably through continuous analysis of irreversible reaction kinetics. Using this technique, *in-situ* diffraction analysis provides direct measurement of metastable, intermediate phases, not detectable via alternate techniques. The application of *in-situ* neutron diffraction to the reaction kinetics of MAX Phase materials over a range of time-scales will be discussed through this article.

2. Review of MAX Phases

MAX Phases ($M_{n+1}AX_n$), where *M* is an early transition metal, *A* is a Group III or IV element, and *X* is either C or N, form a strategic class of materials (>100) with a broad combination of metallic and ceramic properties [1]. Of these materials, Ti_3SiC_2 has been the most widely studied example with in excess of 250 research papers published in the last 10 years concerning its structure, synthesis, and properties. Although the remaining materials have been less intensely studied, there is solid evidence to suggest that their properties are very similar to those of Ti_3SiC_2 [2]. With a brittle-to-ductile transition mechanism, Ti_3SiC_2 is readily machinable with conventional tools, reminiscent of a metal. Paradoxically, the material exhibits high temperature strength (Compressive: 500 MPa at 1573K, Bend: 120 MPa at 1573K, Tensile: 60 MPa at 1473K) and chemical stability ($E(O_2) \cong 370$ kJ/mol) similar to ceramics. Along with a high Young's modulus (320 GPa), thermal shock resistance (ΔT>1673K) and hardness (4 GPa), this unique material also demonstrates high thermal (34 W/m.K) and electrical conductivity ($4.5\times10^6\ \Omega^{-1}m^{-1}$). It has been widely reported these properties arise from the ordered layering of the $M_{n+1}AX_n$ crystal structure [3,4]. $M_{n+1}AX_n$ Phases have been produced via a variety of techniques [5-9], but the greatest phase purity and density have historically been achieved through hot isostatic pressing (HIP) at 1600°C for 2 – 4hrs [10,11]. When fabricated using these solid state techniques, synthesis optimisation has been performed using *ex-situ* analysis of reactant and product phases, typically revealing residual binary phases e.g. $Ti_5Si_3(C_x)$ and TiC_x. Unfortunately, both of these binary compounds have significantly different physical properties then those desired from Ti_3SiC_2 and other $M_{n+1}AX_n$ Phases. Additionally, relatively high decomposition temperatures for both $Ti_5Si_3(C_x)$ and TiC_x are responsible for the very high HIP temperatures of Ti_3SiC_2 (i.e. >1500°C) *and* are difficult to completely remove from the product.

3. Ultra-fast In-situ Diffraction: ILL-D20

Upon inspection of the most common reactants used in synthesizing Ti_3SiC_2, it was evident the thermal energy necessary to form this compound could be obtained directly from the exothermic reaction of elemental powders. This technique is commonly know as either self-propagating high-temperature synthesis (SHS) or combustion synthesis and relies upon the rapid elevation of reactants to a reaction ignition temperature, T_{ig}. Once ignited, the SHS exothermic reaction provides the remaining energy required to convert the reactant powders into the desired product. Initial attempts to synthesize Ti_3SiC_2 via SHS by Pampuch *et al*. [6] had successfully produced the compound, but with a high proportion of residual TiC_x and $Ti_5Si_3C_x$ (>10wt.%). The quantitative phase analysis (QPA) of Ti_3SiC_2 during SHS was achieved using the D20 diffractometer of the Institut Laue-Langevin (ILL) [12]. Achieving a time resolution of 0.9s (0.5s acquisition + 0.4s download) the reaction mechanism during this ultra-fast reaction was determined to proceed via five distinct stages; completing full conversion less then 60s after SHS ignition had occurred. In summary, these stages were (i) pre-heating of reactants, (ii) the α-Ti $\rightarrow$ β-Ti phase transformation, (iii) pre-ignition formation of TiC_x and $Ti_5Si_3C_x$, (iv) intermediate formation of a single phase, $TiC_x(Si)$, and (v) the final nucleation and growth of the product phase, Ti_3SiC_2. As previously reported [12] the reaction was shown to have initiated with the thermal transformation of α-Ti $\rightarrow$ β-Ti, a transition clearly identified in the time-resolved diffraction data provided in Figure 2. Using an acquisition time of 0.5s quantitative phase analysis (QPA) was performed. The mass

phase fractions of each reactant, intermediate and product phase are provided in Figure 3, plotted as a function of time (seconds). The most significant feature of this data is the single intermediate phase, $TiC_x(Si)$, that persists for only 6s after SHS ignition begins. It has previously been confirmed [12] that this intermediate phase is isostructural with the crystal structure of titanium carbide (TiC), but contains substantial dissolved Si. With an effective time-resolution of 0.9s (0.4s download), the dominant SHS reaction mechanisms for Ti_3SiC_2 synthesis were determined both qualitatively and quantitatively.

4. The Optimisation of MAX Phase Synthesis using In-situ Diffraction

Retention of intermediate phases within the microstructure of Ti_3SiC_2 is known to be detrimental to the physical properties exhibited by MAX Phase materials. Although *ex-situ* analysis techniques have been used successfully to identify and aid the reduction in retained intermediate phases, variability in phase purity still remained. The significance of using *in-situ* diffraction during the SHS reaction of Ti_3SiC_2 was in proving that the MAX Phase directly precipitates from the intermediate phase, $TiC_x(Si)$. It was also noted that phase purity was linked to various other SHS parameters, most notably the heating rate. It is reported widely [14,15] that the combustion temperature is proportional to the rate of heating, with higher rates producing a more uniform and concentrated combustion. However, lower combustion temperatures generally reduce the phase purity of the MAX Phase products, with fully stoichiometric TiC being the primary intermediate phase retained during these experiments. This is consistent with the observations of Wu *et al*. [8], reporting that the precipitation of Ti_3SiC_2 was progressively inhibited during reactive sintering synthesis due to reduced mobility of Si through TiC_x as $x \rightarrow 1.0$. In that case, the carbon diffusivity alone would control the rate at which interstitial sites within TiC_x and $Ti_5Si_3C_x$ would become fully occupied and hence inhibit MAX Phase homogenisation. Preferential ordering of carbon vacancies and the rate of this carbon ordering, is therefore the rate limiting mechanism of the reaction. The significance of the vacancy ordering was recognised by comparison of the TiC_x(unordered), TiC_x(ordered) and $Ti_3(A)C_2$ structures. Structural units of the TiC_x structure (Fm-3m), namely the Ti_6C octahedra, are common to the lamella of both the ordered TiC_x and Ti_3AlC_2 structures. Furthermore, differences between each of these structures centre on the stacking sequence and orientation of the Ti_6C layers, with an additional intercalation of an A-group layer for the MAX Phase material. A sequential pathway may be visualised by considering the following structural transformations,

1. TiC_x (unordered) $\rightarrow$ TiC_x (ordered) induced through thermally excited vacancy ordering of the interstitial carbon.
2. TiC_x (ordered) $\rightarrow$ TiC_x (ordered + relaxed) shearing of alternate Ti_3C_2 layers
3. TiC_x (ordered + relaxed) $\rightarrow$ $Ti_3(A)C_2$ through intercalation of A-group layer

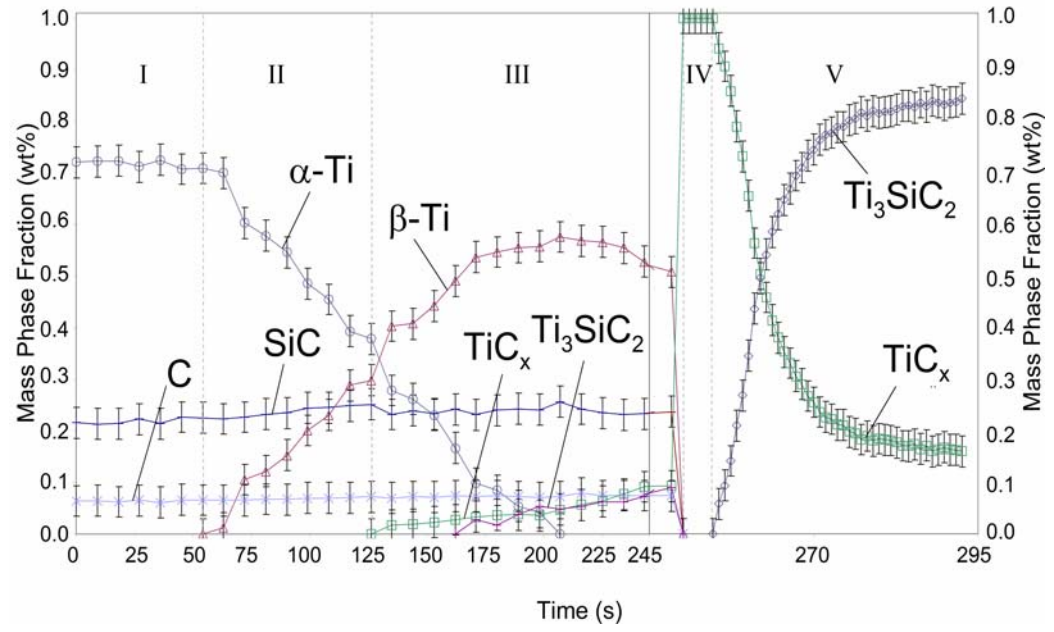

Figure 3 – Quantitative Phase Analysis (QPA) as a function of time of the SHS reaction sequence from 3Ti+SiC+C reactants, forming Ti_3SiC_2 via direct precipitation from the single intermediate phase.

It was proposed that the synthesis of MAX Phases could be achieved through intercalation of the A-group element into the vacant interstitial sites of a sub-stoichiometric compound. The only constraint would be matching the C/Ti ratio to that existing within the final MAX Phase, which for Ti_3SiC_2 was C/Ti = 0.67. This powder would then be mixed with the required A-group element (e.g. Al or Si) in a 3:1 ratio. Thermal process optimisation was experimentally obtained using *in-situ* neutron diffraction conducted at a time resolution of 1 minute. Figure 6 details the four stages of the reaction sequence by which aluminium was successfully intercalated into the precursor material, $TiC_{0.67}$, synthesizing titanium aluminium carbide, Ti_3AlC_2 [16]. The intercalation of aluminium reacting with the precursor $TiC_{0.67}$ can be described by the four stages of the reaction sequence, best detailed by plotting the diffraction angle against processing time. Figure 6 illustrates this reaction with intensity of the diffracted intensity shown as an increasing brightness. *Stage I*: Heating of the reactant powders at 10°C/min produces thermal shifts in the diffraction peaks, best observed by comparing the aluminium reflections (positions at 22.5°, 38.5°, 54.0° and 64.0°) with the more thermally stable precursor peaks (positions at 28.0° and 60.0°). *Stage II*: Begins with the melting of aluminium at 660°C, with a corresponding increase in the diffuse background intensity. As the diffuse intensity decreases with time this suggests disordered substitution of the molten aluminium into the precursor material. *Stage III*: Was delineated from Stage II when the diffuse background arising from the melting of aluminium had returned to levels equal to those of the initial reactants. The formation of superlattice reflections was clearly visible. Upon inspection, these reflections were shown to correspond to a doubling of the cubic precursor unit cell due to of an ordering of the interstitial vacancies. A steady increase of the diffracted intensity for each superlattice reflection is consistent with further ordering of the interstitial vacancies. *Stage IV*: Here the disappearance of the precursor superlattice reflections was accomplished by the precipitation of the

product MAX Phase (Ti_3AlC_2). Simultaneous decreases of the superlattice reflections and increases of the Ti_3AlC_2 intensity are consistent with nucleation and growth from the precursor material. Optimisation of a novel MAX Phase synthesis route was only possible through the use of *in-situ* diffraction analysis, revealing for the first time the integral role of the single intermediate phase. The use of solid state precursors to optimise the reaction sequence of Ti_3AlC_2 and Ti_3SiC_2 has been successful in reducing the processing temperature and time by 37.5% and 50%, respectively.

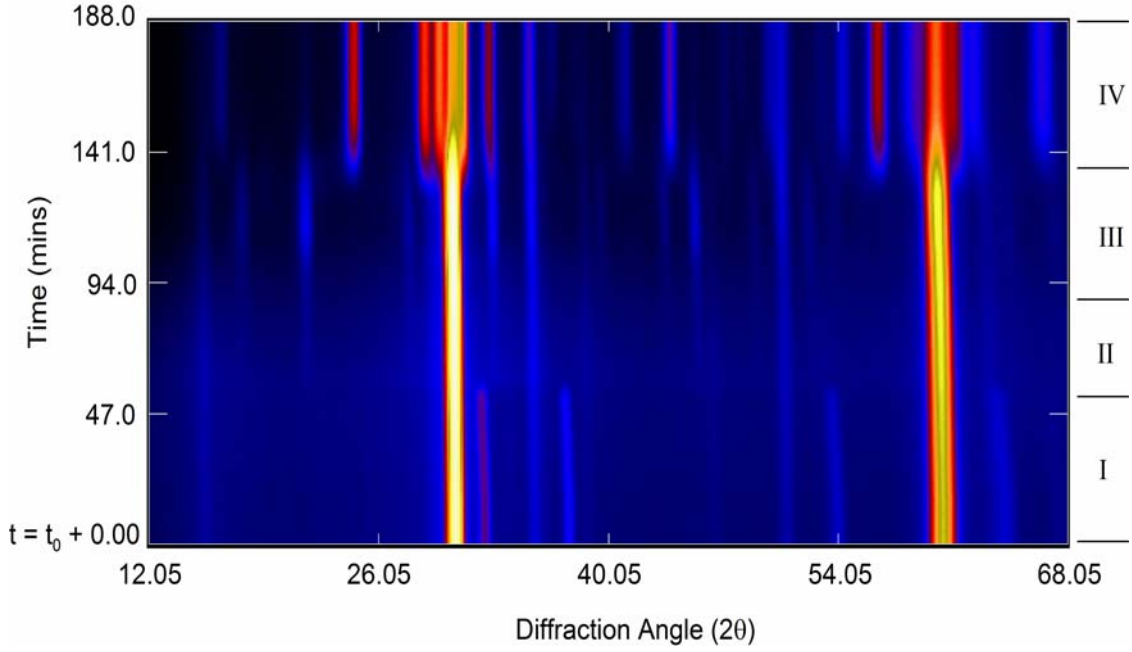

Figure 6 – Synthesis of titanium aluminium carbide using a customised solid state precursor and aluminium powder. In-situ diffraction obtained at a time resolution of 1 minute using the D20 diffractometer at the Institut Laue-Langevin (ILL), Grenoble, France [16].

7. Acknowledgements

The authors wish to thank both Pierre Convert and Jacques Torregossa (D20-ILL). This work was funded by the Australian Research Council (ARC, DP0451429), Access to Major Research Facilities Program (AMRFP), Grant 04/05-N-28 and ILL Experiment No. 5-25-112. The Author wishes to also acknowledge the award of an AINSE Research Fellowship.

8. References

1 E.Wu, E.H. Kisi, S.J. Kennedy and A.J. Studer, "In-situ neutron powder diffraction study of Ti_3SiC_2 synthesis", J. Am. Ceram. Soc., Vol. 84, 11 2281-88 (2001)

2 T. El-Raghy, M.W. Barsoum, A. Zavaliangos, S.R. Kalidindi "Processing and Mechanical Properties of Ti_3SiC_2: II, Effect of Grain Size and Deformation Temperature.", J. Am. Ceram. Soc., Vol. 82, pp.2855-2860, (1999)

3 Wu, E, Kisi, E.H. and Riley, D.P., "Intermediate phases in Ti_3SiC_2 synthesis from Ti/SiC/C mixtures studied by time-resolved neutron diffraction", J. Am. Ceram. Soc., Vol. 85, No. 12, pp.3084-3086, (2002)

4 E.H. Kisi, J.A.A. Crossley, S. Myhra, M.W. Barsoum, "Structure and crystal

chemistry of Ti_3SiC_2", J. Phys. Chem. Solids, Vol. 59, 1437-1443 (1998)

5 Goto, T. and Hirai, T., "Chemically vapour deposited Ti3SiC2", Mat. Res. Bull., Vol. 22, pp. 1195-1201, (1987)

6 Pampuch, R., Lis, J., Piekarczyk, J., Stobierski, L., "Ti_3SiC_2 –Based Materials Produced by Self-Propagating High-Temperature Synthesis (SHS) and Ceramic Processing", J. Mat. Synth. & Process.,Vol.1,pp.93-100, (1993)

7 Barsoum, M.W. and El-Raghy, T., "Synthesis and Characterisation of a Remarkable Ceramic: Ti_3SiC_2", J. Am. Ceram. Soc., Vol. 79, No. 7, pp.1953-1956, (1996)

8 Goesmann, F., Wenzel, R. and Schmid-Fetzer, R., "Preparation of Ti_3SiC_2 by electron-beam-ignited solid-state reaction", J. Am. Ceram. Soc., Vol. 81, No. 11, pp.3025-3028, (1998)

9 Feng, A., Orling, T. and Munir, Z.A., "Field activated pressure-assisted combustion synthesis of polycrystalline Ti_3SiC_2", J. Mater. Res., Vol. 14, No. 3, pp. 925-939, (1999)

10 El-Raghy, T. and Barsoum, M.W., "Processing and mechanical properties of Ti_3SiC_2: I, Reaction path and microstructure evolution", J. Am. Ceram. Soc., Vol. 82, No. 10, pp. 2849-2854, (1999)

11 T. El-Raghy, M.W. Barsoum, A. Zavaliangos, S.R. Kalidindi "Processing and Mechanical Properties of Ti_3SiC_2: II, Effect of Grain Size and Deformation Temperature", J. Am. Ceram. Soc., Vol. 82, pp.2855-2860, (1999)

12 D.P. Riley, E.H. Kisi, T.C. Hansen, A.W. Hewat, "Self-Propagating High-Temperature Synthesis of Ti_3SiC_2: I. Ultra-High Speed Neutron Diffraction Study of the Reaction Mechanism" J. Am. Cer. Soc., Vol. 85, pp.2417-2424, (2002)

13 "Diffraction Thermometry and Differential Thermal Analysis", E.H. Kisi, D.P. Riley, J. Appl. Crystallogr., Vol. 35, pp. 664-668, 2002

14 Moore, J.J. and Feng, H.J., "Combustion Synthesis of Advanced Materials: Part I. Reaction Parameters", Prog. Mat. Sci., 39, pp.243-273, (1995)

15 Moore, J.J. and Feng, H.J., "Combustion Synthesis of Advanced Materials: Part II. Classification, Applications and Modelling", Prog. Mat. Sci., Vol. 39, pp.275-316, (1995)

16 D.P. Riley and E.H. Kisi, "The Design of Crystalline Precursors for the Synthesis of $M_{n+1}AX_n$ Phases and their Application to Ti_3SiC_2", J. Am. Ceram. Soc., 90, [7], pp2231-2235 (2007)

Determination of deuterium adsorption site on palladium(100) using low energy ion scattering spectroscopy

I. Kambali [1], D. J. O'Connor [1], M. J. Gladys [1], M. A. Karolewski [2]
[1] *Department of Physics, The University of Newcastle, Callaghan-Australia*
[2] *Department of Chemistry, University of Brunei Darussalam, Brunei Darussalam, Borneo*

Interaction of hydrogen (H) or deuterium (D) with metal surfaces such as Palladium (Pd) is of great interest to study since there is a wide range of its applications, including nuclear fusion technology, catalysis, and hydrogen storage.

There has been considerable agreement in the research to study H and D absorption phenomena on Pd. At low temperatures (below room temperature) hydrogen atoms are absorbed in the Pd bulk. Once the temperature of Pd is increased to a room temperature, the H atoms are adsorbed in the Pd hollow sites [1, 2] and then desorbed from the surface as temperature increases [1-4]. Nevertheless the height of H at which it is adsorbed on Pd surface as well as the existence of the adsorbate in the subsurface remains debatable.

One of the techniques available to study the adsorption phenomena of such adsorbates on the metal surface is ion beam analysis which consists of low energy ion bombardment. In this project, a beam of 1.9 keV Ne^+ ions was incident on Pd(100) surface to study the adsorption site of deuterium atoms on the surface at room and higher temperatures as well as the possibility of D atoms occupying the subsurface sites by detecting the recoiled D^+ ions. This version of low energy Elastic Recoil Detection Analysis (ERDA) is extremely surface sensitive with the capacity for atomic layer depth resolution. To gain the most precise information about height of adsorption sites, a comparison has been made to the predictions of the computer simulation Kalypso 2.1.

The dependence of the recoil yield on the azimuthal direction of the projectile incidence has a distinctive general shape for different adsorption sites on Pd(100) that can be used to identify the type of adsorption site involved without any need for detailed analysis. For hollow site adsorption, shadowing occurs along the <100> directions, but is absent for the <110> directions. For bridge site adsorption, shadowing occurs along the <110> directions, but is absent for the <100> directions. For on-top site adsorption, shadowing should not occur at all if the adsorbed atom sits sufficiently high enough above the surface. The vertical location of the D adsorption site relative to the Pd surface layer may be determined through comparisons of the experimental azimuthal dependence of the recoil yields with simulations for different assumed D atom positions.

Figure 1(a) compares the azimuthal dependence of D^+ recoil yields (in the energy range 100-350 eV, detected at recoil angle $\theta = 60^o$ to the surface) for projectile incidence angle (α) of 15^o at 295K with the simulated results for different D vertical positions (z, measured relative to the surface Pd layer). The recoil yields display maxima around the <110> directions (0^o azimuth), and are negligible in the <100> directions (45^o azimuth). This behaviour conforms with that expected for D adsorption in Pd(100) hollow sites. The absence of D^+ recoil yields in the <100> directions rules out any adsorption model that involves significant population of the bridge and on-top sites.

The goodness of fit between the simulated and experimental data can be assessed through the mean square error which is shown for different assumed values of z in fig.

1(b). For polar incidence angles of 15° and 20° (not shown in the fig.), the best agreement between the experimental and simulated data is obtained when a value z = 0.25 ± 0.05Å is assumed in the simulation model.

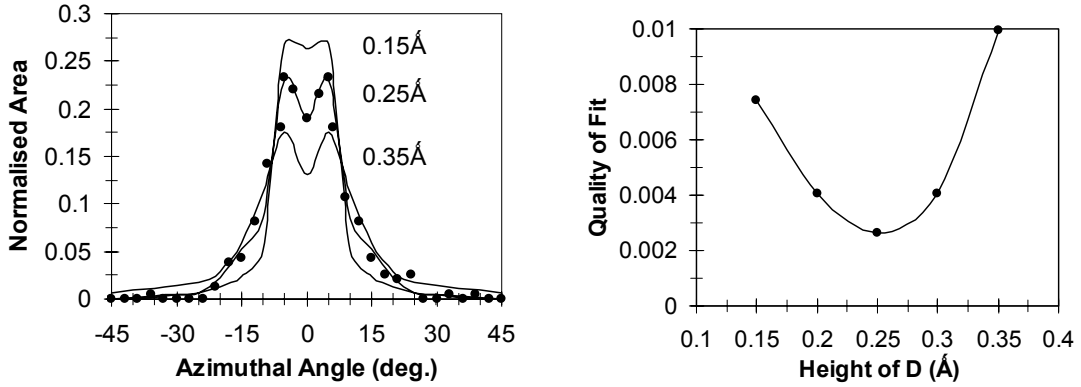

(a) (b)

Fig. 1(a) Comparison of measured (dot points) and simulated (solid lines) azimuthal scans for deuterium recoiled from Pd(100) surface for 15o incidence angle. The quality of fit is provided in (b) which reveals the best agreement for the deuterium to sit 0.25Å above the surface.

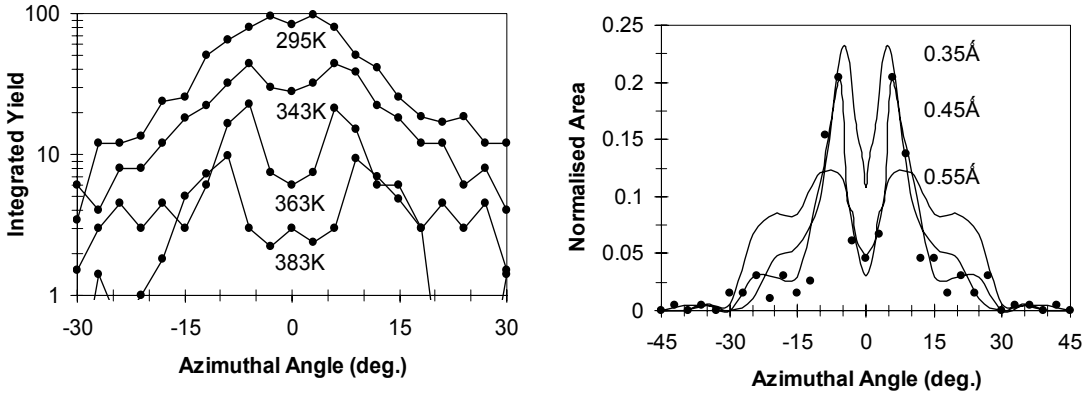

(a) (b)

Fig. 2(a) Azimuthal dependence of D recoil yield as a function of target temperature for incidence angle of 15°. The coverage decreases with increasing temperature and the enhanced yield features move to large angles from the <110> direction (0° azimuth). (b) Comparison of the yield for 363K with computer simulations of different adsorption heights. Best fit is 0.45Å at 363K and 0.40Å at 343K (not shown).

As the temperature increases the desorption rate of the deuterium increases which leads to a lower equilibrium surface coverage (fig. 2a). As well, there is a marked increase in the angular separation of the enhanced yield features close to the <110> direction (0° azimuth). The cause of this increased separation is not immediately obvious. The most possible explanation is that the D adsorption site moves to a higher position above the surface. This is in keeping with the two adsorption sites observed by Besenbacher [7] and is reasonable considering that with increasing temperature the coverage would decrease. The results obtained have been compared to the simulations of the yields from the p(1x1), c(2x2) and p(2x2) structures and the best fit corresponds to the p(2x2) which has not been observed in the earlier studies. This is

consistent with the measured coverage at such high temperatures assuming monolayer equilibrium coverage at room temperature. This comparison with computer simulations reveals that the best fit corresponds to an adsorption height of 0.40Å at 343K and 0.45 Å at 363K (fig. 2b).

To determine whether deuterium atoms reside in subsurface sites, a survey was conducted with the computer simulation to identify the most sensitive geometry for location of subsurface recoils. This was found to be for 30^{o} incidence which reveals significantly different azimuthal 'signatures' for surface only (fig. 5, solid line) and surface plus subsurface adsorption sites (fig. 5, dashed line). A notable difference is the existence of enhanced yield features at $\pm$30^{o} azimuths if deuterium atoms sit on the subsurface sites. In the subsurface simulation, the D atoms were placed at 0.25 Å above the first layer of Pd(100) surface as well as 0.39 Å above the second layer [5] but directly under a surface layer Pd atom (the octahedral site). A comparison of the measured yield under these conditions provides a good match with the computer simulation for only surface sites occupied.

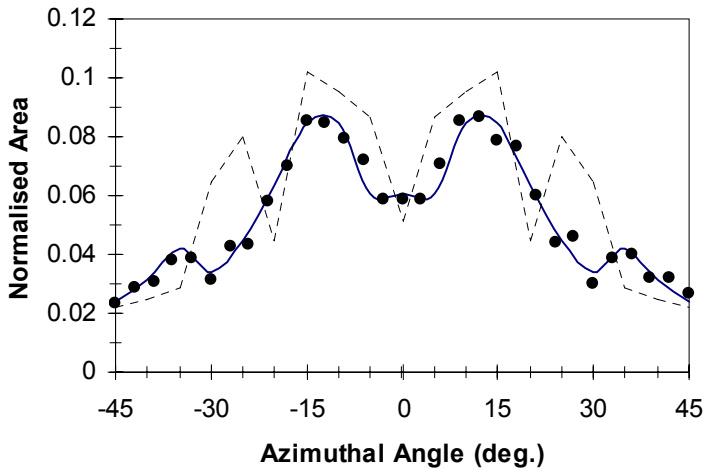

Fig. 3 Surface (solid line) and surface plus subsurface (dashed line) D structures simulated by Kalypso 2.1 software compared to experimental results (dot points) for D^{+} recoil yield when Ne is incident at 30^{o} to the surface. Best agreement is obtained for the simulation with no D atoms occupying Pd(100) subsurface sites.

References

[1] H. Conrad, G. Ertl, and E. Latta Surface Science 41 (1973) 435.

[2] M. G. Cattania, V. Penka, R. J. Behm, K. Christmann, and G. Ertl Surface Science 126 (1982) 382.

[3] N. Tsuboi, H. Okuyama, and T. Aruga, Surface Science 566-568 (2004) 777.

[4] H. Okuyama, T. Nakagawa, W. Siga, N. Takagi, M. Nashijima, and T. Aruga, Physical Chemistry 103 (1999) 7876.

[5] W. Dong, V. Ledentu, Ph. Sautet, A. Eichler, and J. Hafner Surface Science 441 (1998) 123.

[6] A. Eichler, J. Hafner, and G. Kresse, Journal of Physics: Condensed Matter 8 (1996) 7659.

[7] F. Besenbacher, I. Stensgard, and K. Mortensen, Surface Science 191 (1987) 288.

Fabrication of sub micron layers in single-crystal diamond

B.A. Fairchild [1], P. Olivero [1], A. Cimmino [1], M. Draganski [2], B. C. Gibson [3], A. D. Greentree [4], D. Hoxley [1], S. T. Huntington [3], S. Rubanov [1], A. Stacey [1], J. Salzman [5], B. Meyler [5], Y. Bayn [5], A. Lahav [5], D. N. Jamieson [4], S. Prawer [4]

[1] School of Physics, Micro Analytical Research Center, The University of Melbourne

[2] RMIT, Dept. of Applied Physics, RMIT University Melbourne

[3] Quantum Communication Victoria, School of Physics, The University of Melbourne

[4] Centre for Quantum Computing Technology, School of Physics, The University of Melbourne

[5] Dept. of Electrical Engineering and Microelectronics Research, Technion, Israel

This method demonstrates for the first time the fabrication of a sub-micron thickness single crystal diamond layers. We show significant progress in realising all-diamond optical structures, by constructing 330 nm single crystal diamond membranes. The process paves the way for the fabrication of sub-micron components and especially photonic band gap cavities, waveguides, and cantilevers when combined with focused ion beam (FIB) milling. The technique uses a combination of high energy helium implants into single crystal diamond to produce layers of damage within the sample. Annealing at high temperature sharpens the diamond/non-diamond interface. The non diamond material is then removed by galvanic etching. FIB milling and micro manipulation is then used to carve devices for further characterization.

Comparison of the atomic structure in InP amorphised by electronic or nuclear ion-energy-loss processes

C.S. Schnohr [1], P. Kluth [1], A.P. Byrne [2,3], G.J. Foran [4], M.C. Ridgway [1]

1Department of Electronic Materials Engineering, Research School of Physical Sciences and Engineering, Australian National University, ACT 0200, Australia

2 Department of Physics, College of Science, Australian National University, ACT 0200, Australia

3Department of Nuclear Physics, Research School of Physical Sciences and Engineering, Australian National University, ACT 0200, Australia

4Australian Nuclear Science and Technology Organisation, Menai, Australia

Abstract

InP was amorphised by ion irradiation in two very different regimes: (i) 185 MeV Au irradiation where the energy loss was predominantly via inelastic processes (electronic stopping) or (ii) Se irradiation in an energy range 0.08 – 7 MeV where elastic processes (nuclear stopping) were dominant. We used extended X-ray absorption fine structure spectroscopy to determine the structural parameters of the amorphous phase. Despite very different energy deposition mechanisms no significant difference in the atomic-scale structure was observed. Based on these results, the amorphisation process in both energy regimes will be discussed and compared.

Introduction

Amorphisation of semiconductors is an important aspect of their modification by means of ion irradiation. It has been studied extensively for InP in the keV ion energy range1 and was first reported for Swift Heavy Ions (SHIs) by Herre et al.2. The energy loss processes for these two regimes are fundamentally different. Incoming ions of the keV to low MeV range deposit their energy predominantly via ballistic collisions with the target atoms (nuclear stopping), resulting in atomic displacements if sufficient energy is transferred. In contrast, incoming SHIs primarily interact with the target electrons (electronic stopping), leading to excitation and ionization of the electronic system. Given the differences in the energy deposition processes, one may well expect differences in the resulting amorphous phase structures. Extended X-ray absorption fine structure spectroscopy (EXAFS) has been successfully applied to determine the atomic-scale structural parameters of semiconductors amorphised in the low energy regime3. We now present the results of a detailed comparison of the amorphous structure of InP amorphised by either nuclear or electronic energy loss4.

Experimental Details

For the EXAFS measurements, InP/In0.53Ga0.47As/InP heterostructures [2.75 μm/50 nm/ (100) substrate] were first grown by metal organic chemical vapour deposition. For amorphisation induced by electronic interactions (SHI sample), the material was irradiated at room temperature with 185 MeV Au ions to a fluence of 3x1013 cm-2. At this ion energy, the damage due to the electronic energy loss extends 5-10 μm into the sample5 thus spanning the entire depth of the InP epilayer. The InP substrate and the In0.53Ga0.47As layer were then removed by selective chemical etching. For amorphisation due to nuclear energy deposition (Low Energy Ion (LEI) sample), the same process of chemical etching was performed prior to irradiation. The InP films, bonded to Si for support, were then amorphised at liquid nitrogen temperature with multiple-energy/multiple-fluence Se irradiations in the energy range of 80 keV to 7 MeV with the fluences chosen to produce a constant value of total

vacancy production over the extent of the InP epilayer (total fluence 8.5x1015 cm-2). The amorphous nature of the material after irradiation under these conditions was confirmed by Rutherford backscattering spectrometry in a channelling configuration. A crystalline InP reference sample was also prepared from the heterostructures as above. All samples were finely crushed and mixed with BN prior to the EXAFS measurements.

The In K-edge EXAFS was measured in transmission mode at a temperature of ~ 20 K using beamline NW10A at the Photon Factory, Japan. After the measurement, the SHI and LEI samples were annealed at 150°C for one hour then re-measured. Such low temperature annealing leads to structural relaxation with the aim of achieving the intrinsic amorphous phase governed by the minimum-energy configuration3,6. The data was processed and then analysed after performing a Fourier transformation (FT) from photoelectron wave number (k) space into radial space. Details of the procedure are given in Ref. 4.

Results and Discussion

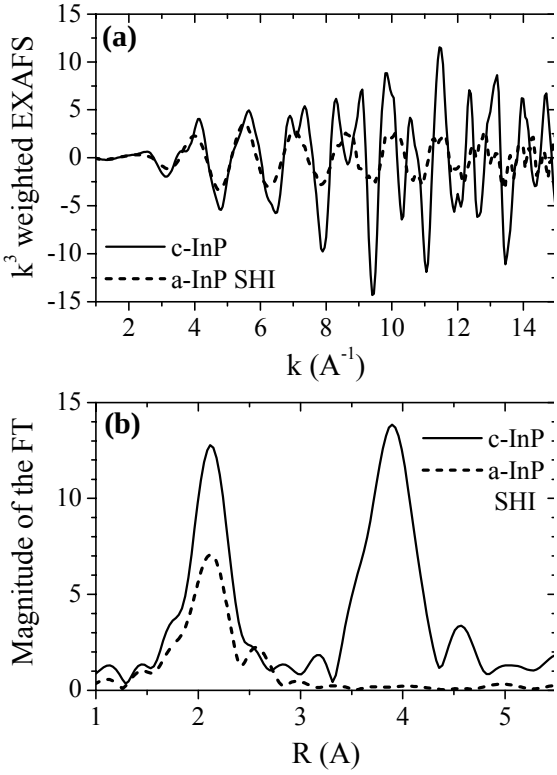

Figure 1: (a) k3-weighted EXAFS spectra of crystalline InP (c-InP, solid line) and amorphous InP as-irradiated by 185 MeV Au (a-InP SHI, dashed line) versus the photoelectron wave number k. (b) Fourier transforms of the spectra shown in panel (a) as a function of the non-phase-corrected radial distance R from the absorber.

Figure 1 (a) shows the k^3-weighted EXAFS signal as a function of k for the crystalline standard and the as-irradiated SHI sample. The EXAFS spectrum of the crystalline material shows a complex structure indicating the presence of several different frequencies. This is confirmed in the corresponding FT, Fig. 1 (b), which contains three distinct peaks at $R \sim 2.1$ Å, $R \sim 3.9$ Å, $R \sim 4.6$ Å representing scattering from the first (P), second (In) and third (P) nearest neighbours (NN), respectively. In contrast, the EXAFS of the irradiated sample is dominated by a single frequency and only the first shell peak is observed in the FT. Structural disorder in amorphous materials is typically sufficient to prevent coherent scattering from beyond the first shell. The absence of higher shell peaks in the EXAFS spectrum is a characteristic feature of amorphous semiconductors and has been previously observed after ion irradiation in the LEI regime[3]. Our EXAFS measurements are consistent with this behaviour and confirm the formation of the amorphous phase after SHI irradiation. In addition to the reduction in amplitude of the first NN P peak, a small second peak at $R \sim 2.6$ Å is apparent in Fig. 1 (b) resulting from the presence of a second component - In atoms - in the first shell of the amorphous material.

Figure 2 (a) plots the FT versus R for the SHI and LEI samples measured in as-irradiated and relaxed forms. Clearly, the spectra for the two samples amorphised in the different energy regimes are very similar both before and after relaxation.

The relaxed samples are characterized by an increase in amplitude of the P peak while the overall features of the amorphous phase are retained. All four spectra exhibit the smaller peak at $R \sim 2.6$ Å associated with In-In bonds. The contribution of these homopolar bonds is further shown in Fig. 2 (b) plotting the FT of the as-irradiated SHI sample and the best fit including the individual scattering contributions of P and In atoms in the first shell. The structural parameters obtained from the fitting and a detailed discussion are given in Ref. 4.

The effects of amorphisation and relaxation on the structural parameters are similar to those observed previously for InP amorphised in the low energy regime[6,7]. No significant difference is observed when comparing the In-P contribution of the SHI sample with that of the LEI sample. Comparing the In-In contributions, a small difference is apparent in the amplitude of the peak, however, the magnitude of the experimental uncertainty inhibits us from an unambiguous assignment of its physical origin. We therefore conclude that amorphisation in both energy regimes leads to a similar amorphous phase structure despite the fundamentally different energy transfer mechanisms.

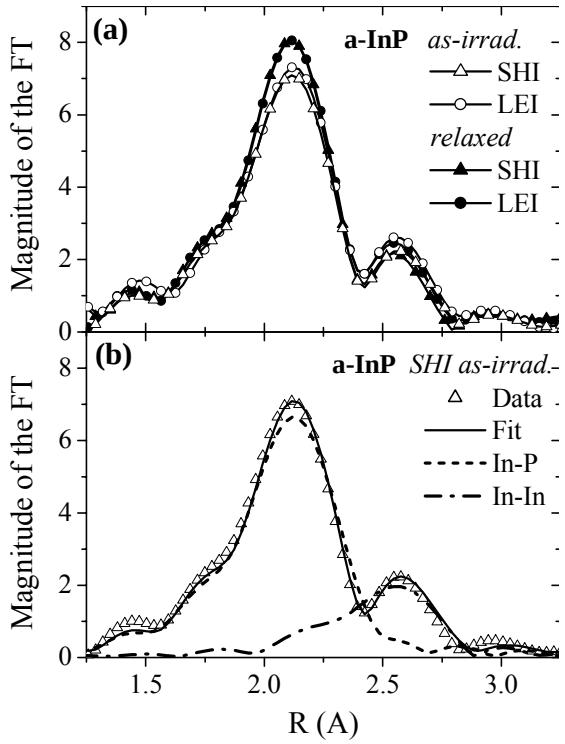

Figure 2: (a) Fourier transforms of the experimental EXAFS of amorphous InP versus R. Shown are the spectra of InP amorphised by 185 MeV Au (a-InP SHI, triangles) and by multiple-energy Se irradiation in the range of 0.08 to 7 MeV (a-InP LEI, circles) for the as-irradiated and relaxed samples (open and full symbols, respectively). For clarity, only every second data point is represented by a symbol. (b) Experimental data from panel (a) and the best fit as a function of R for the as-irradiated SHI sample. Every data point is now represented by a symbol. Also shown are the two contributions arising from In-P and In-In bonds in the first shell (dotted and dash-dotted line, respectively).

Processes induced by ion irradiation are non-equilibrium in nature and different models have been proposed to account for experimental findings. On one hand, an extended Thermal Spike model has recently been applied to predict the irradiation conditions necessary to produce continuous amorphous tracks in InP and good agreement with experimental data was obtained[5]. The Thermal Spike model assumes that electronic energy deposition above a certain threshold leads to melting of the

material along the ion trajectory which, in the present case, is subsequently quenched into the amorphous phase during rapid resolidification. Our SHI irradiation conditions fall within the energy range where the calculated maximum temperature exceeds the melting point and a "melt and quench" process is expected[5]. On the other hand, damage production in the LEI regime is usually associated with collision cascades and the formation, accumulation and growth of various types of defects. Studies of InP irradiated under conditions very similar to our LEI irradiation demonstrate a direct amorphisation process is operative, where amorphous material is produced within a single ion impact[1,8]. Nordlund *et al.* have investigated the amorphisation mechanism during LEI irradiation using molecular dynamics (MD) simulations. For both Ge[9] and GaAs[10] they report recoils of several keV lead to molten regions in the material which subsequently form amorphous pockets upon cooling. In contrast, collision cascades in Si are less dense and hence less damage with a higher fraction of isolated defects results[9]. Following their discussion and supported by the direct amorphisation observed experimentally, we expect a process similar to that in Ge and GaAs to take place in InP for our LEI irradiation conditions. Thus, independent of the energy transfer mechanism, amorphisation in both regimes proceeds via a similar process. As a consequence, our SHI and LEI samples have a nearly identical atomic structure. Amorphisation of InP by quenching from the liquid has been modelled with MD simulations by Lewis *et al.*[11]. Homopolar bonds are present in the liquid phase and are retained (8% of all bonds) after quenching into the amorphous phase. The authors conclude that the presence of chemical disorder is necessary to stabilize the amorphous phase. Our SHI and LEI samples, in both the as-irradiated and the relaxed states, contain a significant fraction of In-In bonds. Given the additional agreement of our experimental results with theoretical predictions of the amorphous phase structure resulting from a quench from the melt, our results could be viewed as indirect evidence that the amorphisation process common to both energy regimes is indeed quenching of molten regions. These molten regions were formed due to the energy loss of the incoming ions, either via electronic stopping for the SHI case or nuclear stopping for the LEI case.

Conclusions

In conclusion, structural parameters of InP amorphised by ion irradiation where the energy loss was dominated by either electronic (SHI) or nuclear (LEI) stopping were determined from EXAFS measurements. No significant difference in the atomic structure of the two samples amorphised in the different energy regimes was apparent despite the fundamentally different energy transfer mechanisms. In agreement with the Thermal Spike model (SHI) and MD simulations for collision cascades (LEI), the common amorphous phase structure reported herein suggests the energy deposition leads in both cases to a molten region that is subsequently quenched into the amorphous phase.

References

1 E. Wendler, T. Opfermann, P.I. Gaiduk, J. Appl. Phys. 82, 5965 (1997).

2 O. Herre, W. Wesch, E. Wendler, P. I. Gaiduk, F. F. Komarov, S. Klaumünzer, P. Meier, Phys. Rev. B 58, 4832 (1998).

3 M. C. Ridgway, C. J. Glover, G. de M. Azevedo, S. M. Kluth, K. M. Yu, G. J. Foran, Nucl. Instr. Meth. B 238, 294 (2005).

4 C. S. Schnohr, P. Kluth, A.P. Byrne, G.J. Foran, M.C. Ridgway, submitted

[5] A. Kamarou, W. Wesch, E. Wendler, A. Undisz, M. Rettenmayr, Phys. Rev. B 73, 184107 (2006).

[6] G. de M. Azevedo, C. J. Glover, M. C. Ridgway, K. M. Yu, G. J. Foran, Phys. Rev. B 68, 115204 (2003).

[7] C. J. Glover, M. C. Ridgway, K. M. Yu, G. J. Foran, T. W. Lee, Y. Moon, E. Yoon, Appl. Phys. Lett. 74, 1713 (1999).

[8] E. Bezakova, A. P. Byrne, C. J. Glover, M. C. Ridgway, R. Vianden, Appl. Phys. Lett. 75, 1923 (1999).

[9] K. Nordlund, M. Ghaly, R. S. Averback, M. Caturla, T. Diaz de la Rubia, J. Tarus, Phys. Rev. B 57, 7556 (1998).

[10] K. Nordlund, J. Peltola, J. Nord, J. Keikonen, R. S. Averback, J. Appl. Phys. 90, 1710 (2001).

[11] L. J. Lewis, A. de Vita, R. Car, Phys. Rev. B 57, 1594 (1998).

Detecting oligonucleotide immobilization and hybridisation using TOF-SIMS

M. Dieker [1], P.J. Pigram [1], N. Brack [1], G.A. van Riessen [1], H.J. Griesser [2], S. Greisser [2], P.C. Nguyen [3], P.S. Hale [4]

1 Centre for Materials and Surface Science and Department of Physics, La Trobe University, Melbourne, Australia

2 Ian Wark Research Institute, University of South Australia, Mawson Lakes, Australia

3 Department of Bioengineering, University of Washington, Seattle, USA.

4 Department of Mining, Metallurgy and Materials Engineering, Laval University, Quebec, Canada

DNA microarray technology is a powerful analytical tool based on sequencing by hybridisation. In recent years, oligonucleotides chip technology has been a topic of growing interest in the areas of gene discovery, clinical diagnostics and toxicological research.

The immobilisation and subsequent hybridisation of surface bound oligonucleotides was investigated using a Time of Flight Secondary Ion Mass Spectrometer (TOF-SIMS) equipped with a bismuth (Bi^+) cluster ion source. The oligonucleotides were immobilised onto planar and patterned propanal plasma modified silicon and fluorinated ethylene propylene (FEP) surfaces. The immobilisation of surface bound oligonucleotides was identified by the detection of sugar/phosphate and nucleobase fragments. TOF-SIMS imaging of patterned propanal coatings demonstrated that oligonucleotide immobilisation was uniform and restricted to areas of aldehyde functionality.

A common method of detecting hybridisation at a solid surface uses target DNA labelled with fluorescent or radioactive markers. In this study, an alternative approach using TOF-SIMS coupled with the multivariate analysis technique of Principal Components Analysis (PCA) was investigated. This technique offers direct detection of hybridisation in the absence of any labelling procedures. Hybridisation of immobilised oligonucleotides was detected via the identification of high mass fragments. Initial findings from PCA also show good discrimination between immobilised and hybridised oligonucleotide sequences.

Blending lead-210 and AMS age profiles from estuarine sediment cores to reconstruct Holocene climate change in the Sydney Region

Robert Haworth [1], Ros James [1], Geraldine Jacobsen[2]
[1]*University of New England;* [2]*ANSTO*

Introduction

A composite age profile was obtained by blending records from Lead-210 and AMS Carbon-14 determinations from a sediment core (Figure 1) extracted from a quiet backwater of Port Hacking estuary, southern Sydney. This comprehensive dating made it possible to reconstruct the record of the past 2500 years of environmental change in this part of the Sydney Basin from geochemical, magnetic susceptibility, and palynological evidence from the sediments.

The Port Hacking core (CTB1) was only one of twelve taken across the Sydney Basin in all the major estuaries and as far afield as the Blue Mountains. The methods worked out on core CTB1 were applied to these other cores.

The first step in gaining a blended age profile was to determine the Lead-210 profile for the core. Although the unstable isotope Lead-210 has a half life of only ~ 22 years and thus as an age marker can only reach back less than 200 years, this would nonetheless mark the point in the core below which samples to obtain reliable AMS dates could be usefully selected.

The Lead-210 Profile

The log linear plot of the activity of unsupported Lead-210 measured for each sample of core CTB1 demonstrates a steady decrease in Lead-210 activity with depth down to 301 mm (Figure 2a), inferring that the sediments have not been seriously bioturbated. Below 301 mm, activities are low, indicating they are at background level, and the sediment no more than 200 years old. The Radium-226, with which unsupported Lead-210 should reach equilibrium when it completes its decay, varies only slightly throughout the profile, and the Pb:Ra ratio shows regular decline, suggesting relatively steady sedimentation from the same or similar sources. The depth of 330 mm is the notional limit of European influence at

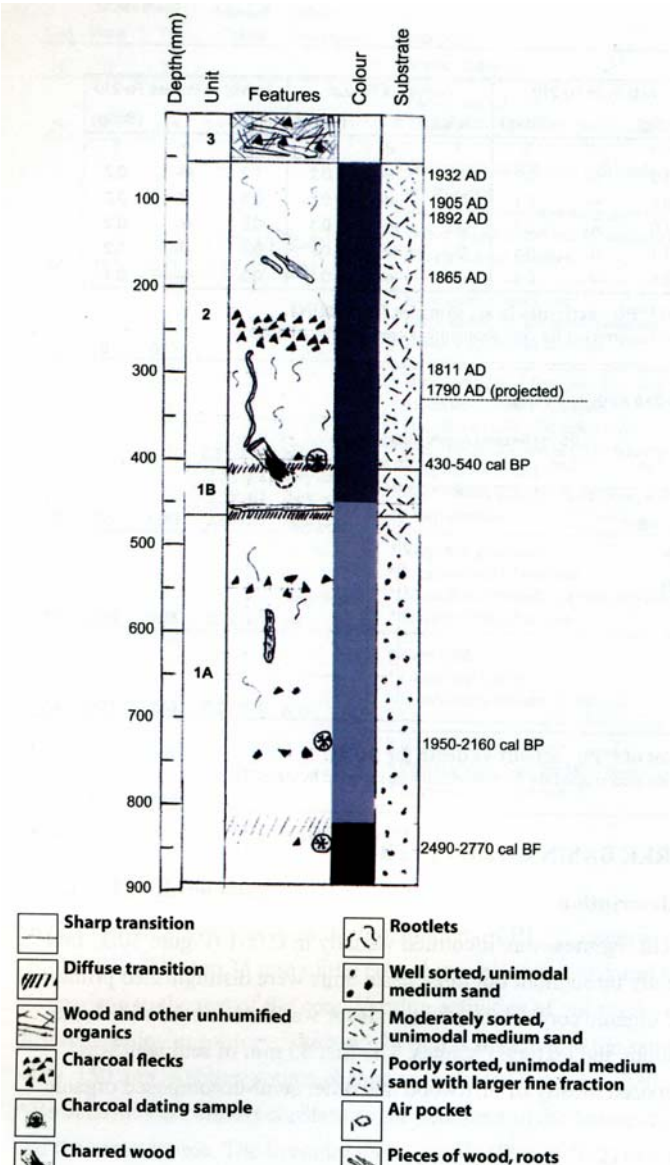

Figure 1: Core CTB 1 – Lead-210 and AMS age profile (cored from Cabbage Tree Basin, a shallow estuarine arm of Port Hacking, southern Sydney region).

1790 AD (Figure 1) and was estimated using the extrapolated sedimentation rate of samples in the zone above.

(a)

Depth (mm)	CIC model
55 - 82	1932
82 - 110	1905
110 - 137	1892
164 - 192	1865
274 - 301	1811
1790 projection	~330 mm

(b)

Depth (mm) From	To	Radiocarbon Age	Calendar Age	Sample Reference	Lab Details	Material Submitted
383	411	450 ± 40 BP	Modern? (430 - 540 cal BP)	OZG257	ANSTO	charcoal piece
739	767	2130 ± 50 BP	1950 - 2160 cal BP	OZG258	ANSTO	sediment & charcoal
849	876	2590 ± 40 BP	2490 - 2770 cal BP	OZF549	ANSTO	charcoal piece
Midden under tree throw near surface		560 ± 50 BP	Modern (59 - 290 cal BP)	WK9142	Waikato	oyster shell

(c)

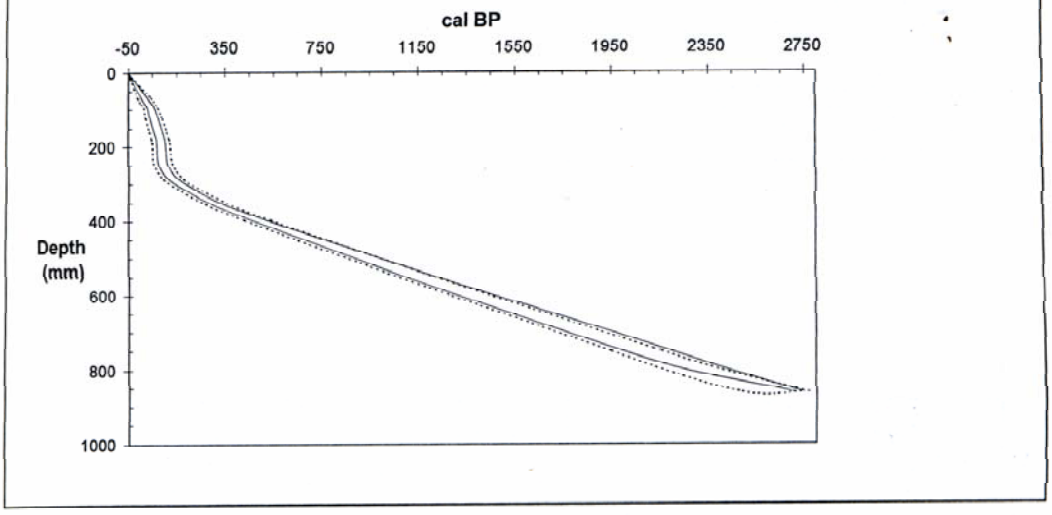

Figure 2: (a) Age estimates calculated from sedimentation rates derived from six Lead-210 samples from CTB1 used as input to composite age/depth. (b) Results and calibration of AMS analyses of three samples from CTB1 and another from a shell on the surface of a nearby rock shelter used as input to composite age/depth. (c) Composite age/depth curve for CTB1 generated from linear interpolation between Lead-210 and AMS age estimates. (Dashed line indicates 2 σ age estimates and solid line indicates 1 σ age estimates. Lead-210 ages were adjusted by -51 years to calibrate them in relation to AD 1950.)

The AMS Profile

The chronology of the lower part of the core was established with three AMS dates converted to calendar dates (Figure 2b). The first samples were taken from as far down the core as possible, in order to work upwards towards the Lead-210 activity limit. Prior to AMS radiocarbon measurement, both the plant matter and charcoal samples were treated using the standard AAA method to remove contaminating carbonates and humic material (2M HCl for 2 hours at 60°C, 0.25% - 0.1% NaOH at 60°C, repeated until the solution is clear and final 2M HCl for 4 hrs.) After drying, the sample was combusted and the resulting carbon dioxide was reduced to graphite using hydrogen over an iron catalyst at 600°C.

The last 300-1000 years were the main target area and time, as this has proved most difficult to date by Carbon-14 because of certain anomalies. The fixing of the base of Lead-210 activity in the sediment to a reasonable degree of precision is able to overcome some of the uncertainties in Carbon-14 ages for the last 400 years by

shortening the error bars where they intrude into the ~ 200 year span of Lead-210 activity. Knowledge of climate and environment in the immediate pre-European period is most important for the present, and we hope this work will extend information about this.

Blended Profile

The age estimates calculated from the Lead-210 profile in CTB1 and those derived from radiocarbon techniques show reasonable continuity (Figure 2C). The projected Lead-210 placement of AD 1790 at 330 mm fits with the AMS profile (Figure 1). The ages display sufficient consistency to establish the history of sedimentation and from phytoliths and pollen extracted from the sediment, a vegetation history. It must be stressed that there are possible disparities which may arise from comparing sediment input averaged over a 2500 year period based on three AMS ages with the much better dated Lead-210 profile (6 ages for 200 years). However, the blended profile offers a good preliminary chronology to guide further work, and it demonstrates that the two techniques can be usefully combined.

Research conclusions and findings

The record from all 12 cores which were analysed by methods developed on the core CTB1 template shows alternating cooler and warmer, wetter and dryer periods, and a charcoal record which suggests that fire regimes were predominantly climate-driven, though with some evidence of increased human agency in the last 1000 years, and especially in the last 200 years. However, charcoal peaks in the record may represent a record of erosion disturbance as much as increased wild fire in the catchment.

Both the saline and fresh water wetlands of the Sydney Basin provide a rich depository of environmental information, with one outstanding core from the Blue Mountains reaching back to the terminal Pleistocene suggesting a surprising dominance of cool rain forest taxa over Eucalyptus, until the late Holocene when increased charcoal associated with Eucalyptus/Myrtaceae pollen replacing Podocarpus suggested that fire, from natural or human causes, had altered conditions.

Low energy lead implantation into Si for novel group IV nanomaterials

Andreas Markwitz*
GNS Science, National Isotope Centre, PO Box 31-312, Lower Hutt, New Zealand

Fax: +64-4-570-4657, Email : a.markwitz@gns.cri.nz

Novel group IV nanomaterials can be produced by low-energy ion implantation in Si followed by electron beam annealing. GNS has established a new dual ion beam implantation facility that produces high current ion beams from any gas and sputter material. Typical examples of ions that are extracted from the gas phase are $^{1}H^{+}$, $^{4}He^{+}$, $^{12}C^{+}$, $^{14}N^{+}$, $^{14}N_2^{+}$, CO^{+}, CO_2^{+}, $^{16}O^{+}$, $^{20}Ne^{+}$ and $^{40}Ar^{+}$. The isotopes $^{13}C^{+}$, $^{15}N^{+}$ and $^{18}O^{+}$ are produced using enriched gases. Sputter materials are used to generate $^{27}Al^{+}$, $^{28}Si^{+}$, $^{48}Ti^{+}$, $^{56}Fe^{+}$, Cu^{+}, Co^{+}, Sn^{+} and Pb^{+} ions, for example. A heater gas source is used for producing S^{+} and Sb^{+} ion beams. These ions can be implanted into any solid material for doping, materials modification and irradiation purposes. The high current ion beam is electrostatically scanned across the sample to produce a laterally homogeneous implantation. The ion range can be adjusted by the terminal voltage between 5-30 keV. A post acceleration stage allows for an additional acceleration of up to 20 keV. The implantation chamber is kept at 5 x 10^{-8} mbar during implantation. At GNS, much research has focused over the last few years on producing SiC nanocrystals on Si, named nanoboulders, by implanting 10-20 keV C^{+} ions into wafer Si. These SiC nanocrystals grow in vacuum during annealing with a high current raster scanned electron beam [1-2]. Annealing simply Si wafer material with this computer controlled electron beam annealer produces Si nanostructures, named nanowhiskers that offer fascinating applications in field emission devices [3-4]. Annealing Si targets that have been partly implanted with C^{+} ions results in the simultaneous production of Si nanowhiskers in the un-implanted region and SiC nanoboulders in the implanted region [5].

To investigate the formation of Pb nanostructures in Si, for example for tailor-make corrosion resistant electrical contacts, series of Pb^{+} ions were implanted shallowly with 5-20 keV ion energy with varying fluence. As an example, the following brief discussion focuses on the implantation of 7 keV Pb into (100) Si. Table 1 lists the dependence of the ion range, sputtering yield, Pb peak concentration and Pb surface concentration on the ion fluence. The ion energy and fluence range was chosen to implant a significant amount of lead into the sample with the Pb profile intersecting with the surface. Similar carbon implantations have proven to produce large SiC nanostructures on Si after electron beam annealing. It was found to be important that the carbon concentration stays well below 50 at.% and that the carbon depth profile intersects with the surface.

Ion fluence (10^{15} at cm^{-2})	1.0	2.0	3.0	5.0	7.0	9.0	12.0
Ion range (nm)	11.0	10.8	10.7	10.4	10.1	9.8	9.3
Sputtering yield	1.99	1.96	1.96	1.97	2.00	2.05	2.11
Peak concentration (at.%)	3.44	6.08	8.55	12.85	16.62	19.79	25.15
Surface conc. (at.%)	0.00	0.04	0.13	0.30	1.74	3.65	5.80
Area under peak (a.u.)	20.12	40.23	60.38	100.47	139.24	178.72	230.21

Table 1: Dynamic Trim calculation of 7 keV Pb implantation into (100) Si.

The calculated Pb depth profiles are shown in Figure 1a to illustrate the increase in surface and peak concentration with increasing ion fluence.

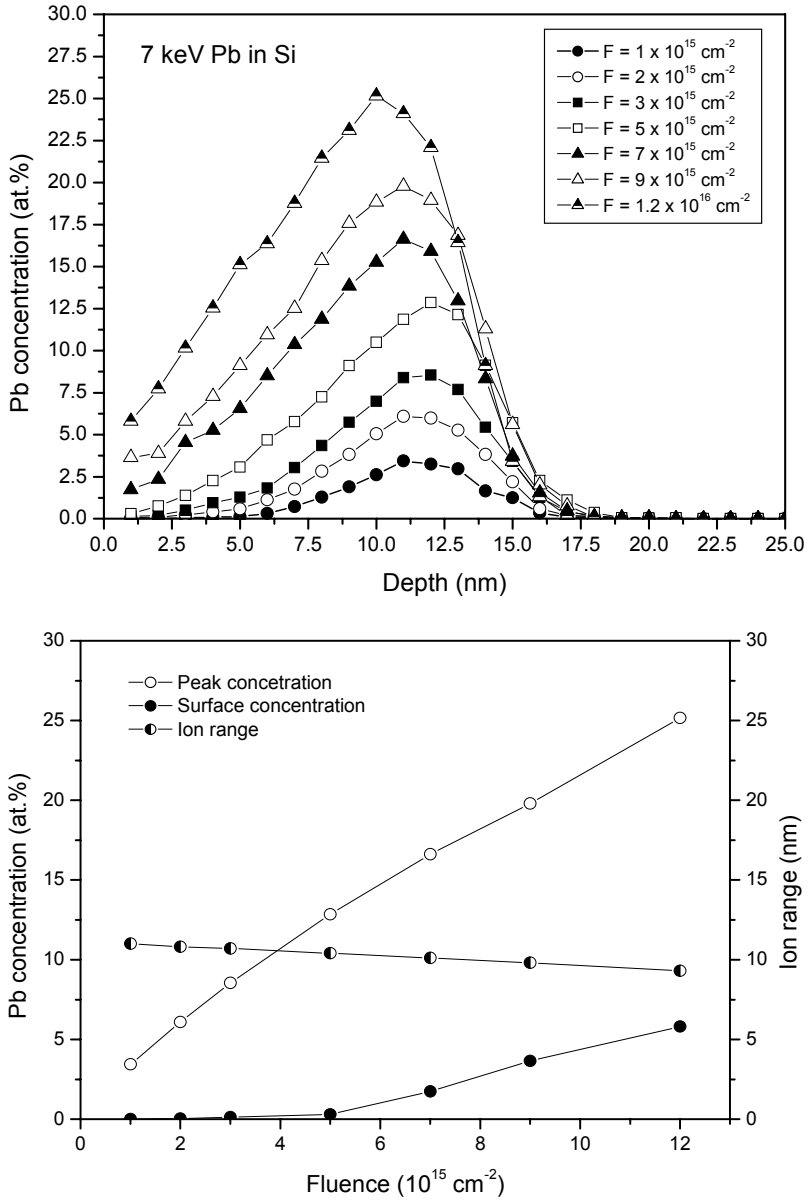

Figure 1: (a) Calculated Pb depth profiles (ion energy 7 keV), (b) dependence of peak and surface concentration and ion range on ion fluence.

Figure 1b shows the dependence of the peak and surface concentration and ion range on the ion fluence. As expected, the Dynamic trim calculations show an increase in peak concentration and surface concentration with increasing fluence. The peak concentration increases linearly with increasing fluence, which is explained by a static sputtering yield value around 2.0 (table 1). Even though the Pb profile starts to intersect with the surface at a fluence of 3 x 10^{15} cm^{-2}, the sputtering yield does not change significantly. The linear decrease in ion range from 11 to below 10 nm with increasing fluence from 1 x 10^{15} to 1.2 x 10^{16} cm^{-2} results in an increased Pb concentration at the surface. At around 5 x 10^{15} cm^{-2}, the lead concentration starts to rise linearly with increasing fluence.

RBS measurements were performed with a 2.0 MeV $^4He^+$ ion beam to determine the Pb dose. Figure 2 shows three representative Pb measurements for Si samples implanted with 7 keV.

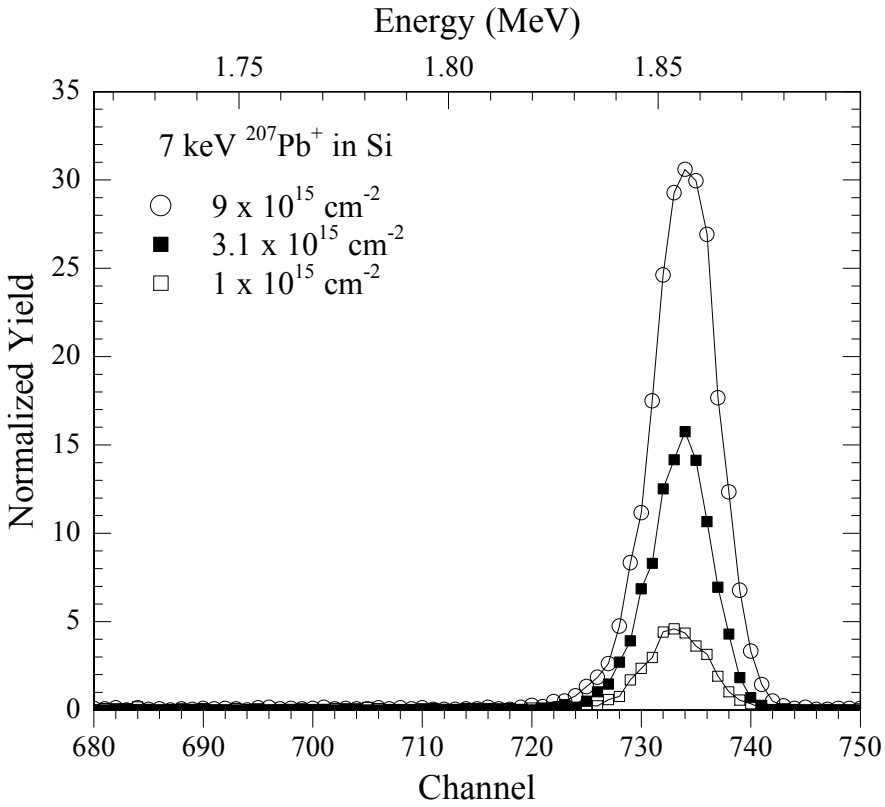

Figure 2: Lead profiles measured with RBS.

Table 2 shows the results of the evaluation of the Pb profiles with RUMP. Data from PIXE measurements that were performed simultaneously with RBS are also listed in table 2.

	A	B	C	D	E	F
7 keV Pb+ ion implantation	Dynamic trim area under peak	RBS dose (10^{15} cm^{-2})	PIXE dose (cts.)	Fluence (10^{15}) / dynamic trim area	Fluence (10^{15}) / RBS dose	PIXE dose / RBS dose (10^{15})
F = 1 x 1015	20.12	0.9	4 ± 28	0.045	1.11	LOD
F = 3 x 1015	60.38	2.9	385 ± 40	0.047	1.06	132
F = 9 x 1015	178.72	6.8	740 ± 43	0.050	1.32	109

Table 2: Comparison of Dynamic TRIM, RBS and PIXE dose. LOD = limit of detection

Table 2 shows that the Dynamic Trim calculation (columns A and D) predicts a linear relationship between the dose and the ion fluence in the fluence range from 1 – 9 x 1015 cm-2. This is in agreement with the RBS data (columns B and E) measured for the samples implanted with 1 and 3 x 1015 cm-2. However, the sample implanted

with 9 x 1015 cm-2 reveals a significant loss in the fluence to dose ratio (column E). This is confirmed by the PIXE measurements for the samples implanted with 3 and 9 x 1015 cm-2, which also show a decrease in the ratio of the measured dose and fluence (columns C and F).

The dynamic Trim, RBS and PIXE results show that it is possible to (1) implant Pb into the surface of silicon with 10 – 20 at.% and (2) produce a Pb depth profile that intersects with the surface. Further studies will focus on annealing effects of the implanted samples with an electron beam under high vacuum conditions to diffuse the Pb atoms towards the surface in a controlled manner.

The author wished to acknowledge the scientific and technical contributions from Horst Baumann, John Kennedy, Chris Purcell, John Futter, Bill Trompetter and Perry Davy.

References

[1] A. Markwitz, V. J. Kennedy, S. Johnson, W. J. Trompetter, M. Rudolphi and H. Baumann, "SiC nanoboulders on silicon – a nuclear reaction analysis study of low energy ^{13}C implanted and subsequently electron beam annealed (100) silicon", Nucl. Instr. and Meth B217 (2004) 583 - 588

[2] A. Markwitz, S. Johnson, M. Rudolphi, H. Baumann and A. Mücklich, "Formation of SiC nanoboulders on (100) silicon after carbon implantation and electron beam rapid thermal annealing", Applied Physics Letters 86 (2005) 013108

[3] S. Johnson, A. Markwitz, M. Rudolphi and H. Baumann, "Nanostructuring of silicon (100) using electron beam rapid thermal annealing", Journal of Apply. Phys. 96 (2004) 605

[4] S. Johnson, A. Markwitz, M. Rudolphi, H. Baumann, S. P. Oei, K. B. K. Teo and W. I. Milne, "Field emission properties of self-assembled silicon nanostructures on n- and p-type silicon", Applied Physics Letters 85 (2004) 3277

[5] A. Markwitz, S. Johnson and M. Rudolphi, "Simultaneous formation of SiC and Si nanostructures on silicon by local ion implantation and electron beam annealing", Appl. Phys. Lett. 89, 153122 (2006)

Bridging the gap between the nano-particle and single crystal surface science

M. J. Gladys [1,4], L. O. Mentes, L. Abelle, A. Locatelli and G. Held[1,3]
[1]*Department of Chemistry, University of Cambridge, Lensfield Rd, Cambridge, CB21EW, UK*
[2]*Sincrotrone Trieste, S.c.p.A., Padriciano 99, I-34012 Trieste, Italy*
[3]*Department of Chemistry, University of Reading, Whiteknights, Reading RG6 6AD, UK*
[4]*School of Mathematical and Physical Sciences, University of Newcastle, Callaghan 2308, NSW Australia.*

Over the past 50 years fundamental surface chemistry has almost continually been performed on single crystal surfaces to essentially minimise the possible parameters within the system. Nanoparticles on the other hand are increasingly being used in industry due to better performance and less mass, but are difficult to investigate. We have used a novel idea to bridge this expanse, and investigate surface reactions on particular facets within a polycrystalline surface using Low energy and X-ray Photo Emission Electron Microscopy (LEEM and X-PEEM). In this way we can determine for the first time the crystal orientation and measure reaction kinetics simultaneously on each facet on the surface. We find that boundaries between the facets play a significant role in the reaction kinetics of CO oxidation, which signifies the importance of fundamental experiments on polycrystalline materials.

Introduction

Automotive heterogeneous catalysis has evolved in leaps and bounds over the past few decades, with extremely sophisticated sensor controlling the most minute increases in unwanted carbon and NOx gases. This comes at a time when environmental concerns are in strong debate and petroleum prices at record levels. It is predicted that in the not too distance future, car catalysts will work so effectively, that they will, in fact, lower pollution levels in our atmosphere.

Most recently the Toyota corporation has announced that Iridium is there new choice of catalytic material for use under lean burn conditions, and for this reason we have chosen to investigate reactions on polycrystalline iridium. Along with Nitrous oxides (NOx), Carbon monoxide (CO) is one of the gases prevalent within the final phase of the combustion engine, which needs to be eliminated before entering the atmosphere. Iridium is well known for its CO oxidation capabilities it has been attracting attention for a variety of industrial applications. However iridium metal is much scarcer than other precious metals such as platinum, which makes it less desirable for a large range of applications.

Low Energy Electron Microscopy (LEEM) and Photo Emission Energy Microscopy (PEEM) using synchrotron radiation are techniques that allow us to characterise polycrystalline surfaces and measure reactions in action. LEEM is a relatively new technique with its first operation in 1985 by Teileps and Bauer and has progressed into a very powerful surface science instrument. [Bau94] With the incorporation of synchrotron light, the LEEM/X-PEEM system is one of the world's most sophisticated surface science techniques that allow a multitude of different experiments. These include electron micro-diffraction and microscopy, X-ray spectroscopy as well as fine structure and spin polarised techniques.

Polycrystalline surfaces consist of a menagerie of close packed, low miller index crystal faces of all shapes and sizes, but typically consist of three surfaces, labelled {100}, {111} and {110}. It is well known that grain boundaries provide pathways for

bulk diffusion, however the boundaries between faces on the surface may also influence or even dominate reactions and therefore not relate to idealised single crystal investigations. Okumura et al. [Oku06] used DFT calculations to conclude that Iridium nanoclusters behave similar to bulk terminated Ir surfaces. This suggests that work on polycrystalline surfaces will provide invaluable information on reactions occurring on nanoparticles catalysts. For our experiments we utilise the "micro" abilities of the instrument; that is, measuring over a very small area of the sample, typically a micron in diameter with resolutions down to 5nm. This allows us to differentiate sections of the surface and measure a variety of experiments simultaneously on different surfaces.

Experimental and Preliminary Results

The experiments were done on the Nanospectroscopy beamline at the ELETTRA synchrotron, Trieste, Italy. LEEM images of a surface show the elastically backscattered electrons reflected from the surface are used to image the sample in real space. LEEM images of areas on the iridium surface are shown in figure 1, illustrating the different crystallite facets. Using the Micro-LEED facility the crystal structure of each facet was determined and shown in the inserts in figure 1. Across the entire surface, the crystallite facets were found to be of all shapes and sizes, ranging from 1um to a few hundred micron and were stable throughout the reaction experiments. C1s XPS spectra were measured in the X-PEEM dispersive mode which allow fast spectra to be taken over several micron area.

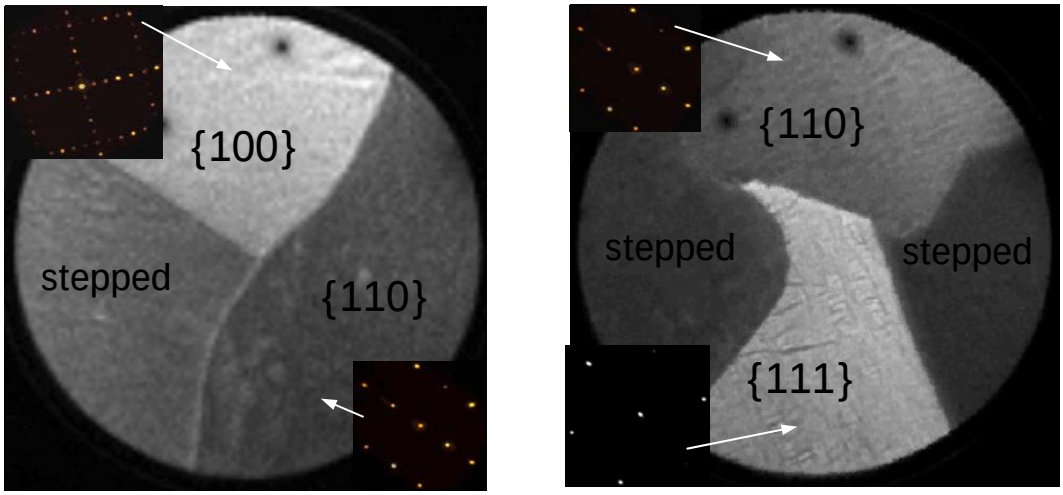

Figure 1: LEEM images of polycrystalline iridium surface showing {100}, {111} and {110} facets, along with stepped facets of varying orientation. LEED images from the facets of clean polycrystalline iridium as included and show the typical square, rectangle and hexagonal structures for the (100), (110) and (111) surfaces respectively.

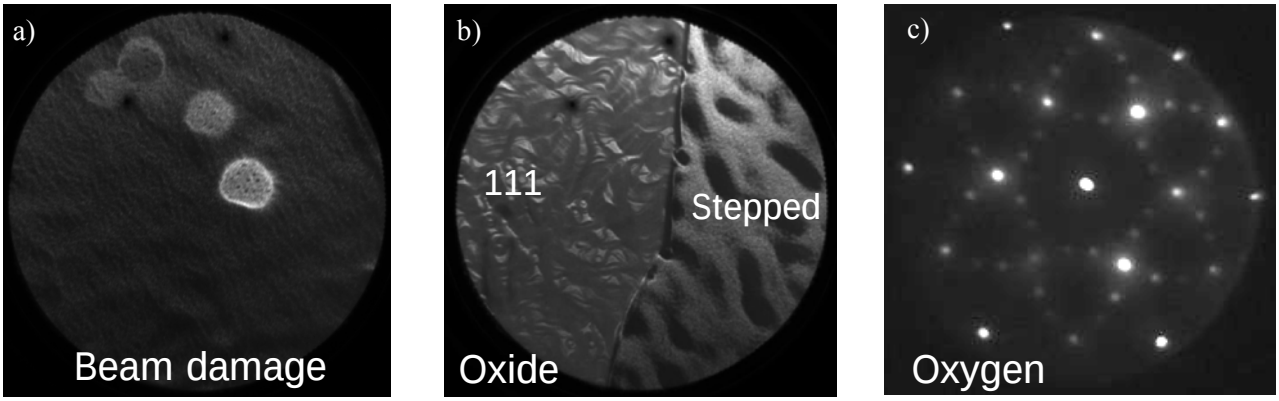

Figure 2: a) Beam damage of adsorbed CO molecules caused by 100eV electrons. b) Oxide structures on stepped facet and oxygen adsorbed onto Ir(111) facet. c) Strange oxygen structures on Ir(111) facet.

Figure 2 displays two LEEM images that were generated on the polycrystalline surface. Figure 2a) was illustrates the destructive power of 100eV electrons on CO molecules on a Ir(111) facet. The bright spots are approximately 10μm in diameter and are due to a different work function present for dissociated CO molecules. This was surprising since CO is generally a stable molecule on this surface and is typically used for surface characterisation on many surfaces. Figure 2b) shows the changes that occur on the surface under $1x10^{-5}$ mbar of oxygen. The Ir(111) facet shows little structural changes and is indicative of an (2x1) oxygen adlayer on the surface. The rough stepped facet on the right of the LEEM image shows micron size structures which are most likely subsurface oxides. Figure c) shows a LEED image from a Ir(111) facet that has had 10L of oxygen at $1x10^{-7}$ mbar adsorbed onto it. This pattern is unlike any other that has been observed on any (111) single crystal surfaces before. It is thought that the boundary conditions are changing the surface energies to allow this as yet unknown structure to be stable.

The oxygen adsorption profiles and CO oxidation reactions have been examined and show significant influences by the surrounding facets and grain boundaries.

References

[Oku06] M. Okumura, Y. Irie, Y. Kitagawa, T. Fujitani, Y. Maeda, T. Kasai and K. Yamaguchi, Catalysis Today 111, Issues 3-4 (2006), Pages 311-315.

[Bau94] E. Bauer, Rep. Prog. Phys. 57 (1994) 895-938.

[Bau01] E. Bauer, J. Phys.: Condens. Matter 13 (2001) 11391–11404

Application of focused ion beam systems to materials analysis

P.R. Munroe and C.H. Kong
Electron Microscope Unit, University of New South Wales, NSW 2052, Australia

Abstract

Focused ion beam (FIB) microscopes are assuming increasing importance in the analysis of a wide range of materials. These instruments provide a large number of analytical possibilities, including the direct analysis of specimen substructure, preparation of thin films suitable for TEM examination and generation of data that allows 3-dimensional projections of specimen microstructure. Moreover, these instruments provide the possibility for nanoscale fabrication.

Introduction

The focused ion beam (FIB) microscope is broadly similar in architecture to the scanning electron microscope (SEM), but uses a fine (~5nm) energetic ion beam instead of an electron beam [1]. Gallium liquid metal ion sources (LMIS) are commonly used in commercial instruments due to their low operating temperature, long lifetime and excellent stability. The controlled scanning of a highly energetic (typically 30 keV) ion beam over selected region of interest (ROI) sputters atoms away from the sample surface, such that trenches, typically a few microns in size are created within a few minutes. Moreover, the interaction of the ion beam with the specimen surface leads to the emission of both secondary ion and secondary electrons which can be used to form images showing the topography of the specimen surface or trench cross-section. A variant of this technique is the dual beam FIB, which synergistically combines a conventional FIB ion column with a SEM-type electron column. This allows simultaneous milling using the ion column with high resolution imaging with the electron beam. Moreover, the electron column can be used to generate characteristic x-rays, photons or backscattered electrons which can be used in a wider range of analyses. The following case studies briefly illustrate a range of FIB applications in finding solutions to materials science problems.

Case Study 1: Direct substructure investigations

Figure 1 shows an example of cross-sectional imaging using a single beam FIB. In this investigation a complex TiN-based coating has been deposited on a steel

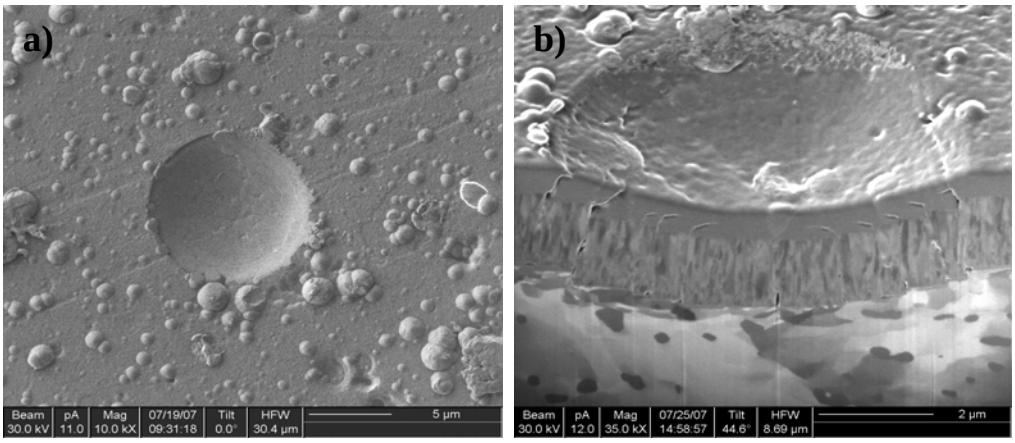

Figure 1: Ion induced secondary electron images of a complex TiN coating on a steel substrate following nanoindentation. Fig 1a shows a plan view image of the indent, fig 1b a FIB-prepared cross-section through the indentation.

substrate. This is then subject to nanoindentation with a spherical indenter to investigate the mechanical response of the costing to contact damage. Figure 1a is a secondary electron plan-view image of the indentation that shows very limited information about the coating, its interactions with the substrate and its behaviour under loading. A cross-section prepared by, and imaged using, the FIB (fig 1b) provides detailed information of thickness of the two coating layers (an outer coating of diamond-like carbon and an inner later of TiN) as well as the steel substrate. The degree of cohesion at each interface, as well as the size and location of the cracks in the various layers, can also be seen.

Case Study 2: Sample preparation for TEM investigation

In general, conventional methods for TEM specimen preparation of material such as ceramics and semiconductor are tedious and often involve low rates of success. Moreover, there is limited control in locating the electron transparent region in the precise region of interest. Figure 2 shows a typical procedure for TEM sample preparation using a FIB. The sample in this case is a polished bulk sample of steel containing a second phase particle, where the thin area needs to include this particle. Semi-automated software is used to prepare the sample, first by using the ion beam to define the region of interest with marker crosses. The gas injection source located in the FIB is then used to deposit a Pt strip, which not only protects the surface of the specimen against the beam damage, but also help to bind the fragile specimen together in the final milling stage. The ion beam is then used to mill an electron transparent section, typically 15 µm x 5 µm x 100 nm. This process typically takes 1-2 hours. The resultant free floating membrane can then be lifted out using a micro-manipulator and deposited onto a standard Cu grid with supporting film of carbon ready for TEM investigation.

Case Study 3: 3D reconstruction of microstructure

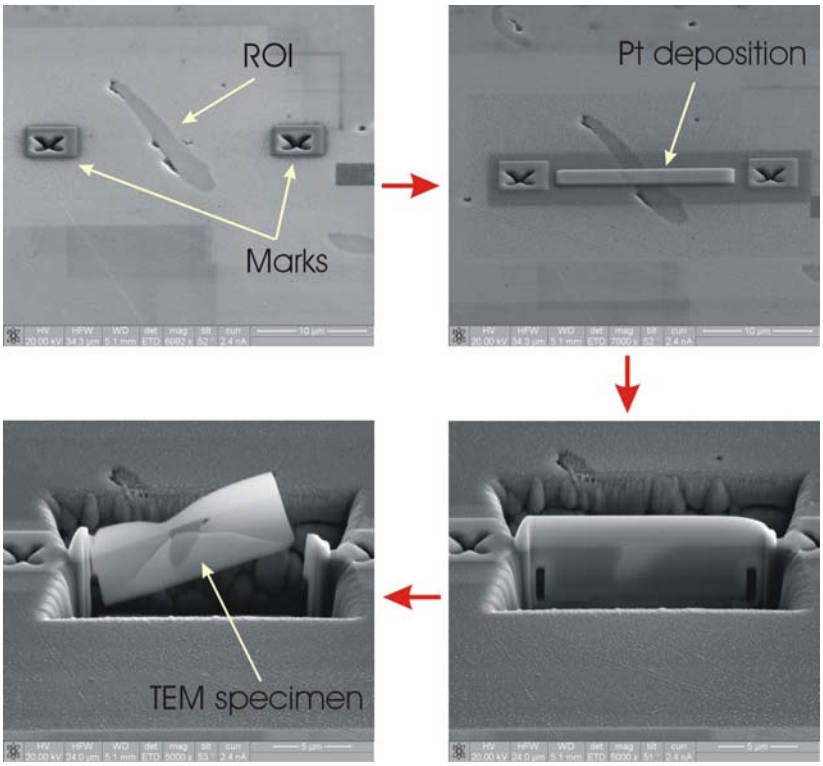

Figure 2: A sequence of secondary electron images which illustrate the procedure for TEM sample preparation with the FIB. The specimen is a steel, where the region of interest is a clearly visible particle in the steel surface. The ion beam can be used to generate an electron transparent section through this precise region.

The dual beam instrument allows sequential sectioning, through the ion beam, and imaging, through the electron beam. As a result, data sets, typically of 100-200 images can be recorded sequentially through a microstructural feature within a few hours. Post acquisition processing can then be used to reconstruct a three dimensional representation of a feature [2].

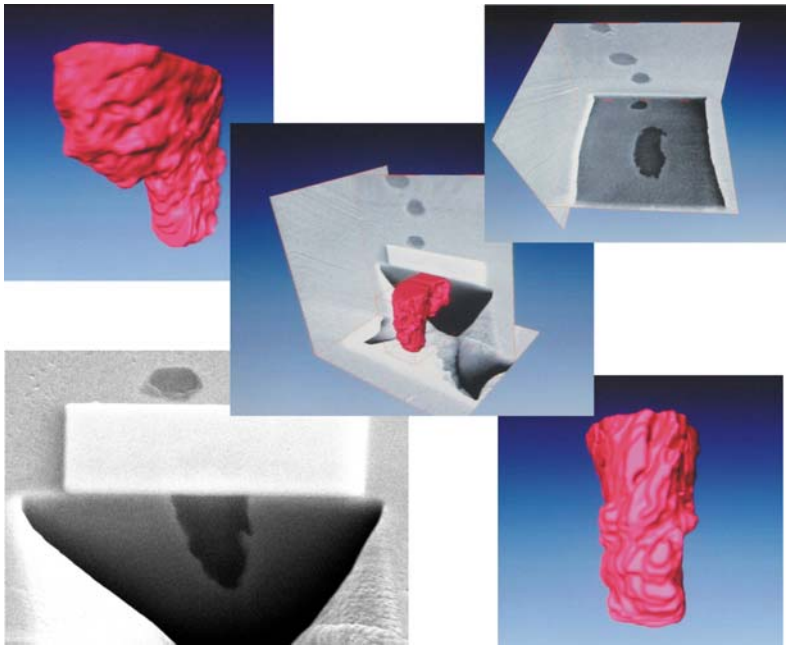

Figure 3: Montage of images showing the reconstruction of a particle embedded in a steel matrix. The red regions show a digitally reconstructed and rendered 3-D visualization.

Figure 3 shows a series of images of a second phase particle located in a steel matrix. Spatial features, such as particles, thin film layers and cracks, can be segmented and designated with a distinguishing colour. This will provide detailed information of specific microstructural features in 3-dimensions.

Case Study 4: Nano-fabrication

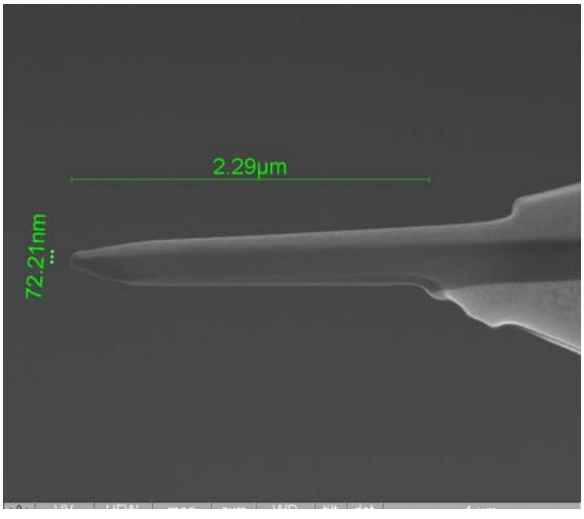

Figure 4: Secondary electron image of a FIB-prepared atom probe post from a thin film structure. The post is prepared with the coating-substrate interface running down the axis of the post.

FIB can be used as a tool to fabricate devices and prototypes at a submicron level. This can be used, for example, to mill sub-micron apertures or gratings to act as filters. More recently, the FIB has been extensively used as a tool for the fabrication of posts for atom probe analysis. These posts have rigorous specimen preparation requirements, including a tip that must be ~ 50 to 100 nm in diameter. The use of the FIB not only allows rapid and reproducible production of these posts, but allows the tip to be prepared from specific regions of interest. Fig 4 shows a FIB-prepared atom probe post in its final stages of preparation.

Final Remarks

The FIB is a highly flexible instrument which can be used to solve materials science problems in a number of ways, either through direct imaging, a tool for specimen preparation or in fabrication of devices.

Acknowledgement

Authors would like to thank AMMRF for financial support. Thanks to Y. Lin, S. Aminorroaya, W. McKenzie for providing part of materials for this study.

References

L.A. Giannuzzi and F.A. Stevie, *Introduction to Focused Ion Beams, Instrumentation*, *Theory, Techniques and Practice*, Springer, (2005).

"3D Microstructural Characterisation Using Focused Ion Beam Tomography", M.D. Uchic, L. Hozler, B. Inkson, E.L. Principe and P.R. Munroe, MRS Bulletin, 32, pp. 408-416 (2007)

Nuclear science and forensic science - complementary sciences !

James Robertson
Australian Federal Police

Is there really such a species as " forensic science " and, if so, why should nuclear scientists be interested in engaging with forensic science professionals ? This presentation will dispel myths about what forensic science is, and what it is not, as perpetuated by the CSI phenomenon ! It will show how in today's world of national and international security why scientists in the " nuclear space " and the " forensic space " need to engage in a synergistic and practical way and it will show how this engagement in Australia is working. Finally, it will describe the recent implementation within the AFP of the Australian Chemical, Biological, Radiological and Nuclear (ACBRNE) Data Centre and its future importance in ensuring these " spaces " are properly connected and driving intelligence through the sharing of technical information.

Presenter: Adjunct Professor James Robertson BSc, PhD, PSM.

Ad /Prof.James Robertson is the National Manager Forensic and Technical for the. During a 30 year plus career James has worked for 10 years as an academic in Scotland, migrated to Australia in the mid 1980's and has led the AFP's forensic group since 1989. He is an Adjunct Professor at two universities and has edited or coedited several books and is widely published in his areas of professional interest. The latter includes trace evidence and illicit drugs. He has a particluar interest in forensic and technical intelligence. James sits on numerous government and academic committees and steering groups. He was awarded the Public Service Medal in 1985 for his services to law enforcement and forensic science.

Radiologically contaminated evidence: extraction procedures and the effect of radioactive materials on forensic DNA profiling

Serena Abbondante [1], David Hill [2], William Maher [3], Cindy Lim [4], Jennelle Kyd [1], Chris Lennard [1]

[1]*National Centre for Forensic Studies, University of Canberra, Canberra ACT Australia,* [2]*Australian Nuclear Science and Technology Organisation, Lucas Heights NSW Australia,* [3]*School of Resource, Environmental & Heritage Science, University of Canberra ACT Australia, 4Australian Federal Police, Weston ACT Australia*

A need has been identified within the forensic science community to investigate the impact of radioactive contaminants on the analysis and interpretation of forensic biological evidence. A possible application of this research includes the response to a terrorist use of a 'dirty bomb', where radioactive material is dispersed with the aid of explosives. The research undertaken investigates: (1) DNA extraction methods for the efficient isolation of DNA from a representative contaminant (with analysis via inductively coupled plasma mass spectrometry), and (2) the damage caused to DNA evidence after exposure to gamma (^{60}cobalt source) and alpha radiation (STAR accelerator).

Traditional and novel methods utilised for DNA extraction merit investigation for the removal of radioactive contaminants while effectively extracting DNA from the biological sample. In addition, considerations need to be made for improvement in time and resource efficiency and suitability for implementation in on-site/mobile processing units. Novel systems, such as DNA IQ (Promega, USA) and ChargeSwitch (Invitrogen, UK), utilise paramagnetic silica beads for the extraction of DNA, and show promise for such applications. These systems have also demonstrated efficiency for the purification of DNA from traditional contaminants found in forensic samples.

These extraction methods were investigated for the efficiency of contaminant removal at levels representative of a radiological incident as well as the quantitative and qualitative effects of the contaminant on DNA analysis. Non-radioactive caesium-133 was introduced to the samples in known concentrations of 0.001M, 0.005M and 0.01M prior to extraction via standard protocols. The recovered caesium concentration was determined using inductively coupled plasma mass spectrometric analysis in both the presence and absence of DNA. In addition, these samples were analysed to assess the quantity of DNA obtained and quality of the DNA profile produced with and without the caesium-133 contaminant. The DNA extracts were profiled with the Amp*Fl*STR Profiler Plus kit (Applied Biosystems, USA). Results have shown a consistent reduction in the level of caesium present in the final purified DNA extract at an efficiency of greater than 99.9% for all concentrations tested. The extraction procedure exhibited an 88-95% removal of contaminating caesium-133, with a significant portion suspected to be adsorbed onto the silica extraction beads ($\leq$ 12%). The addition of DNA did not appear to affect the ability of the system to remove contaminants, and quantitation of the DNA samples and the DNA profiles produced from contaminated samples were consistent with control samples analysed.

The forensic analyst will also need to be equipped with the knowledge to assess the information obtained from biological material that has been exposed to radioactive sources. The interaction of ionising radiation with biological systems results in damage to the cell, particularly to the DNA molecule within. DNA damage is characterised by single- or double-stranded breaks, formation of alkali-liable sites and DNA adducts where there is alteration to the chemical or physical structure of the

DNA. From the known types of damage caused by ionising radiation, there are significant implications for the process of DNA profiling, as successful analysis relies on the integrity and stability of the DNA molecule at specific non-coding regions of the genome.

Biological samples were exposed to various doses of gamma (^{60}cobalt source) and alpha (STAR Accelerator, 5.5MeV) radiation which represent the doses expected at the site of a potential radiological incident. DNA from the samples were extracted, quantitated, and amplified to generate a DNA profile (Amp*Fl*STR Profiler Plus kit, Applied Biosystems USA). DNA profiles from each sample were compared for variation in peak height, allelic dropout, and anomalous peaks. After gamma irradiation, the data generated shows little observable degradation of DNA up to 5kGy for all samples tested. Consistent decreases in peak height and allelic dropout were observed in profiles at and above 10kGy, with complete profile loss at 500kGy. Results obtained from samples irradiated with alpha particles showed an increasing dose significantly reduce the successful production of a DNA profile from $5.9x10^{11}$ Becquerels/cm^2. The DNA profiles from samples irradiated with both gamma and alpha radiation also illustrate that allelic dropout first occurs at higher molecular weight loci. This suggests that the larger sizes of these loci are more susceptible to radiation bombardment, and therefore more likely to incur damage.

From the data generated, the paramagnetic bead extraction systems have shown to be effective for the removal and purification of DNA after contamination with soluble caesium salt. This reflects the potential for its successful application to forensic DNA profiling following a radiological incident. In addition, information has also been obtained demonstrating the likelihood of successful DNA profiling following exposure of the evidence to gamma and alpha radiation.

Keywords: DNA profiling, DNA damage, extraction, radioactive materials, gamma radiation, alpha radiation

A new methodology in prosthesis research: radioisotope tracing of knee implant wear

Laura G. Gladkis [1,2], Jennie Scarvell[2], Paul Smith[2], Heiko Timmers[1]

[1]School of Physical, Environmental and Mathematical Sciences, UNSW@ADFA, Canberra, ACT 2600
[2]Trauma and Orthopaedic Research Unit, The Canberra Hospital, PO BOX 11, Woden, ACT 2606

The incidence of knee replacement surgery in Australia (~30,000 per year) is rising annually by about 10% [1]. Limited by wear debris the medical lifespan of a knee implant is only 10-15 years and can be as short as 2-3 years in some cases [2]. Due to increasing life expectancy, and due to medical complications caused by wear debris, enhanced wear resistance of knee implants will reduce overall health costs and will benefit patients' quality of life.

Particulate wear debris from the UHMWPE (ultra-high molecular weight polyethylene) component of the implant typically causes the inflammatory reaction that breaks down bone around the prosthesis and limits its lifespan. Previous measurement attempts of wear in surgical implants using mass loss or geometrical techniques have drastically been lacking in sensitivity.

We investigate a new methodology which promises to be more sensitive and may allow the characterization of wear debris shedding on the nanometer-scale. In our approach, radioisotope tracers are introduced into prosthesis materials and wear rates are derived by detecting the radioactivity of the prosthesis lubricant during laboratory simulation. The radioisotope tracer chromium-51 with a half-life of 27.7 days is well suited for this work. It is aimed to place the tracer atoms in the materials using three different techniques, at minimum atomic concentration and with negligible material modifications, however, with detectable activity. In combination with atomic force microscopy [3,4] this methodology may allow the detailed measurement of early wear phenomena and possibly debris tagging.

Wear debris from knee prosthesis

Figure 1 shows an x-ray image of a knee implant following replacement surgery. The femoral component (Cocr) articulates a wear surface made of UHMWPE, which is the established bearing material for knee prostheses [5].

PE is superior to any other bearing material. However, for each day of patient activity around 100 million microscopic debris particles are released into the tissue surrounding the implant [5]. UHMWPE particulate debris is found in the synovial fluid bathing the implant, in the cellular tissue lining the joint, in the bone, and in the soft tissues of the knee. The debris activates cells that engulf, and then digest, the debris particles as foreign material. These cells (macrophages) then release waste material (cytokines), which is the mediator of the inflammatory reaction. This stimulates a response within the bone tissue (osteoclasts), leading to the gradual resorption of bone tissue at the bone/cement or bone/prosthesis interface, eventually causing loosening of the implant [6]. This is painful for the patient and inevitably the prosthesis has to be replaced by additional surgery [7].

New Methodology

Green *et al*. [8] have shown that the most biologically active polyethylene wear particles are in the size range 0.3 - 10 μm. The time, origin and rate of debris production in knee prosthesis are, however, poorly understood. Our new methodology is described below.

1) Introduction of the radioisotope tracer into UHMWPE

The radioisotope tracer may be introduced into the tibial component of the prosthesis via: (i) admixture during manufacture, (ii) diffusion, or (iii) ion implantation. ^{51}Cr, a gamma-ray emitter (E_γ = 320 keV) with $t_{1/2}$ =27.7 days is well suited for this work, since its half-life matches the time-scale of a typical wear study. Each introduction procedure has advantages and poses challenges. Admixture during manufacture, (i), requires collaborative arrangements with a commercial producer of knee implants to ensure that the properties of the doped tibial UHMWPE component are identical to those of their product. However, uniform tracer concentrations throughout the component can be achieved and the mass- and volume-change during wear simulation may thus be measured.

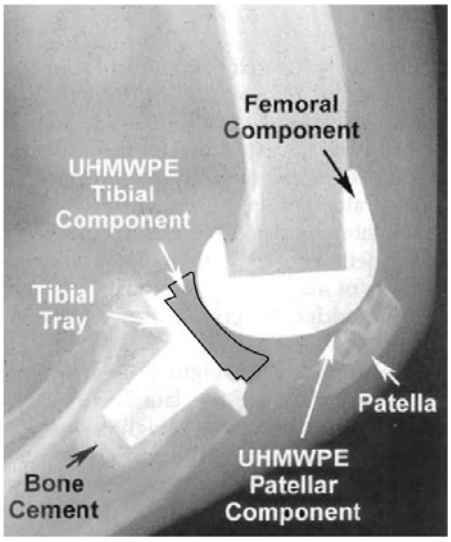

Figure 1: x-ray of knee implant: Bone resorption due to particulate debris loosens the implant.

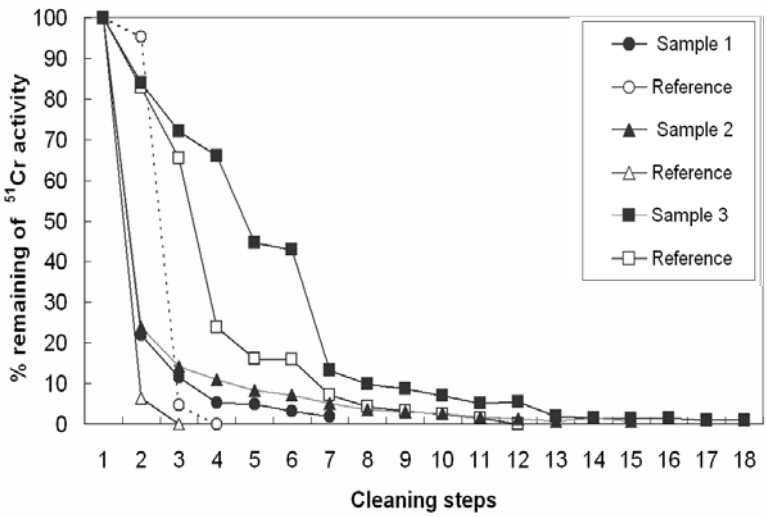

Figure 2 :51Cr Activity remaining on 3 samples kept three days in an oven at 100°C in comparison with reference samples.

The diffusion of radioisotope tracers into UHMWPE, (ii), is untested. Only low annealing temperatures below 100°C may be considered, however, near-surface concentrations at depths of less than 100 nm are sufficient and, in fact, desirable for the measurement of wear effects on the nanometer scale.

The ion implantation of the radioisotope tracer, (iii), combines shallow depth-profiles with the possibility of lateral resolution [10]. Both direct implantation, at energies of 100 - 150 keV, and recoil implantation following production via nuclear fusion evaporation reactions at energies of 10 - 50 MeV, may be considered. In the first case a 50 nm surface layer of the material may be labelled, whereas in the second case a thin layer of material at a depth in the range of 500 - 1000 nm may be labelled with the radiotracer, respectively.

Preliminary work

In preliminary experiments the diffusion of the radioisotope tracer ^{51}Cr has been studied. 0.02 ml of ^{51}Cr in solution, obtained commercially from Perkin and Elmer, were placed inside a circular positioning ring onto 6 UHMWPE samples. The samples were then dried overnight under a heat lamp, and 3 of the samples were kept in a furnace at a constant temperature of 100°C for 5 days to induce the diffusion of the tracer. After removal from the furnace the positioning ring was also removed and the ^{51}Cr-activity of the samples was measured using NaI-scintillation detectors. This was followed by a series of identical cleaning attempts using cotton balls and ethanol and repeated measurement of the remaining gamma ray activity.

Figure 2 shows the results and demonstrates that 99%± 1% of the ^{51}Cr activity did not diffuse into the material, but remained at the UHMWPE surface. Further studies will explore different diffusion regimes and attempt to quantify less than 1% of the initial ^{51}Cr activity in order to verify what fraction, if any, of the ^{51}Cr diffuses into UHMWPE.

2) Articulation of the UHMWPE wear surface

The wear of knee prosthesis components is studied using a constant force and a more realistic commercial knee simulator allowing more realistic articulation cycles.

Preliminary work

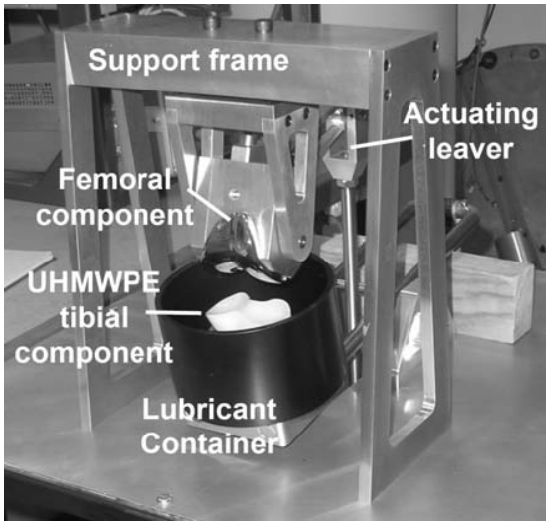

Figure 3: Constant load knee motion simulator for radioisotope tracing studies of prosthesis

The constant force knee simulator (see Figure 3) has been design and constructed at University of New South Wales at ADFA. Such a simple design was chosen to produce reproducible wear patterns reliably. The axial force (load applied from below) can be adjusted over a range of 0-1000 N, and flexion angles of 24o, 38o, 51o and 66o can be set. The UHMWPE wear surface is articulated at a rate of 1 cycle per second. The knee simulator was commissioned using a pristine knee implant from Depuy, with water as lubricant. It was found that the simulator operate reliably over up to 1.2x106 cycles at various loads and flexion angles, and that wear debris could successfully be removed from the lubricant. Figure 4 compares (a) flexion angles and (b) axial force for the constant load knee simulator with those of a more realistic simulation (data from [11]).

3) Characterization of debris in the synovial fluid

In regular intervals, the lubricant is removed from the simulator. The prosthesis components are weighed and particulate debris is characterized. Ultimately the activity of the radiotracer will be measured.

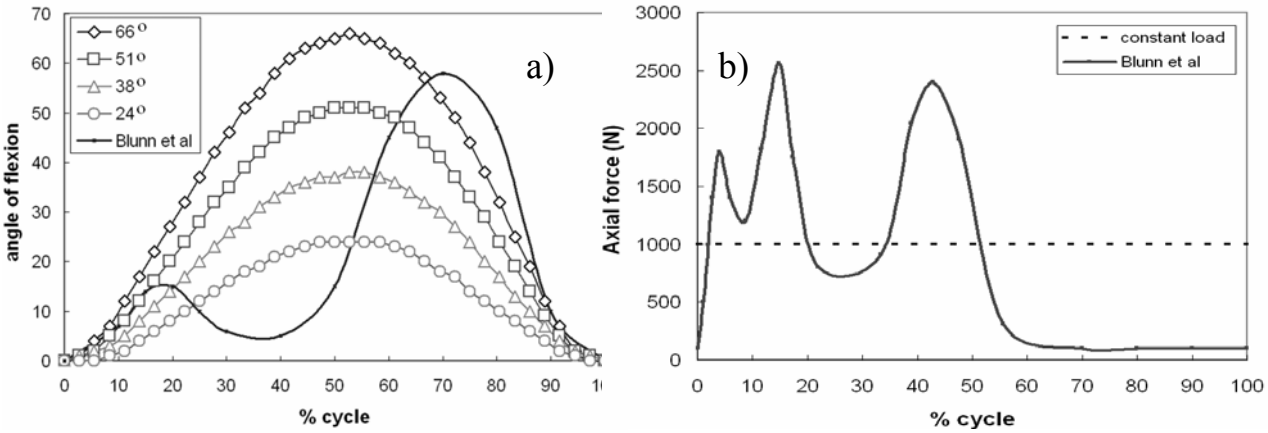

Figure 4: (a) Angle of flexion and (b) axial force comparison for the constant load knee simulator, and a more realistic simulation measured by Blunn et al.[10]. The x-axis represents a single walking cycle.

Preliminary work

Illustrating a typical result, Figure 5 shows the mass loss of a UHMWPE tibial component as a function of simulation time, for different angles of flexion and loads. The component mass was determined by weighing with an accuracy of better than 0.001 g following drying under a heat lamp over 2 hours. The measured wear rate is an order of magnitude larger than expected. This may be attributed to the deliberate application of a relative large axial force at maximum flexion angle, leading to shear load and scraping of the wear surface. The debris particulates from these preliminary simulations may, however, still be expected to be similar to more realistic conditions and can thus serve to verify the new methodology. A state-of-the-art knee simulator is currently acquired to produce wear debris under more realistic conditions approaching those in a patient.

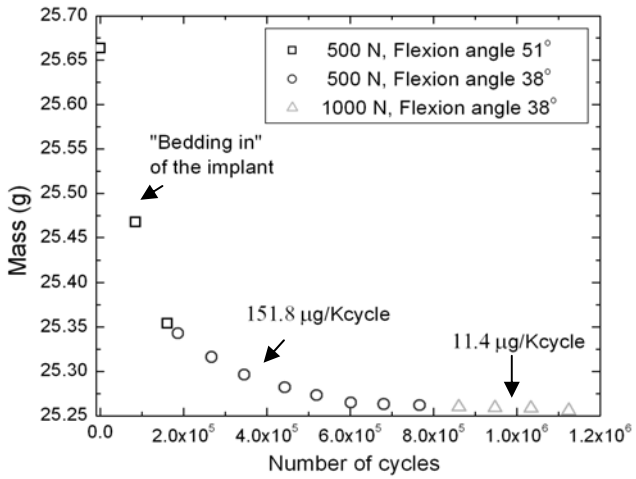

Figure 5: Mass of a UHMWPE tibial component as a function of cycles on a knee motion simulator.

Green *et al.* [8] and other authors characterize biologically active polyethylene particles by filtration and SEM. The capability of atomic force microscopy of directly determining the spatial dimensions of a polyethylene particle, however, has only be applied in few studies [9]. In the present study atomic force microscopy has been used to measure the particles dimensions.

Debris particles suspended in the lubricant (H_2O) have been characterized using AFM in semi-contact mode, after a drop of the lubricant was dried on a clean silicon surface. Figure 6 shows typical images which allow the assessment of debris dimensions. Two types of particulate debris may be distinguished. Figure 6 (a) shows that clumps (C) with typical diameters of 5 µm fall well inside the biologically active range. Fibrils (F) have a much smaller overall volume with elongations ranging from 0.5 to 10 µm and typical diameters of less than 300 nm, as apparent in the three-dimensional visualization of AFM data in Figure 6 (b).

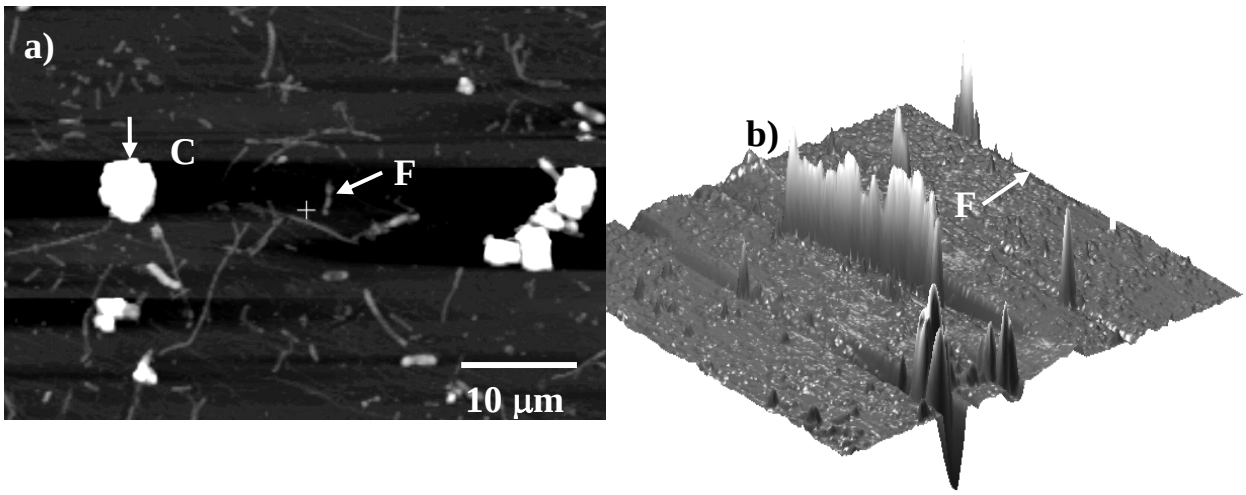

Figure 6: (a) Two-dimensional AFM image of UHMWPE debris. Note the two types of shapes: clumps (C) and fibrils (F). (b) Three dimensional representation of AFM data. A typical fibril is indicated.

Conclusions

A new methodology for measuring the wear performance of knee prostheses is being studied. Preliminary diffusion studies demonstrated that (99±1) % of the ^{51}Cr activity did not diffuse into the material, but remained at the UHMWPE surface. A knee simulator was successively commissioned using a pristine knee prosthesis. It was found that the simulator operates reliably over up to $1.2x10^6$ cycles at various loads and flexion angles, and that wear debris particulates can be obtained. It has also been shown that atomic force microscopy is well suited to characterize nanometre size UHMWPE particles. Two types of particulate debris, clumps and fibrils, have been distinguished in the lubricant.

References

[1] Australian Orthopaedic Association, Annual Report, 10, Tab. G4,ISSN 1445-3657 (2005)

[2] John A.L. Hart, Medical Journal of Australia, 180, S27-S30 (2004)

[3] A.P Elfick et al., Wear 253 (2002) 839-847

[4] S.P. Ho et al., Wear 253 (2002) 1145-1155

[5] S. M. Kurtz, The UHMWPE Handbook, Elsevier Press (2004)

[6] A.L. Galvin et al., Wear 259 (2005) 977-983

[8] T.R. Green et al., Biomaterials 19 (1998) 2297-2302

[7] C. Kowandy et al., Wear 261 (2006) 966-970

[9] M. Scott et al, J Biomed. Mater. Research B 73 (2005) 325-337

[10] S.K. Shrestha et al., Hyperfine Interactions, DOI 10.1007/s10751-005-9067-6 (2005)

[11] G.W. Blunn et al., Friction, lubrication and wear of artificial joints, P. E. Publishing (2003)

Cylindrical silicon-on-insulator microdosimeter: charge collection characteristics

A.L. Ziebell [1], W.H. Lim [1], , M.I. Reinhard [2], I. Cornelius [2], D.A. Prokopovich [1], R. Siegele, A.S. Dzurak [2], and A.B. Rosenfeld [3]

[1]Student Member IEEE, [2]Member IEEE, [3]Senior Member IEEE

Introduction

At present there exists a need, in both medical physics and radiation protection, for a portable microdosimeter that can be used in determining the radiobiological effectiveness (RBE) of different mixed radiation fields. The microdosimetric approach to this determination is based upon obtaining the spectrum of lineal energy events, $f(y)$, in a micron sized site produced by secondary charged particles generated during the exposure of tissue to ionizing radiation. With knowledge of $f(y)$ the RBE is calculated using $\int Q(y)y^2 f(y) d\log y$, where $Q(y)$ is a quality factor obtained from radiobiological experiments [1,2]. Experimental measurements of $f(y)$ require a radiation detection instrument with a sensitive volume equivalent in size to a biological cell. Traditionally gas proportional counters have been used; however these have a number of well documented failings [2].

Recent efforts to produce a solid state microdosimeter include a semiconductor-on-insulator (SOI) based device developed at the Centre for Medical Radiation Physics at the University of Wollongong, Australia [3]. This device consisted of a 2D diode array of elongated parallelepiped shaped micron sized volumes. The device was tested for applications in radiation therapy [4-6] and in radiation protection [7]. Due to the sensitive volume geometry the device was found to have a poorly defined average chord length for isotropic radiation fields. Additionally the response of the device as a microdosimeter suffered due to the unwanted diffusion of charge from outside the defined sensitive volume [8]. Other attempts to realize a solid state microdosimeter also suffer from the limitations of the elongated parallelepiped design [9].

We present a solid state microdosimeter with a cylindrical sensitive volume fabricated as a physically and electrically isolated structure. This design allows for a reduced variance in the average chord length of the sensitive volume, with charged particles incident at varying angles to the sensitive volume, as well as a decrease in the amount of lateral charge diffusion.

In this study the electrical characteristics of the device are presented along with the results of an ion beam induced charge collection (IBICC) study.

Materials and Methods

The Device

Schematics of the detector structure are shown below in figure 1. Fabrication of the device employed planar processing techniques on a p^{--} silicon on insulator (SOI) wafer. Phosphorus and boron were diffused into the silicon wafer to produce p-n diode structures possessing coaxial geometry. The P diffusion formed an axial n^+ region separated from the B diffused coaxial p^+ region by an intrinsic p^{--} sensitive volume of width, w. The silicon external to the p^+ region of each diode was removed through an etching process to create a mesa structure 2 μm in thickness (t). In production two versions of the test structure were fabricated with sensitive region widths of 2μm and 10μm respectively. Each substrate contained 10 individual diodes.

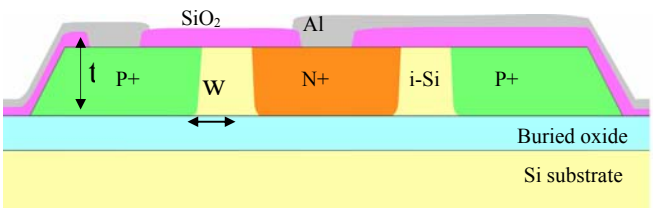

Fig. 1. A cross sectional schematic of the microdosimeter. The size of the sensitive volume is equivalent to the size of a cell nucleus. Note the cylindrical nature of the design.

Experimental Setup

The electrical properties of the diodes were determined using conventional IV and CV testing with a Keithley 6517A electrometer and a Boonton 7200 capacitance bridge. All measurements were performed under vacuum at room temperature to allow for reproducible conditions.

The charge collection characteristics of the device were experimentally measured using the Australian Nuclear Science and Technology Organisation (ANSTO) heavy ion microprobe. The microprobe was used to produce a 3 MeV beam of He^{2+} ions focused to a diameter of approximately 1.0 μm. The amount of energy deposited within the microdosimeter during each ion traversal, E, was measured with a standard charge sensitive preamplifier and shaper. The signal was fed directly into an ADC channel of the data acquisition system in coincidence with signals indicating the beam position, x and y. Data triplets (x,y,E) were saved for each event in a list mode file. Using this data IBICC imaging maps were generated to display the median charge collected, and the number of collected events within a desired energy range, as a function of beam position. The aim of using these maps was to observe the geometrical boundary of charge collection within each device, draw conclusions about the uniformity of the device thickness, and identify any other features that may produce artefacts within the subsequent microdosimetric spectra.

Results and Discussion

IV and CV

The typical reverse current for diodes on both the 2μm and 10μm device were not greater than 3.0pA at an applied reverse voltage of 9V. The capacitance per unit area was found to be ≈ 0.5 $pF{\cdot}um^{-2}$ under the same conditions, a high value due to the 2 μm depletion width.

IBICC Results: 2 μm Device

An energy spectrum of the 2 μm wide microdosimeter device in response to the 3 MeV He^{2+} ions is shown in figure 2. A peak can be seen at an energy of approximately 500 keV. The expected energy loss of a 3 MeV He^{2+} ion in 2 μm of silicon is 400 keV (196 keV/μm). The origin of events at energies below the peak can be understood in terms of the spatial location of the ion strike as discussed below.

Figure 3 shows a median energy map of the charge collected during a scan of the 2 μm device. The location of events with high median energy collection are shown in red forming an annulus. These events correspond to the charge collection under the drift of the applied electric field. The uniform nature of the energy implies a uniform thickness of the microdosimeter throughout this region. The small central region of low median energy events shown as blue corresponds to the presence of the axial n^+ region of the device.

At the outer perimeters of the diode another region of low median energy events can be seen. These low energy events correspond to ion strikes incident upon the coaxial

p^+ region external to the intrinsic silicon. These events are thought to result from the diffusion of charge from the p^+ region into the radial electric field region of the diode. No events were observed from outside of the diode mesa structure external to the intrinsic silicon. These events are thought to result from the diffusion of charge from the p^+ region into the radial electric field region of the diode. No events were observed from outside of the diode mesa structure.

Conclusion

A new design for a solid state based microdosimeter with micron sized sites typical in size to a cell nucleus was presented. Charge collection mapping of the individual diodes demonstrated a well defined region of complete charge collection corresponding to a true micron sized sensitive volume. The mesa structure design was successful in eliminating unwanted diffusion of charge from outside of the sensitive volume.

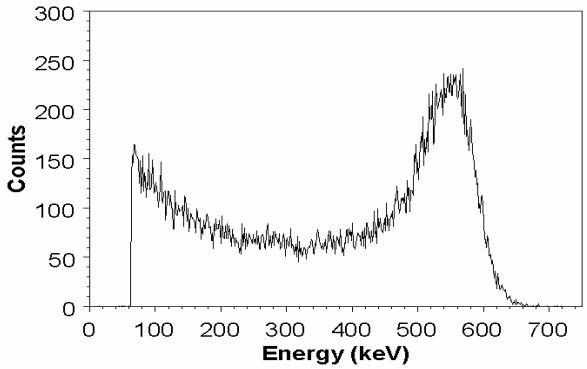

Fig. 2. Energy spectrum of the 2 μm microdosimeter device in response to 3 MeV He^{2+} ions.

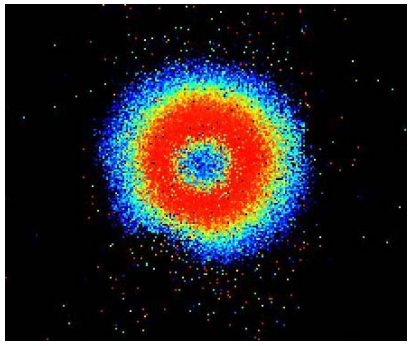

Fig. 3. The median energy map of the charge collected (calibrated in terms of energy) during a scan of the 2 μm device.

In the full paper additional results of IBICC testing with 3 MeV and 5.5 MeV He^{2+} ion beams will be presented for both the 2 μm and 10 μm wide diodes along with IBICC results for proton and carbon ion beams. Device simulations using GEANT4 will also complement the presented experimental results.

References

H.H. Rossi et al., "Microdosimetry and its Applications," Springer (1996)
ICRU Report 36, "Microdosimetry," Bethesda, Maryland (1983).
P. D. Bradley, "The Development of a Novel Silicon Microdosimeter for High LET Radiation Therapy," Ph.D. Thesis, Department of Engineering Physics, University of Wollongong, Wollongong, Australia, 2000.
P.D. Bradley, et al., "IPerformance of silicon microdosimetry detectors in boron neutron capture therapy," Radiation Research, vol. 151, pp. 235-243 (1999).
A.B. Rosenfeld, et al., "Solid state microdosimetry in hadron therapy, "Radiation Protection Dosimetry, vol. 101, pp. 431-434 (2002)
A.B. Rosenfeld, et al., "A nuclear detector for microdosimetry applications in proton therapy," IEEE Transactions on Nuclear Science, vol 47, pp.1386-1394 (2000)
M. Reinhard et al., "Response of a SOI microdosimeter to a 238PuBe Neutron Source," 2005 IEEE NSS Conference Record
I. Cornelius, et al., "Ion beam induced charge characterisation of a silicon microdosimeter using a heavy ion microprobe," NIM B, vol. 190, pp. 335-338 (2002)
A. Fazzi, et al., "A microdosimetric thickness silicon diode proposed as a microdosimeter," IEEE Transactions on Nuclear Science, vol 53, pp.312-316 (2006)

Australian Synchrotron

Dr Julian Adams
Principal Beamline Scientist
Protein Crystallography
Australian Synchrotron

The Australian Synchrotron is a new 3rd generation synchrotron source. The initial funding covered the construction of the machine and nine beamlines of which two are dedicated to Protein Crystallography. Protein crystallography is the largest single science user of synchrotrons world wide. Details of the construction, commissioning, user operations of the two protein crystallography beamlines will be presented.

NanoSIMS – Recent advances and new applications in SIMS

Matt Kilburn
[mkilburn@cyllene.uwa.edu.au]
Centre for Microscopy, Characterisation and Analysis, University of Western Australia

Recent advances in SIMS instrumentation have fostered new applications in biological, materials, and earth sciences, where high spatial resolution is required. The novel design of NanoSIMS allows high spatial and high mass resolution to be achieved while maintaining high sensitivity and transmission. A multi-collection system enables the detection of up to five species or isotopes simultaneously. This has made it possible to map elemental and isotopic tracers in biological samples at sub-cellular scale, oxide growth in stress corrosion cracks, isotopic measurements of micron-sized particles, and interface mechanics in semiconductor materials. These and other examples will be presented in this talk.

+61 (0)8 6488 8068 office

+61 (0)8 6488 8082 nanosims lab

Ion-beam sputtered germanium thin films – self-assembly of surface nanostructure using post growth annealing

Damian Carder [1], Andreas Markwitz [1,2] and H. Baumann [1]
1 National Isotope Centre, GNS Science, Lower Hutt, New Zealand
2 The MacDiarmid Institute for Advanced Materials and Nanotechnology, New Zealand

d.carder@gns.cri.nz

Presented here is a study into the self-assembly of Ge nanostructures using ion-beam sputtering followed by a rapid and uncomplicated post-growth annealing method. The aim of the work is to produce controlled and predictable assembly of the surface features, central to the development of any application.

Our group has recently demonstrated the nanostructuring of untreated Si substrates using an electron beam annealing (EBA) technique [1], with the so-called nanowhisker surface structure showing immediate promise in field-emission and vacuum electronics applications [2].

Experimental: Ion-beam sputtered layers of Ge, ~200-400 nm thick, were deposited near room temperature on a Si substrate. The ion sputter system was operated at a base pressure of better than 2×10^{-7} mbar, with an argon gas ion source operating at 1mA. The Ge films were annealed at temperatures ranging from 400°C up to 700°C using the GNS electron beam annealing (EBA) technique.

Results and Discussion: Atomic force microscopy (AFM) measurements were made using an Easyscan 2 AFM from Nanosurf. Figure 1(a) shows an AFM image of the as-deposited Ge surface. In contrast, figure 1(b) shows the scan of the surface after annealing at 550°C for 15s. It is evident from figure 1 that a dramatic surface roughing on the nanoscale has occurred due to the annealing process. Figure 2 shows the average surface roughness calculated from AFM images of Ge films after annealing for 15s at temperatures from 400°C to 700°C.

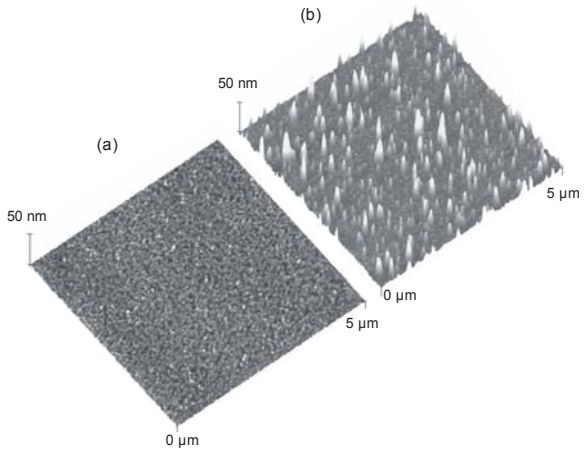

Figure 1: Atomic force microscope images of a sputtered Ge film (a) before and (b) after electron beam annealing.

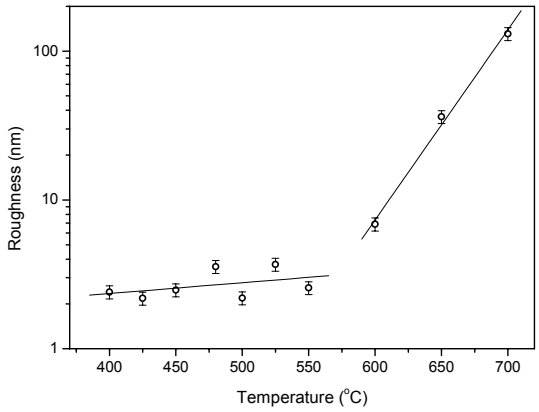

Figure 2: Roughness analysis of Ge films after electron-beam annealing at temperatures 400°C to 700°C. Lines are drawn through the data to provide a guide for the eye.

Between 400 and 600°C the roughening is an order of magnitude higher than the as-deposited surface layer but remains relatively constant in this region. Over an interval of 100°C (600 – 700°C) the surface roughening increases again to a value three orders of magnitude greater than the pre-annealed value. Further analysis of the height distributions for the nanostructures reveals a large characteristic difference for samples annealed above and below 600°C. At the lower temperatures the nanostructures are all below 50nm whereas larger nanofeatures form at 700°C, with a distribution of heights centred at 450nm [3].

To further investigate the larger feature size at higher temperatures, we performed Rutherford backscattering spectroscopy (RBS) measurements. The experimental details are as detailed in [4], where simulation of the RBS data was performed using the RUMP software program [5].

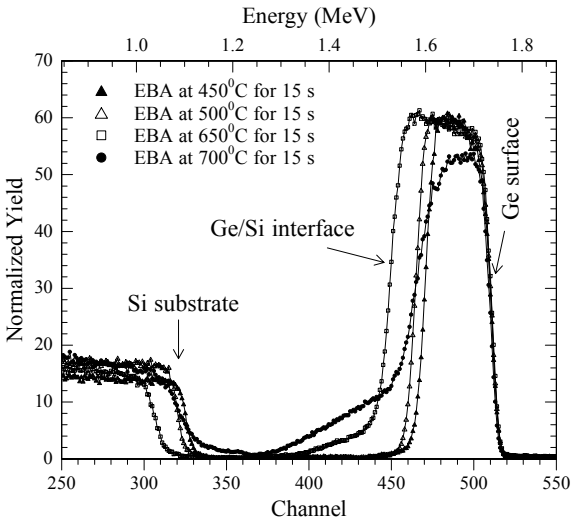

Figure 3: RBS spectra of selected Ge films after annealing.

Figure 3 shows the RBS spectra of four annealed Ge films. The position of the Ge surface, Ge/Si interface and Si substrate are indicated. Notably, the regions of the Ge/Si interface (1.3 - 1.6MeV) and Si substrate (~1.1MeV) show distinct changes as the annealing temperature is increased. At the lower temperatures (450 and 600°C) the Ge/Si interface is abrupt (at 1.6MeV), in contrast to the higher temperatures (650 and 700°C) where the data shows a pronounced gradient across energies of 1.3 to 1.6MeV. Similarly, the gradient is more abrupt for the lower temperatures at the Si substrate. Both these observations show significant intermixing of Ge and Si across the film/substrate interface. It is noted that the film thickness varies between samples. However this does not account for the simulated differences in the following analysis.

The general features of the film annealed at 450°C are shown in detail in figure 4, assessed from a simulation of the measured spectra.

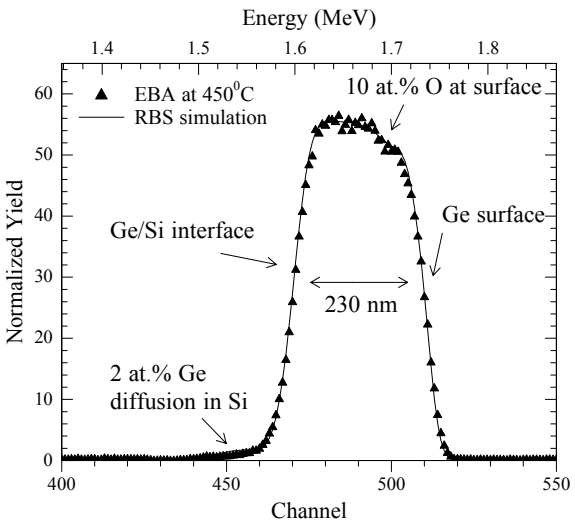

Figure 4: Measured RBS and simulation spectra for the sample annealed at 450°C.

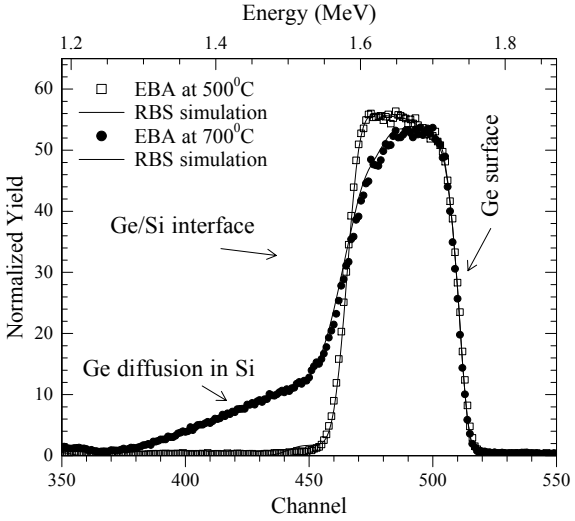

Figure 5: Measured RBS and simulation spectra for samples annealed at 500 °C and 700 °C.

A surface layer of $Ge_{0.9}O_{0.1}$ is observed for all samples. The 450°C sample had a film thickness of 230 ± 5 nm. Similar analysis for the sample annealed at 500°C resulted in a film thickness of 260 ± 5 nm. It is notable that even at 450°C a 2 at. % diffusion of Ge, extending 180 ± 5 nm, into the Si substrate is observed. This diffusion becomes more pronounced at the higher temperatures, where a comparison between the 500°C and 700°C sample is shown in figure 5. For the sample annealed at 700°C there is significant diffusion and intermixing of the Ge into the Si substrate, which is illustrated further in figure 6. It is notable that some Si (5%) has diffused through to the uppermost layer. The Ge content reduces from 95% to 4% across a thickness of around 650 ± 5 nm. The significant intermixing alters the strain distribution between the film and the substrate which leads to the formation of larger surface features. A similar shift in size distribution has been observed by Jin et al [6] during MBE growth of Ge on a heated Si substrate above a temperature of 600°C.

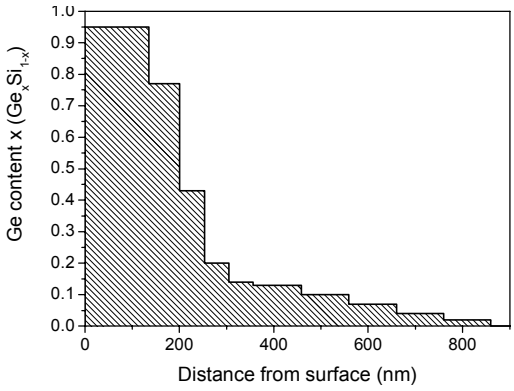

Figure 6: Simulated Ge content of layers for the sample annealed at 700 °C. The distance from the surface (excluding the ultra-thin GeO layer) is plotted on the x-axis.

The authors wish to acknowledge the technical assistance of J. Kennedy, J. Futter and C. Purcell.

This project is funded by a research contract with the Foundation for Research Science and Technology of New Zealand.

References

[1] S. Johnson, A. Markwitz, M. Rudolphi, and H. Baumann, J. Appl. Phys. 96, 605 (2004)

[2] S. Johnson, A. Markwitz, M. Rudolphi, H. Baumann, S. P. Oei, K. B. K. Teo and W. I. Milne, Appl. Phys. Lett. 85, 3277 (2004)

[3] D.A. Carder, A. Markwitz, H. Baumann, and J. Kennedy, Current Applied Physics, accepted for publication August 2007

[4] V. John Kennedy, A. Markwitz, U.D. Lanke, A. McIvor, H.J. Trodahl, A. Bittar, Nucle. Instru. and Meth. B190 (2002) 620

[5] RUMP (program), http://www.genplot.com/

[6] G. Jin, J.L. Liu, and K.L. Wang, Appl. Phys. Lett. 83 (2003) 2847

Interface trap density reduction in thin silicon oxides using ion implantation

Michael Dunn [1], Dr. Jeff McCallum [1], Eric Gauja [2]
[1] *Centre for Quantum Computer Technology, University of Melbourne, Australia*
[2] *Centre for Quantum Computer Technology, University of New South Wales, Australia*

The reduction of interface charge trap density is important in the manufacture of semiconductor devices such as MOSFETS, and for the successful construction of a silicon based quantum computer using single ion implantation. These devices require very thin oxides (<10 nm) in order to obtain high readout sensitivity. However, thinner oxides are also sensitive to oxide integrity so techniques such as rapid thermal annealing (RTA) are used to improve the electrical characteristics. The density of charge traps at the interface between the oxide and semiconductor (Fig 1) is a key measure of oxide integrity. A relatively low density is desired as this generally improves device characteristics.

Interface traps arise due to inherent structural defects, or by radiation processes which cause bond-breaking. In a silicon-oxide interface these defects correspond to trivalent silicon bonds, or "P_b centres" that arise as bonds transfer from the bonding configuration in the crystalline Si to that of the amorphous silicon dioxide. For longer growth times (creating thicker oxides) the interface trap density is reduced as the traps are concentrated only at the interface. These traps are physically localized, but have a continuous spectrum of energy levels and are therefore different to traps found within bulk silicon which have distinct energy levels, at a range of locations in the band gap [1].

Growth of silicon oxide nearly always includes a thermal annealing step which reduces the interface trap density by up to two orders of magnitude depending on anneal settings and the specific sample [2]. Further reduction may be obtained if ions are implanted into the sample as noted by Afanas'ev for F ions implanted to stop in the oxide [3]. Peterstrom observed an increase in interface trap density for B and P implants into Si through SiO_2 [4].

In contrast to the Peterstrom study, this paper presents results that indicate ion implantation through the oxide can significantly reduce interface trap density, and finds neither significant ion species nor fluence dependency on the level of reduction.

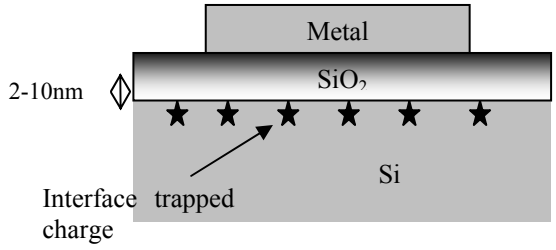

Figure 1. MOS device structure

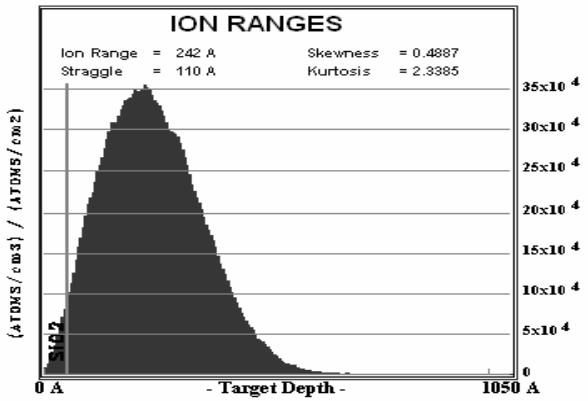

Figure 2. SRIM data for 14keV P implanted through 7 nm SiO_2 layer

Experimental Procedure

Si oxide layers were thermally grown in a triple wall oxidation furnace to thicknesses of 5 nm and 7 nm. Samples were passivated in forming gas for 15 min at 400 °C. P, Si and SiN ions were each implanted through the oxide at respective energies of 15 keV, 15 keV and 20 keV, for a range of fluences between 109 ions/cm2 and 1012 ions/cm2. 15 keV P was used due to its importance in the silicon quantum computer development; Si to compare if the observed effect was ion species dependent or damage related; and SiN as a third species with the N component being of interest. 20 keV ensured that the N atoms had a similar stopping range to the other two implant species. SRIM (Stopping Range of Ions in Matter) data (Fig 2) show that P atoms come to rest at an average depth of ~240 Å below the surface of the oxide. The other species show a similar predicted range. Following implantation, samples underwent a 5 s RTA at 1000 °C, followed by a H-passivation anneal at 400 °C, 15 min in N_2 (95%)/H_2 (5%) and then 110 µm diameter Al contacts were deposited.

Electrical analysis was carried out using Deep Level Transient Spectroscopy (DLTS). Spectra are obtained by taking the sample into depletion with a 2.0 V bias, then applying 4.0V, 40 ms pulses at 1000 ms intervals and measuring the transient behaviour as charges are emitted from the electrical traps. Capacitance-Voltage and Capacitance-Temperature scans are also performed which together with DLTS spectra allow interface trap density to be obtained.

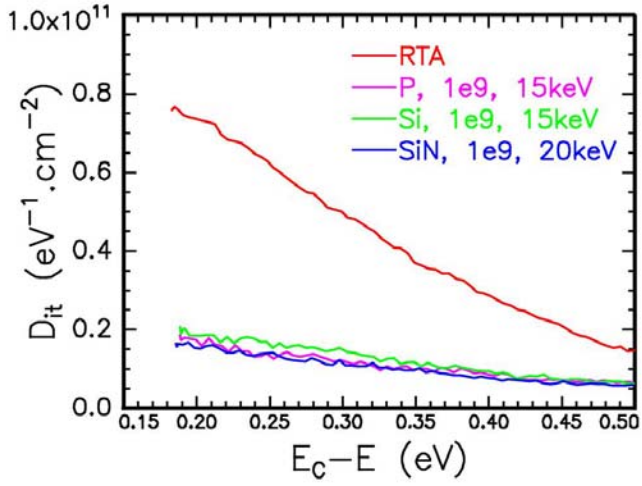

Figure 3. Interface trap density (Dit) of 7 nm silicon MOS device after various ion implantation.

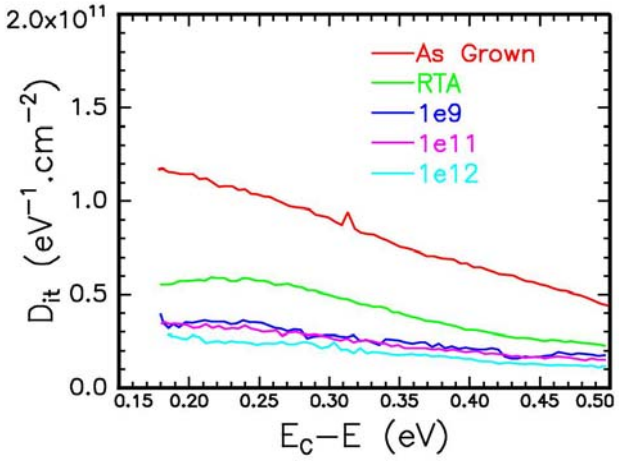

Figure 4. Interface trap density of MOS device after 14 keV P ion implantation at various fluences

Results

Results for the three ion species at a fluence of 109 ions/cm2 are shown in Fig 3, with interface trap density (Dit) presented as a function of energy. The "RTA" sample underwent all of the same processing steps, including RTA, but was not ion implanted. After implantation there is a significant reduction in interface trap density for all three ion species. Furthermore, this reduction does not seem to be dependent on the type of ion implanted.

Comparison of samples with different implanted fluences is shown in Fig 4. No significant fluence dependency is observed indicating that if a threshold fluence exists it is less than 109 ions/cm2. A similar lack of fluence dependency has also been observed in Si and SiN.

CV curves of the non-implanted samples feature an unusual capacitance 'hump' as the sample is biased into depletion (Fig 5). After implantation the hump is no longer present indicating that the mechanism causing the capacitance hump could be linked to the reduction in interface traps.

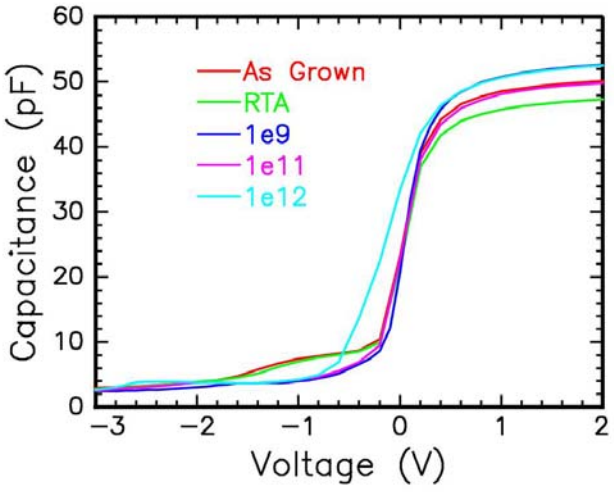

Figiure 5. Capacitance-Voltage curves for 7 nm silicon MOS device before and after implantation of 15 keV P ions

The lack of ion species dependency suggests that the damage caused by implantation is responsible for the reduction in density. It is thought that the incident ions trigger a reorganization of the bonds at the interface such that a more energetically favourable structure is obtained with fewer charge traps. Further work will include a study of ion energy dependence and whether the associated stopping range has an effect on the reduction of interface traps. In addition to the ion implantation techniques studied here, MOS devices will also be exposed to electron beam and UV radiation to compare the effects on interface density.

Acknowledgements

Ion implantation performed on the Low Energy Implanter at Australian National University, Canberra.

References

[1] Dieter Schroder, Semiconductor Material and Device Characterization, New York: Wiley-Interscience, 1998

[2] M. Reed and J. Plummer, "Si-SO_2 interface trap production by low-temperature thermal processing" Appl. Phys. Lett. 51(7) 1987

[3] V. V. Afanas'ev, J. M. M. de Nils, and P. Balk "Necessity of Hydrogen for activation of implanted fluorine in Si-SO_2 structures" Appl. Phys. Lett. 63 (21) 1993

[4] S. Peterstrom, "Si-SO_2 interface trap density in boron- and phosphorous implanted silicon" Appl. Phys. Lett. 63 (5) 1993

Surface fraction statistics of gold nanoclusters of dissimilar sizes determined by RBS

Dinesh Kumar Venkatachalam [1], Dinesh Kumar Sood [1], Robert G Elliman [2] and Suresh Kumar Bhargava [1]

[1] *School of Applied Sciences, RMIT University, Melbourne 3001, Australia*

[2] *Electronic Materials Engineering Department, Research School of Physical Sciences and Engineering, Australian National University, Canberra, ACT 0200, Australia*

Abstract

Recently we reported [1] ordered spiral patterns of gold nanoclusters in silicon (100) substrates by Au ion implantation followed by thermal (furnace) annealing. This unique phenomenon was observed only above a critical threshold implantation dose and annealing temperature. High resolution SEM & TEM analysis showed two generations of Au nanoclusters of different size distributions. In this work, we have used Rutherford backscattering spectrometry (RBS) to study the surface fractional distribution of the Au nanoclusters of dissimilar sizes. Room temperature implantations of 10 keV Au^{2+} ions were performed into Si (100) single crystal substrates to a dose of $4.5x10^{16}$ Au/cm^{-2} followed by thermal (furnace) annealing at 600^{o} C for 60 min. The quantitative information about the lateral non-uniformity of the sample surface is estimated by analysing the shape of the RBS spectra. The values determined by RBS are in good agreement with electron microscopy results. This study shows the capability of RBS in obtaining quantitative information on size distribution of nanoclusters of heavy elements embedded in light substrates.

Introduction

Surface embedded metallic nanoparticles are of interest as templates for nanowire growth and as primary components for future nanoscale devices. Self-assembled nanoparticles, in particular, can facilitate selective bottom-up growth of patterned one-dimensional nanostructures. While major progress has been made in fabricating nanoparticles through various top-down approaches, a general direct bottom-up self-assembly method is still not available. In this context, ion implantation has emerged as a promising technique due to its ability to produce embedded nanoclusters [1-3]. Recently we reported the direct (maskless) formation of self-assembled spiral patterns of gold nanoclusters on Si by Au ion implantation and subsequent annealing [1]. A systematic study (SEM, AFM, XRD, and TEM) was conducted to determine the formation mechanism underpinning these patterns. High resolution electron micrographs showed the growth of Au nanoclusters of two different size distributions after annealing at temperature above the a-Si/Au eutectic melting point. In this work, we report the use of Rutherford backscattering spectrometry (RBS) to extract quantitative information about the size distribution of Au nanoclusters by analysing the shape of the backscattering spectrum as complement to the qualitative information obtained by microscopy.

RBS has emerged as a powerful analytical tool to investigate the distribution of heavy elements in light substrates. It has been applied to investigate the kinetics of phase formation, amorphous re-crystallization and for depth profiling of laterally uniform targets. Rough targets, on the other hand, are often considered as unsuitable for such analysis. Thirty years ago, Campisano et al. [4] drew the attention of scientific community to solve the ambiguity in RBS spectrum interpretation of laterally non-uniform targets. Following his work, in mid 90's, Marin et al. [5] developed an

algorithm to extract lateral non-uniformity statistics by analysing the shape of RBS spectra. In this report we present statistical information of surface fraction of different populations of Au nanoclusters segregated to substrate surface from a shallow near-surface a-Si/Au alloy produced by ion implantation and thermal annealing. The quantitative information obtained from RBS is confirmed by several low magnification scanning electron micrographs.

Experimental

Prime grade single crystal p-type (100) oriented, Czochralski silicon substrates were implanted at room temperature with Au^{2+} ions to an ion fluence of $4.5x10^{16}$ cm^{-2} using a MEVVA (metal vapour vacuum arc ion source). The lowest possible extraction voltage of 10 keV to produce a stable ion beam (with average energy of 20 keV) was chosen to ensure maximum surface concentration of implanted Au. A metal (Al) mask with 16 equi-spaced circular holes of 4 mm diameter was used in contact with the 2" diam substrate held at room temperature to produce identical and well separated zones of gold ion implanted regions. Later, these implanted regions were cleaved into samples for post-implantation treatments. The depth of the resulting amorphous layer was estimated using SRIM. After implantation, the samples were annealed in an open alumina tube (4" diam) furnace at 600 ^{0}C (temperature accuracy ±1%) for 60 min. High purity argon (Ar) gas was used as a carrier gas and the flow rate was maintained at 100 cm^3 /min throughout the course of heating/cooling. Before annealing, the furnace was ramped to the desired temperature in the presence of Ar ambient. The sample was then introduced and heated for the required time. In all the cases the sample was cooled rapidly by moving it to the cold end of the furnace tube after the anneal.

Rutherford backscattering with 2 MeV $^4He^+$ ions was used to evaluate the surface fractional distributions of Au nanoclusters of different populations. The detector was positioned at a scattering angle of 110^o (glancing angle to the sample surface) to obtain better depth resolution from the shallow amorphous region. The beam size was maintained large enough (1 mm^2) to contain a statistically representative sampling of the target to ensure a single spectrum is representative of the sample. The surface morphology and the size distribution of the nanoclusters were analysed using field emission scanning electron microscopy (FEI Qanta 200).

Results and discussion

Figure 1 shows the principle observation of our work, namely the formation of a bimodal distribution of Au nanocluster from a molten amorphous-silicon / gold (a-Si/Au) alloy layer after heating $4.5x10^{16}$ Au/cm^2 at 600^o C for 60 minutes. The as-implanted substrate shows a smooth topology (see inset in figure 1a) with a spatially random distribution of Au droplets in the size range 0.5 - 10 μm deposited during MEVVA implantation. These solid Au droplets (labelled by an arrow in the inset) are called "macroparticles" to emphasize their size compared to Au nanoclusters generated during the crystallization of a-Si/Au alloy layer during annealing. These "macroparticles" are generated at the vacuum arc cathode, travel along with the plasma and deposit on the target surface during MEVVA implantation [6].

Figure 1a shows the lateral non-uniformity of the sample surface caused by clustering of zone-refined Au on Si after heating at 600^o C for 60 min. It also shows that variations of the structure and composition are not so microscopic that no difference with the approximation of a homogeneous medium can be detected. The presence of

two generations of Au nanoclusters of different sizes is shown in figure 1b. The bigger clusters are of the size range 400-500 nm whereas the second generation clusters range between 50-75 nm. The size of the Au nanoclusters has been determined from several low magnification scanning electron micrographs. The increase in width of the size distribution is similar to 'Ostwald ripening' process where the bigger clusters grow at the expense of smaller ones at higher annealing temperatures.

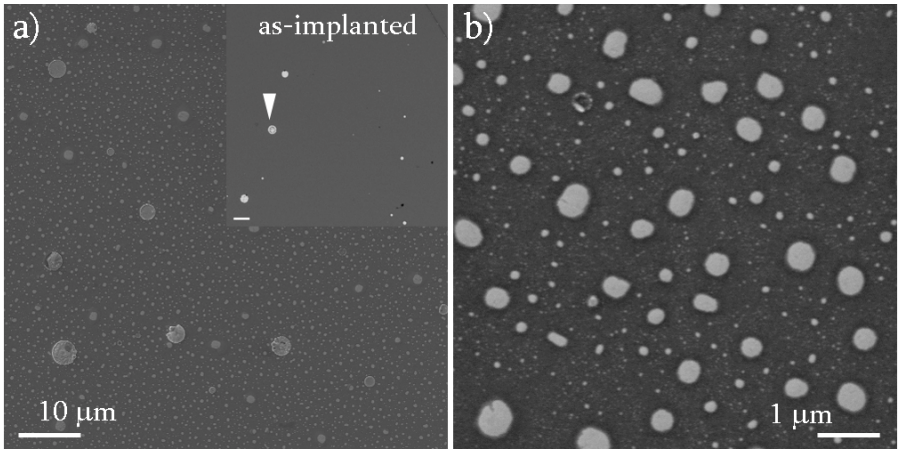

Figure 1: SEM micrographs showing surface morphology of $4.5x10^{16}$ Au/cm^2 implanted into Si (100) and annealed at 600^o C for 60 min a) low magnification image showing de-wetting of Au on Si (Inset showing as-implanted substrate); and b) high magnification image showing bimodal distribution of Au nanoclusters.

Figure 2 shows the corresponding backscattering spectra obtained with 2 MeV He^+ ions. The spectrum obtained from the as-implanted (un-annealed) sample shows a well defined Gaussian distribution of a 30 nm near-surface a-Si/Au alloy layer. The small tail of Au profile in the as-implanted sample is due to the random size and spatial distribution of the Au "macroparticles". After annealing at 600^o C for 60 min the implanted Au condensed into Au islands, leaving free a large potion of underlying silicon substrate. This is evidenced by a strong decrease in the Au yield and a gradual decrease in the intensity towards lower energies.

The Au profile after annealing at 600^o C in figure 2 confirms the presence of two generation of Au nanoclusters of different size distributions. The long Au tail is due to the lateral non-uniformity of the substrate surface and the size distribution of the larger Au nanoclusters. (Similar effects were observed by Campisano et al. [4] in a laterally non-uniform lead (Pb) thin film on Si.) In contrast, the smaller clusters lead to resolution limited surface peak [7].

By analysing the shape of the Au profile before and after annealing, it is estimated that after heating at 600^o C, Au nanoclusters of the size range 400-500 nm account for 70% of the Au coverage, whilst the smaller nanoclusters account for the remainder. To strengthen this estimation, the samples were annealed at temperatures above and below 600^o C for very short annealing cycles (5-30s) to study the early stages of Au nanocluster formation. The early stages of Au de-wetting and Au nanocluster formation is estimated by comparing the RBS spectra recorded after different annealing conditions (results will be reported elsewhere).

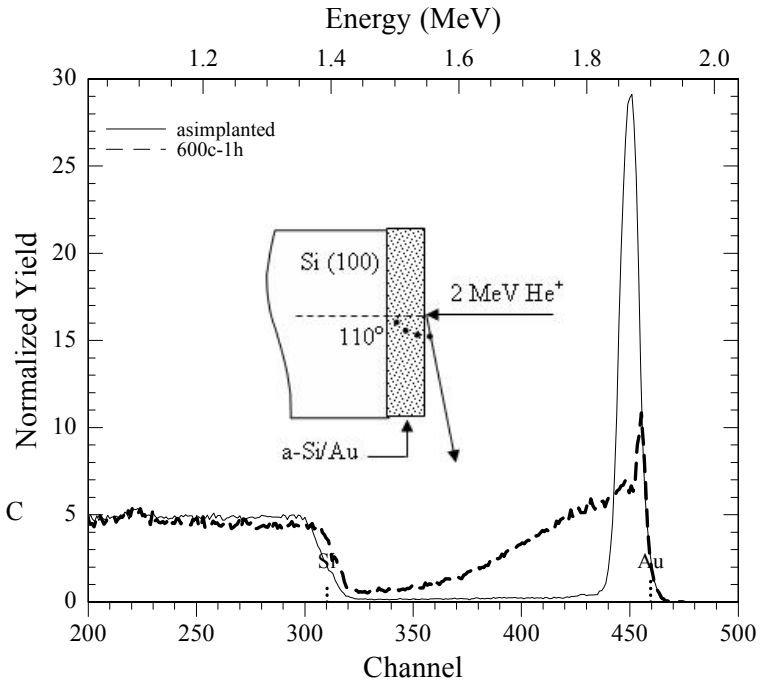

Figure 2: 2 MeV He^+ RBS spectra showing Si and Au profile of Si (100) implanted with $4.5x10^{16}$ Au/cm^2 before and after annealing at 600^o C: The solid line corresponds to as-implanted substrate; (--) dashed line corresponds to 600^o for 60 min

Conclusions

By analysing the shape of RBS spectra of Au implanted Si before and after annealing, the surface fraction of two different generations of Au nanoclusters is obtained. Good agreement with SEM measurements confirms the accuracy of this method. The above results show that RBS can provide quantitative information about laterally non-uniform samples with more descriptive information provided by SEM. It is sometimes possible to conclude the presence of lateral non-uniformity by comparing several RBS spectra.

Acknowledgements

We thank Dr. Peter J Evans and Mr. David Button, ANSTO for performing Au ion implantation. This research is supported by an AINSE grant.

References

[1] Dinesh Kumar Venkatachalam, Dinesh Kumar Sood and Suresh Kumar Bhargava, Nanotechnology (submitted).

[2] Dinesh Kumar Sood, Praveen Kumar Sekhar and Shekhar Bhansali, Applied Physics Letters 88 (14), 143110 (2006).

[3] Th Stelzner, G.Andra, E Wendler, W Wesch, R Scholz, U Gosele, and S Christiansen, Nanotechnology 17, 2895 (2006).

[4] S.U.Campisano, G.Foti, F.Grasso and E.Rimini, Thin Solid Films 25, 431 (1975).

[5] N.Marin, Y.Serruys and P.Calmon, Nuclear Instruments and Methods in Physics Research - B 108, 179 (1996).

[6] Othon R. Monteiro and Andre Anders, IEEE Trans. on Plasma Science 27 (4), 1030 (1999).

[7] Wei-Kan Chu, James W.Mayer and Marc-A.Nicolet, *Bacscattering Spectrometry*, 1 ed. (Academic Press Inc., New York, 1978).

Photonic nanostructures and their influence on Er luminescence

R.G. Elliman, A.R. Wilkinson, T.-H. Kim and P. K. Sekhar
Electronic Materials Engineering Department, Research School of Physical Sciences and Engineering, Australian National University, Canberra, ACT 0200, Australia.

Abstract

The properties of Er-doped silica wires are investigated and shown to exhibit properties characteristic of the material nanostructure. Specifically, the 1.5 μm emission from Er^{3+} is shown to exhibit a longer luminescence lifetime and enhanced thermal quenching in comparison to similarly doped bulk silica samples. The former is attributed to a reduction in the optical density of states of the nanowire samples and the latter to their large surface-to-volume fraction.

Introduction

Whilst there has been intense interest in the synthesis, structure and properties of silica nanowires [1-5], little work has been performed on optical doping and functionalisation of such materials. Several studies have noted the strong intrinsic luminescence from as-grown nanowires and a recent study by Zhang et al. [5] reported results for Er implanted nanofibre bundles. However, this latter study only examined samples implanted to very high fluences where strong concentration quenching effects are expected. In the present study, we report new results for Er-doped silica nanowires, including the impact of the nanowire structure on the Er luminescence and a novel ion-implantation technique that enables simultaneous nanowire growth and doping.

Experimental

Silicon wafers of (100) orientation were coated with a 20 nm thick Pd layer by sputter deposition. Portions of the wafer were subsequently annealed at 1100°C for 4 hours in an Ar ambient to produce a dense, randomly-oriented array of silica nanowires on the sample surface. Doping of the nanowires was achieved by ion-implantation with 110 keV ErO^-. Samples were implanted to fluences in the range from 5×10^{14} to 1×10^{16} Er/cm^2 together with fused silica samples for comparison. The implanted Er has a mean-projected range in SiO_2 of 45 nm and its peak concentration ranges from 0.3 at. % to 5 at. %. All samples were then annealed at 900°C for 1 hour in either N_2 or O_2 to optically activate the erbium. These experimental procedures are summarized in Fig. 1.

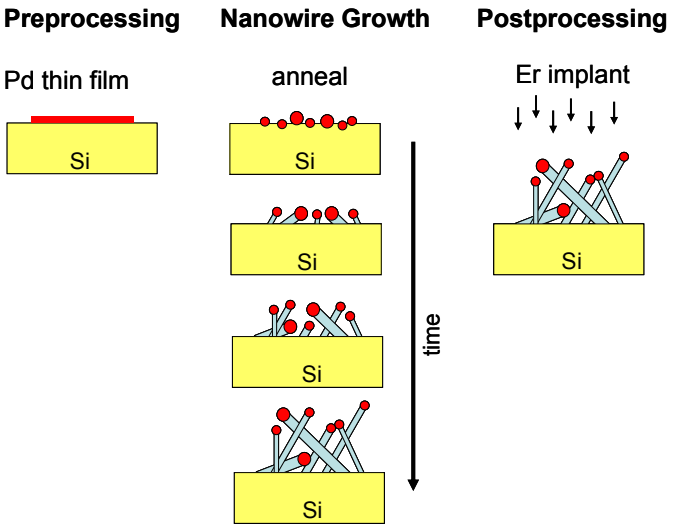

Fig. 1: Schematic of experimental procedures employed in this study.

Physical characterisation of nanowires was undertaken by scanning electron microscopy using a Hitachi field-emission scanning electron microscope (FE-SEM) equipped with energy-dispersive x-ray (EDX) analysis. Photoluminescence (PL) measurements of the Er emission were performed at room temperature using the 488 nm line of an argon ion laser as the excitation source. The luminescence emission was analysed with a Triax 320 spectrometer equipped with a high-sensitivity liquid-nitrogen cooled germanium detector. The excitation laser was mechanically chopped at 15 Hz and standard lock-in techniques employed to collect the spectra. For time-resolved PL measurements, the output of the detector was connected directly to a digital storage oscilloscope and the response averaged over 128 cycles. The time response of the system is estimated to be less than 0.5 ms.

Results and Discussion

Fig. 2 shows SEM images of silica nanowires produced by the metal-induced growth process described above. The nanowires have an average diameter of around 150 nm and lengths exceeding 100 µm. The nanowire growth mechanism has been investigated and found to depend on the formation of volatile Sao via a reaction between trace oxygen in the annealing ambient (present at the ppm level) and the silicon wafer.

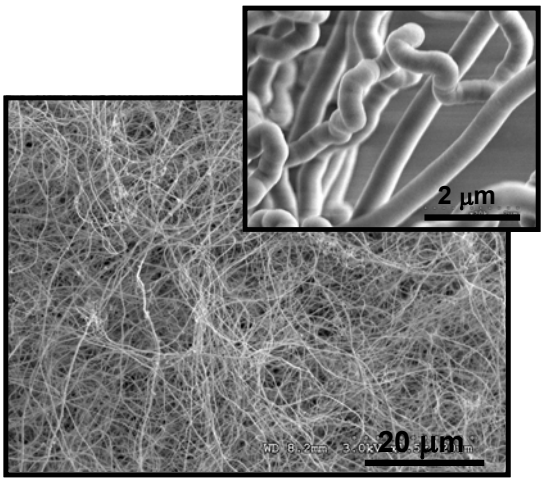

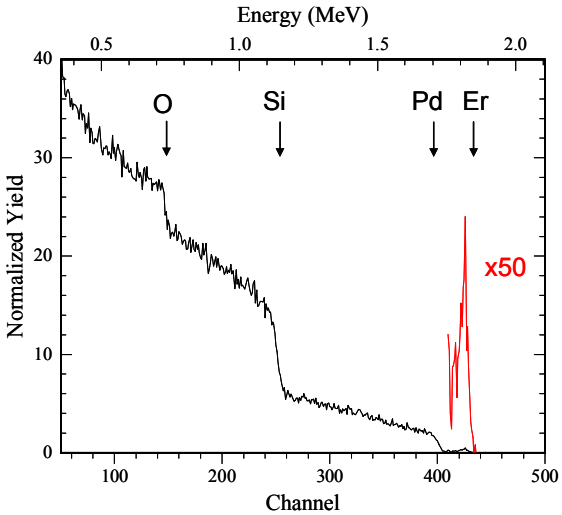

Fig. 2: SEM images of Pd-induced nanowires produced by annealing at 1100°C in Ar.

Fig. 3: RBS spectrum of nanowire sample after implantation with 100 keV ErO^- to a fluence of $5x10^{14}cm^{-2}$.

Fig. 3 shows an RBS spectrum of the nanowire sample after implantation with ErO^- to a fluence of $5x10^{14}$ cm^{-2}. The spectrum shows that Pd is distributed throughout the nanowire layer, consistent with its role as a growth catalyst. The implanted Er is located in the near-surface region of the nanowires, as expected from the fact that the projected range, (~45nm), is less than the average nanowire diameter (~150nm). Analysis also suggests that the nanowires consist of silicon-rich-oxide rather than stoichiometric SiO_2.

Fig. 4 shows a typical PL spectrum from the Er implanted nanowires together with a schematic of the optical transitions involved. The 1.5μm emission corresponds to the $^4I_{13/2}$ -> $^4I_{15/2}$ transition of the Er^{3+} ion.

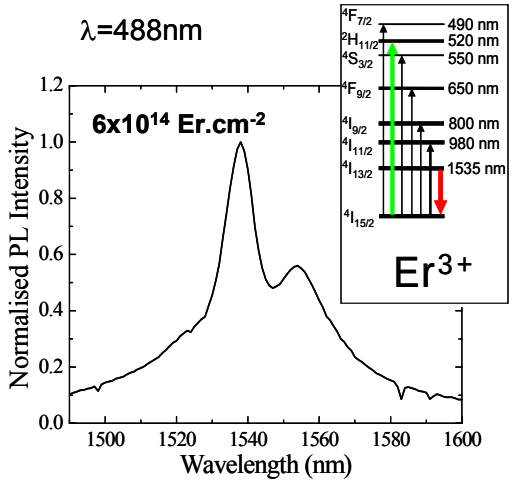

Fig. 4: Room temperature PL spectrum from a nanowire sample implanted with ErO^- to a fluence of $6x10^{14}cm^{-2}$.

Fig. 5 shows measured PL decay curves for nanowire samples implanted to a fluence of $6x10^{14}cm^{-2}$ after annealing in N_2 and O_2, together with a similarly implanted bulk silica sample annealed in N_2. The luminescence lifetime of Er in the nanowire sample is longer than that of the bulk sample. Analysis suggests that this is a direct result of a reduced optical density of states in the nanowire samples.

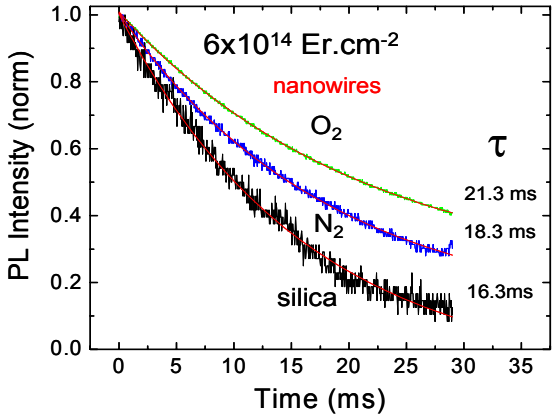

Fig. 5: PL decay curves for nanowire samples implanted with ErO^- to a fluence of $6x10^{14}cm^{-2}$ and annealed in N_2 and O_2. Results for a similarly implanted bulk silica samples are included for reference.

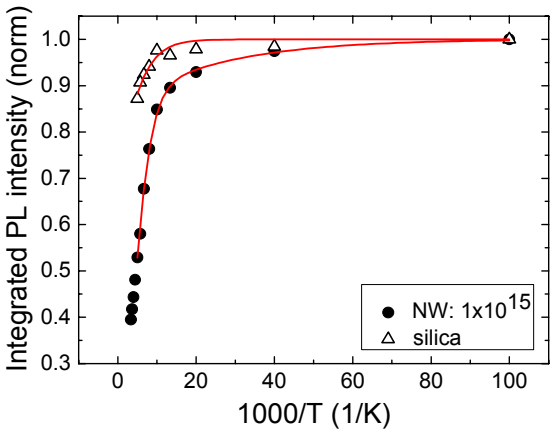

Fig. 6: Integrated PL intensity as a function of temperature for nanowire and bulk silica samples implanted with ErO^- to a fluence of $1x10^{15}cm^{-2}$ and annealed in N_2.

Fig. 6 shows the temperature dependence of the PL intensity for nanowire and bulk-silica samples. This shows enhanced thermal quenching of the luminescence in nanowire samples compared to bulk silica samples. This effect is attributed to interaction between the excited state of Er and surface defects, with the effect enhance in nanowires due to their high surface-to-volume fraction.

Summary and Conclusions

The properties of Er-doped silica wires have been examined and shown to exhibit properties characteristic of the material nanostructure. Specifically, the 1.5 μm emission from Er^{3+} was shown to exhibit a longer luminescence lifetime and enhanced thermal quenching in comparison to similarly doped bulk silica samples. The former is attributed to a reduction in the optical density of states of the nanowire samples and the latter to their large surface-to-volume fraction.

Acknowledgements

The authors would like to thank Mr David Llewellyn and Dr. Kidane Belay for assistance with electron microscopy. The Australian Research Council is also acknowledged for partial financial support of this project under its Discovery Grant Programme.

References

[1] D. P. Yu, Q. L. Hang, Y. Ding, H. Z. Zhang, Z. G. Bai, J. J. Wang, Y. H. Zou, W. Qian, G. C. Xiong and S. Q. Feng, Appl. Phys. Lett., 73 (1998) 3076

[2] Z. L. Wang, R. P. P. Gao, J. L. Gole and J. D. Stout, Advanced Materials, 12 (2000) 1938

[3] D. K. Sood, P. K. Sekhar and S. Bhansali, Appl. Phys. Lett., 88 (2006) 3

[4] P. K. Sekhar, S. N. Samhandam, D. K. Sood and S. Bhansali, Nanotechnology, 17 (2006) 4606

[5] X. T. Zhang, Z. Liu, C. Wong, S. Hark, N. Ke and S. Wong, J. Phys. Chem., C111 (2007) 4083

Unravelling the mystery of zinc oxide

John V Kennedy and Andreas Markwitz
National Isotope Centre, GNS Science, 30 Gracefield Road, PO Box 31312, Lower Hutt, New Zealand, Email: j.kennedy@gns.cri.nz

Zinc oxide (ZnO) is a low-priced, powdery white substance that is harmless to humans. It has found use in a wide range of medical and cosmetic applications. The ability to absorb ultraviolet light makes zinc oxide an active ingredient of choice in suntan lotions. ZnO is also incorporated in dietary supplements and vitamin tablets as source of the essential micro-nutrient zinc for the human body. It is widely used in paint pigments, paper coatings, UV-absorbing pigments, voltage spike suppressing varistors, touch-screen transparent conductive films, gas sensors and filler for rubber goods, etc. Although ZnO is used in commonplace, it also possesses semiconductor-like properties. It has a direct band gap of 3.36eV at room temperature and a higher excitation binding energy (50meV) which assures more efficient emission at higher temperatures, compared with other wide band gap materials such as GaN (28meV). Owing to these properties, ZnO has been identified by researchers in world wide as a next generation material that has the potential to create more efficient optoelectronic devices such as LED's, Lasers, CDs and high definition DVD players [1-2].

ZnO is a natural n-type semiconductor, because of the presence of intrinsic defects such as Zn interstitials and O vacancies causing deviation from stoichiometry. Progress in ZnO research for optoelectronic applications remains limited due to constraints encountered in producing p-type materials in either thin films or bulk crystals. The growth of n-type material has proven to be relatively simple, as shallow donor impurities (Al, Ga and In) are readily incorporated into the ZnO lattice [1,3].The fundamental difficulty in p-type doping of ZnO arises from a number of reasons. For example, the donor level may be especially deep so that thermal excitation into the valence band is low. Other reasons could be a low solubility of the dopant or induced self compensating processes [4]. Recent theoretical studies have suggested that zinc vacancies in the ZnO matrix act as possible deep acceptors. However, nitrogen (among group V elements of P, As, N) atoms substituting for oxygen in the ZnO film have shown to be the most promising shallow acceptor in ZnO [4]. The aim of this investigation is to establish the doping protocol for nitrogen ion implantation into ZnO thin films using the GNS low energy ion implantation facility and ion beam analysis techniques.

Experimental procedure and results

We have deposited a range of ZnO thin films on silicon (100), quartz, glass and glassy carbon substrates using radio frequency (RF) magnetron sputtering under the optimised deposition parameters described in ref.3. The ion beam analysis techniques of RBS, Elastic Recoil Detection Analysis (ERDA) and Nuclear Reaction Analysis (NRA) [5,6] were used to measure the stoichiometry of the films and impurities such as hydrogen concentrations. Large variations in film thickness and composition were found in most of the as deposited films. It was also found that less than 1-2% hydrogen was present on the films deposited on Si. XRD analysis revealed that a strong (002) preferential orientation in the ZnO films deposited Si irrespective of thickness, indicating a polycrystalline hexagonal structure characteristic of ZnO, and preferential orientation along c-axis. It is due to the lowest surface free energy of (002) plane in ZnO.

Ion implantation for doping semiconductor materials (i.e. introducing dopants into the semiconductor) is a well established technique for the fabrication of electronic and optoelectronic devices. We have implanted 23keV nitrogen ions at under normal incidence with fluences ranging from $1x10^{15}$ to $1x10^{17}$ ions cm^{-2} into ZnO films deposited on Si. The ion beam was raster scanned over the surface to produce a laterally homogeneous implantation into the films. DYNAMIC-TRIM [7] calculations have been performed to determine theoretical implanted ion profiles for the various fluences. The calculations predict a mean projected range of 45nm coupled with a maximum implantation depth of around 80nm. For these fluences, the N peak concentration varies between 0.05 and 18 at.%. At fluences larger than 1×10^{16} N cm^{-2}, the N profile intersects with the surface. Annealing was performed using an electron beam annealing system [8] at sample temperatures of 700°C for 10 min. This system operates with an electron energy of 20 keV and current up to 2mA. The annealing chamber is evacuated with a turbomolecular pump to a base pressure better than 1×10^{-7}mbar.

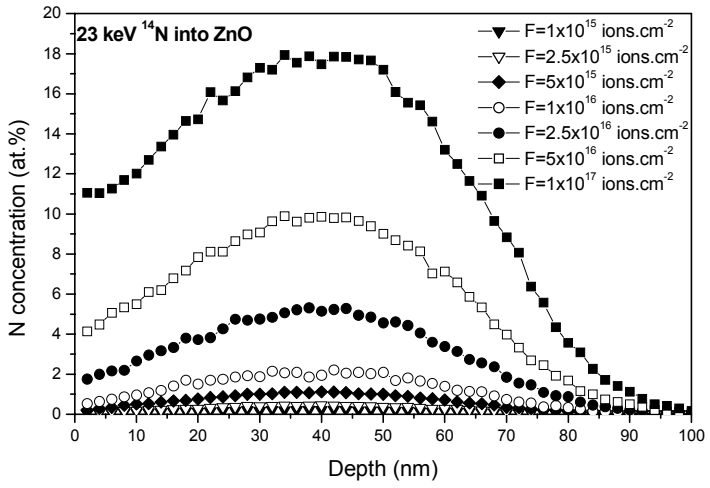

Figure 1. N depth profiles calculated with DYNAMIC-TRIM for N implanted at 23keV into ZnO with fluences from $1x10^{15}$ to $1x10^{17}cm^{-2}$

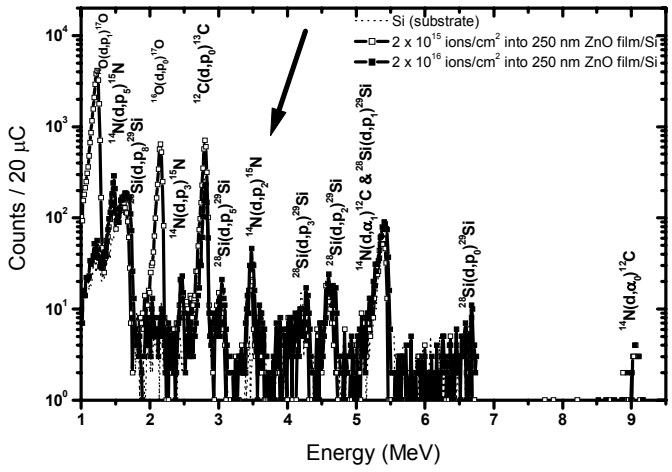

Figure 2. NRA spectra of nitrogen implanted ZnO films on Si for two different fluences.

NRA measurements were carried out to determine the nitrogen concentration in the implanted samples. Nuclear reactions induced by bombardment with energetic protons, deuterons or alpha particles cause the emission of other energetic particles that can be used for elemental analysis. The sensitivity of the technique is very high for light elements [6].

Deuteron beams of an energy of 920keV (ion current = 20nA, ion beam diameter = 1 mm) were used. The emitted particles were detected with a surface barrier detector (active area of $300mm^2$, Mylar absorber thickness 10.6μm) mounted at 150° to the beam. Standard materials of anodically oxidised Ta_2O_5 and TiN were used for calibration purposes.

Fig. 2 shows independent nuclear reaction peaks for the implanted ion N along with the O from the film and Si from the substrates. Carbon impurities can also be seen.

The peak width corresponds to the thickness of the film. The peak height can be converted into concentration by taking into account the values of cross sections and stopping power. In the present study the nuclear reactions $^{14}N(d,\alpha_0)^{12}C$ ($d\sigma/d\Omega$ = 0.07mb sr^{-1}) and $^{14}N(d,p_2)^{15}N$ ($d\sigma/d\Omega$ = 0.56 mb sr^{-1}) were used to determine the N ion concentration in the implanted films. These reactions were chosen because their peaks do not interfere with peaks from the film and substrate material. It was found that the measured N concentrations at a fluence of $2x10^{16}$ ions cm^{-2} are around 4.1 at.% which is close to the DYNAMIC-TRIM calculated values as shown in Fig. 1. Nitrogen concentration can be measured at fluences above $5 \pm 1 \times 10^{15}$ ions cm^{-2}, which convincingly proves that NRA is suitable for detecting low levels of nitrogen in implanted semiconducting materials.

Electrical and optical measurements

The resistivity, carrier concentration and carrier mobility of the deposited and nitrogen implanted ZnO films on silicon were measured using an Ecopia HMS-3000 Hall Effect measurement system [9]. A high purity Ti coating was used for ohmic contact to all the films. Table l summarises the electrical characteristics obtained from the implanted and annealed films.

Table.1. Electrical properties of nitrogen implanted ZnO film deposited on Si substrates

Sample code	Film thickness (nm)	Sample treatment	Carrier Concentration (cm^{-3})	Mobility ($cm2.V^{-1}.s^{-1}$)	Resistivity (Ω cm)	Type
50	302	as-deposited	-4E19	4	0.04	n
51	170	Implanted (F=$1x10^{15}$ cm^{-2})	-4.9E18	1.5	0.04	n
52	200	(F=$1x10^{15}$ cm^{-2}) & annealed	2.6E18	3	1.0	p
53	314	Implanted (F=$2x10^{15}$ cm^{-2})	-2.2E19	9	0.032	n
54	302	(F=$2x10^{15}$ cm^{-2}) & annealed	3.39E18	305	0.0047	p
55	326	Implanted (F=$2.5x10^{16}$ cm^{-2})	-2.1E19	3	0.01	n
56	338	(F=$2.5x10^{16}$ cm^{-2}) & annealed	3.4E18	278	0.006	p
57	302	Implanted (F=$5x10^{16}$ cm^{-2})	-1.9E19	3	0.12	n
58	326	(F=$5x10^{16}$ cm^{-2}) &annealed	2.34E18	40	0.06	p

It is found that the N implanted and annealed targets showed p –type carrier concentration values from -1.0 $x10^{13}$ –5.0 $x10^{19}cm^{-3}$, hole mobility from 1 – $500cm^2.vs^{-1}$ and resistivity of 0.0001 – 5 ohm.cm [10] . All the implanted samples show n-type conductivity. After annealing, the films were showing p-type behaviour. The carrier concentration decreases after implantation since the implanted region becomes amorphous. However, the carrier mobility does not change. Once the implanted films are annealed, the carrier mobility has increased two orders of magnitude and the carrier concentration value remain in the same order of magnitude value.

The optical properties have been investigated by photoluminescence (PL) [10]. PL measurements are performed at 77K. The results are shown in Figure 3. A strong donor bound exciton peak near 374nm (~3.32eV), which is typical for n doped ZnO, is observed in addition to the broad peak in the visible region near 600nm. The exciton peaks correspond to p-type ZnO formed as a result of the acceptor doping process of low-energy acceptor ion implantation and EB annealing are observed between 360 – 450nm. The most prominent line at 3.31eV is observed in our p-type

ZnO samples. In addition to that few other acceptor bound exciton peaks at 3.31 and 3.35eV are also observed.

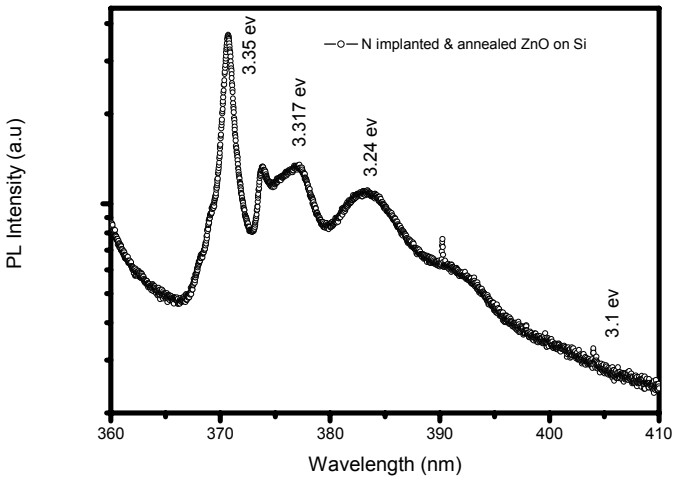

Figure 3. PL spectra nitrogen implanted ZnO film deposited on Si

Summary

We have successfully developed a protocol to produce a p-type ZnO via low energy ion implantation and electron beam annealing. We have implanted low energy nitrogen ions into thin films deposited on Si (100). The implantation depth was calculated to be 50nm using Dynamic-TRIM. The implanted N was measured quantitatively using nuclear reaction analysis. The structural, electrical and optical properties were determined by XRD, Hall effect and PL. It is found that the N implanted and annealed targets show p–type carrier concentration. PL revealed exciton peaks in the region between 300 -450 nm. These exciton peaks correspond to p-type ZnO formed as a result of the acceptor doping process of low-energy acceptor ion implantation and EB annealing.

Acknowledgments

The authors would like to thank Prof. Wei Gao and Dr. Z. Li for their contributions. This project is supported by a Marsden Grant from the Royal society of New Zealand and Foundation for Research Science and Technology of New Zealand.

Reference

1. D.C. Look, J.W. Hemsky and J.R. Sizelove, Phys. Rev. Let, 82 (1999) 2552.
2. C. Jagadish and S.J. Pearton, “Zinc oxide bulk, thin films and nanostructures”, Elsevier (2006)
3. W. Gao and Z. Li: Ceramics International. 30 (2004)1155.
4. Y. Yan, S.B. Zhang, S.T. Pantelides, Phys.Rev.Lett 86 (2001) 5723.
5. J. Kennedy, A. Markwitz, Z. Li and W. Gao, International Journal of Modern Physics B, Vol. 20, (2006) 4655.
6. J. Kennedy, A. Markwitz, B.J. Ruck, S.M. Durbin and W. Gao, Journal of Electronic Materials V 36 N 4 (2007) 472-482.
7. J. P. Biersack, Nucl.instru. and Meth B 27 (1987) 21.
8. A. Markwitz., R. W. Michelmann, H. Baumann, E. F. Krimmel, E. C. Paloura, A. Knop and K. Bethge, J. Appl. Phys A54 (1994) 435.
9. J. Kennedy, A. Markwitz, Z. Li, W. Gao, S.M. Durbin and R. Reeves, Current applied physics 6 (2006) 495.
10. John V Kennedy and Andreas Markwitz, “Zinc oxide materials & methods for their preparation”, PCT International application claiming priority from NZ 542917, filed 05 April 2007.

Towards a formula for optimized production of single NV centres in diamond by ion implantation

J.O. Orwa [1], A. Cimmino [1], B. Gibson [2], D. Simpson [2] and S. Prawer [1,2,3]

1 Microanalytical Research Centre, School of Physics, University of Melbourne, Victoria 3010, Australia

2 Quantum Communications Victoria (QCV), University of Melbourne, Victoria 3010, Australia

3 Centre for Quantum Computer Technology, Melbourne node, Australia

Corresponding author. Tel.: +613 8344 7651; fax: +613 9347 4783; e-mail: jorwa@physics.unimelb.edu.au

Abstract

Single NV centres in diamond have been the subject of many studies in recent years due to their potential applications in quantum information processing. Compared to other single photon sources such as attenuated lasers, single atoms, molecules and semiconductor quantum dots, the NV diamond colour centre has the advantage of simplicity, photo-stability and room temperature operation. Despite these excellent properties, a recipe for maximizing the efficiency of NV production is yet to be optimized. This study is a step towards this optimization and uses photoluminescence and confocal fluorescence spectroscopy to investigate the NV yield of high purity single crystal type IIa diamond samples implanted with nitrogen followed by thermal annealing. The parameters varied include implanted nitrogen species, implantation energy, temperature, fluence and annealing temperature. Further, the study distinguishes between the yields of NV- and NVo and offers theoretical basis for the observed differences.

Keywords: Diamond, N-V centre, Ion Implantation, Single photon source.

Neutral atom microscopy: a non-destructive, high-resolution surface analysis technique

K. O'Donnell [1], P.C. Dastoor [1], D.J. O'Connor [1], W. Allison [2]

[1] School of Mathematical and Physical Sciences, University of Newcastle, NSW 230

[2] Cavendish Laboratory, Cambridge University

In recent years there has been much interest in neutral atom microscopy for surface studies. A neutral helium beam with an energy of 30-110 meV has a sub-angstrom de Broglie wavelength, making it an extremely sensitive surface probe. In addition, the energy range allows for simultaneous thermal and chemical contrast.

Development of a microscope based on neutral helium atom beams has previously been held back by the lack of sufficiently advanced optical elements for focussing and detection, however it is believed that there are now viable approaches to both problems. Ultra-thin single-crystal, hydrogen-passivated Si(111) surfaces have been created at the Cavendish Laboratory, which when electrostatically bent can be used to focus a helium beam for microscopy.

For an imaging microscope configuration, the University of Newcastle is developing a spatially-resolved field ionization detector allowing for the first time true imaging with a neutral atom beam source. In this talk the author will describe the concepts and technology behind both the Cavendish Laboratory's Scanning Helium Microscope (SHeM) and the University of Newcastle's spatially resolved helium field ionization detector.

Characterization of silicon detectors utilized in an on-line dosimetry system for microbeam radiation therapy

A.M. Baloglow [1], M.L.F. Lerch [1], M. Reinhard [2], R. Siegele [2], E. Brauer-Krisch [3], E. Siegbahn [3], V. Perevertailo [4], A. Bravin [3], A.B. Rosenfeld [1]

[1] *Centre for Medical Radiation Physics (CMPR), University of Wollongong, NSW, Australia*
[2] *Australian Nuclear Science and Technology Organization (ANSTO), Lucas Heights, NSW, Australia*
[3] *European Synchrotron Radiation Facility (ESRF), Grenoble, France*
4. SPO-BIT, Ukraine

Microbeam radiation therapy (MRT) is a new form of radiation treatment being developed for children with inoperable and otherwise untreatable brain tumours. A new on-line dosimetry system is currently under development at the Centre for Medical Radiation Physics, University of Wollongong, Australia [1], which will be used to measure peak dose for each microbeam and the instantaneous MRT peak-to-valley dose ratio (PVDR). The peak dose and PVDR is an important physical parameter in MRT that indicates the quality of the MRT beam and must be measured with an accuracy of better than 5%.

The detector will also be used to act as a fast beam-stop trigger to avoid an undesirable dose being delivered to the patient undergoing MRT treatment within milliseconds time treatment delivery. Therefore the radiation damage induced in these detectors is important for understanding the reliability of the deduced dose using these detectors and will determine the useable lifetime of the detectors. The work outlined in this article discusses radiation damage studies induced in the bulk silicon strip detector utilized in the dosimetry system. Such radiation damage studies have not been widely studied under the very intense pulsed, low energy (average energy 100keV) synchrotron X-ray photons.

Materials and methods

The strip detector was fabricated by 'SPO-BIT' Ltd., Ukraine, according to the CMRP design. The detector is made up of 128 p+ p-n junction strips each with a width of 10 microns, length of 500 microns and with a strip-pitch of 200 microns produced on a 375 micron n-silicon substrate of resistivity of 5 kOhm cm. Current-voltage I-V measurements were taken of individual strips of the detector using a Keithley237 current source device. A BOONTON7200 capacitance bridge was used to measure the capacitance-voltage, C-V, characteristics of the silicon strip detector as above. The device was placed under evacuated conditions and measured at room temperature.

The Ion Beam Charge Collection (IBIC) study was performed on the ANTARES tandem accelerator at the Australian Nuclear Science and Technology Organization (ANSTO), using a 5.5MeV alpha particle beam with a diameter of 2 microns under reverse and zero bias. All three of the above mentioned techniques were performed before and after the irradiation of the detector with 60kGy from biomedical beamline (ID17) at the European Synchrotron Radiation Facility (ESRF) in Grenoble, France. The detector was irradiated under standard MRT beam conditions [2].

Results and Discussion

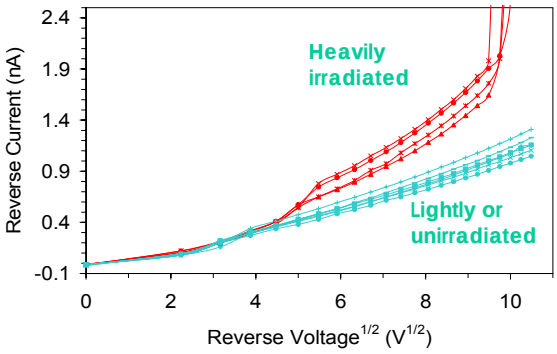

Figure 1. Current-voltage characteristics of the post-irradiated Silicon Strip Detector.

Fig. 1 displays the I($V^{1/2}$) characteristics of some of the strips that make up the silicon strip detector, after MRT synchrotron beam irradiation. The neighbouring strips were suspended. Due to the penumbra of the 1mm microbeam the strips in the centre of the beam received higher radiation dose. One can clearly identify the heavily irradiated strips compared to the lightly/unirradiated strips. The non-irradiated and lightly irradiated p+ strips have demonstrated a typical linear relationship I vs $V^{1/2}$ in a wide range of the reverse bias. However, the relation no longer exists for heavily irradiated strips for bias above 20V

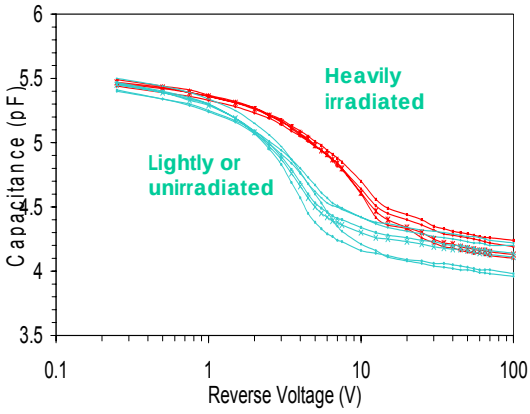

Figure 2. Capacitance-voltage characteristics of the post-irradiated Silicon Strip Detector.

Fig. 2. shows a distinct difference in the CV curve between the heavily irradiated strips to the lightly irradiated or unirradiated strips. One important notable feature is the change occurring to the kink within the C-V curve within (1-15)V.

Both of the effects mentioned above can be explained by build up positive charge in the field oxide by synchrotron ionizing radiation. The mechanism of increasing current is related to the creation of a MOS structure by the Al contact above the field oxide outside of the p-n junction area of the p+ strip. The build up of positive charge within this field oxide layer results in an electron enhancement channel at the silicon surface, leading to lateral shrinkage of the depletion layer at the p+ strip/n layer. An increase of the negative bias above the critical voltage (~20V) will overcome this induced electron channel and result in abrupt lateral depletion. Increasing of the depleted volume of the p-n junction increases the reverse current proportionally.

A similar explanation can be related to the kink present within the C-V characteristics of irradiated p+ strips. The MOS capacitance, produced by the Al contact above the field oxide and outside of the p-n junction, is connected in parallel to the capacitance of the reverse biased p-n junction. The effect of this MOS

capacitance on the total capacitance can be seen on Fig.2. With the positive charge accumulated in the field oxide layer, this MOS component requires a greater reverse bias to reduce the term and for the capacitance exhibited by the depleted p-n junction to dominate. This can be seen in the C-V curve for the heavily irradiated strips. A more detailed explanation with theoretical modelling of this structure will be presented in the full paper.

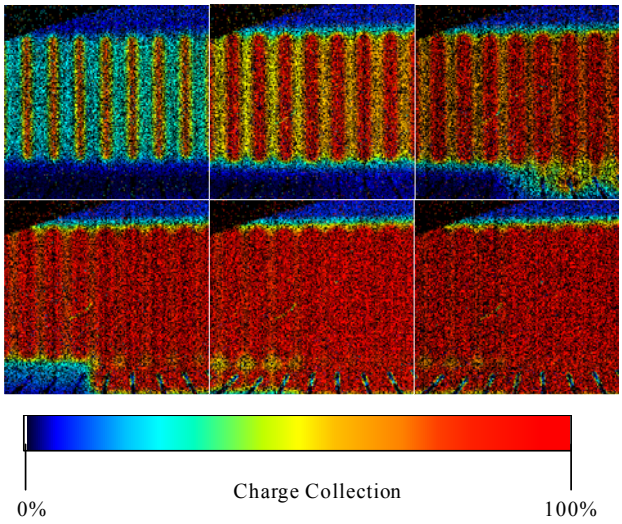

Figure.3 Image of the collected charge on IBIC experiment.

For verification of the nature of the radiation damage within the strip detector under the synchrotron radiation and the explanation of the behaviours of I-V and C-V characteristics presented above, an Ion Beam Charge Collection (IBIC) study has been carried out on the device. IBIC was performed on the ANTARES tandem accelerator at the Australian Nuclear Science and Technology Organization (ANSTO), using a 5.5MeV alpha particle beam with a diameter of 2 microns under zero and reverse bias. Fig.3 shows a colour coded representation of the collected charge on 7 consecutive p+ strips irradiated with the 1mm synchrotron beam under various reverse bias conditions (0, 5, 10, 20, 30, 50V). The Al connection pads containing the wire bonding to the detector board can be clearly seen at the bottom of each strip.

It is clear that for bias 0 and 5 V full charge collection was observed in a central part of the 10 μm strip and no charge collection was observed under Al pads due to build up charge in the field oxide as discussed above. With increasing bias up to 10V (upper right image) improvement of the charge collection

has been observed for the three far right strips which have received less dose due to beam penumbra and therefore less build up charge in the field oxide. The next image (lower row, left image) a bias of 20V demonstrates the effect of the accumulated positive charge within the field oxide layer, due to the irradiation of intense x-rays, on the charge collection efficiency of the device. A further increase in bias leads to full

charge collection under the Al pads of the strips on the left hand side and laterally to P+ strips due to spreading of the depletion region.

Conclusion.

The proposed model of radiation damage of the n-Si strip detector for MRT dosimetry on ESRF synchrotron beam based on build up charge in a field oxide only has been proved. This model was successfully applied for explanation of peculiarities of I-V and C-V characteristics changes. No bulk defect due to the irradiation of intense x-rays was observed in this application. Build up charge effect can be avoided by overbias of the strips or by regular annealing under 150°C if detector is to be used in a passive mode [3].

References

[1] M. Lerch et al "Design of an On-Line Dosimetry System for Microbeam Radiation Therapy" IEEE 2007, Hawaii

[2] E. Brauer-Krisch et al. "New Irradiation Geometry for Microbeam Radiation Therapy" Phys. Med. Biol. 50 3103-3111, 2005

[3] A. Kelleher, N. McDonnell, N.B. Oapos, W. Lane, L. Adams. "Investigation into the Re-Use of PMOS Dosimeters" IEEE Trans. on Nucl. Sci., 41,445 – 451, 1994

Diffusion characteristics of silicon implanted with group IV elements

Perry Davy, Andreas Markwitz, Horst Baumann,
GNS Science, National Isotope Centre, Lower Hutt, New Zealand

Low-energy ion implantation of Group IV elements into wafer silicon has been used to investigate the fabrication of novel nanomaterials. For example 7 keV Pb^+ atoms have been implanted into p-type Si wafer material at room temperature with the ion fluence of 4 x 10^{15} at cm^{-2} [1]. The analysis of the physical properties of implanted materials includes determination of the elemental depth distribution by RBS, elemental loss under high vacuum conditions after computer controlled electron beam annealing at 200 to 1000 ºC; and the determination of surface topography by AFM [2]. The results of the experimentally determined elemental loss and structural properties need to be compared to theoretical calculations in order to understand and explain the physical structure of implanted substrates. This paper presents theoretical calculations for the rate of Pb and Sn loss from Si implanted substrates under vacuum during electron beam annealing over a range of temperature regimes.

Electron beam annealing of Si wafer material itself can produce nanostructures called nanowhiskers with potential applications as field emission devices [3]. The process of implanting ions into Si substrates results in amorphisation of the Si crystal lattice at the implanted area. Electron beam annealing of the implanted area recrystallises the Si or co-recrystallises Si with the implanted atoms to produce materials with novel and interesting nanostructures [4-5].

An important part of the process is determining the atomic concentration and depth profile of the implanted material. The annealing of substrates can result in diffusion of implanted atoms into, and out of, the bulk material. Theoretical calculations of the rate of loss of implanted atoms can be compared to experimentally determined values.

In the absence of any other interaction with the substrate, kinetic theory can be used to determine the rate of atomic loss from a substrate surface. The rate of migration of a property (mass, energy) is measured by its flux (J) and for mass this is expressed in kg m^{-2} s^{-1}. The general form of the equation known as Fick's First law of diffusion is given as [6]:

$$J = -D(\mathrm{d}N/\mathrm{d}z) \qquad (1.1)$$

where:
D = the diffusion coefficient
N = the number of particles per unit volume (atoms cm^{-3})
z = some axis

With respect to the case of atoms leaving a solid surface under high vacuum conditions we assume that the flux is mono-directional and equation 1.1 can be used to derive the flux of atoms from the surface such that:

$$J = \tfrac{1}{4} N \cap^2 \qquad (1.2)$$

$\cap$ = mean speed = $(8kT/\pi m)^{0.5} = (8RT/\pi M_{mol})^{0.5}$ from the Maxwell distribution.

Since we are interested in the change of state from solid to gas we can incorporate the vapour pressure and atomic mass and rearrange equation 1.2 to give:

$$J_m = 4.38 \times 10^{-4} \times p \times (M_{mol}/T)^{0.5} \qquad (1.3)$$

where:

J_m = mass flux (g cm^{-2} s^{-1})
p = vapour pressure (Pa)
T = temperature in Kelvin
M_{mol} = molar mass (g)

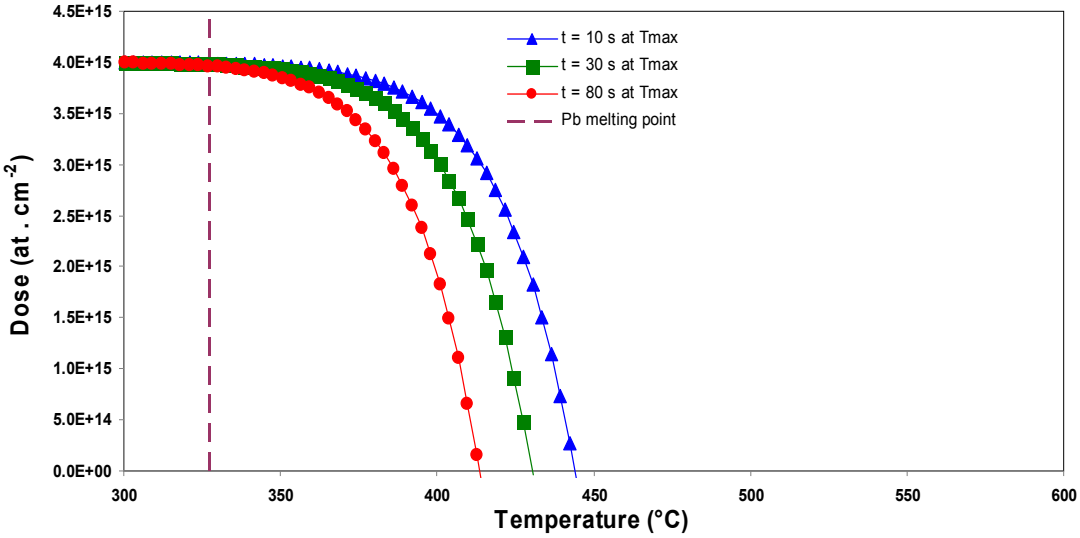

Figure 1 Calculated remaining dose of Pb in Si after annealing at T_{max} for different times, the dashed vertical line is the melting point of Pb

We can use equation (1.3) to calculate the loss of Pb and Sn from Si at different temperatures using the vapour pressure at that temperature (from [7]). For comparison with electron beam annealing the calculation can be modified to also account for atomic loss during ramping up and down and the time that the material is held at target temperature.

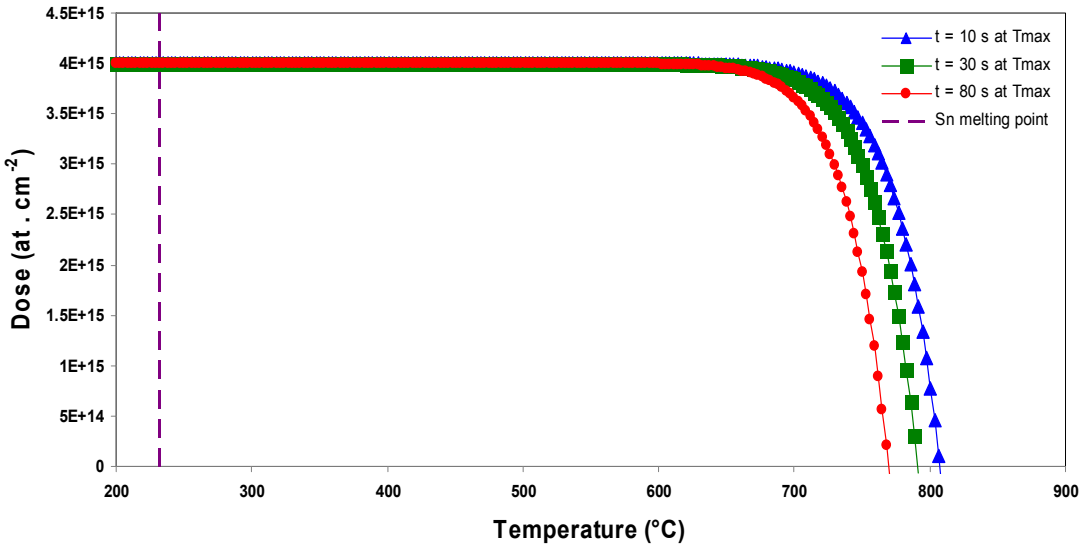

Figure 2 Calculated remaining dose of Sn in Si after annealing at T_{max} for different times, the dashed vertical line is the melting point of Sn

Starting from an initial dose of 4×10^{15} atoms cm^{-2}, Figure 1 presents the calculated remaining dose (atoms cm^{-2}) for Pb in Si after annealing over a range temperature regimes using a temperature ramp of 5°C s^{-1} and holding at the target temperature (T_{max}) for 10s, 30s, and 80s respectively.
In the case of annealing Si implanted with Sn at an initial dose of 4×10^{15} atoms cm^{-2}, Figure 2 presents the calculated remaining dose (atoms cm^{-2}) for Sn in Si after annealing over a range temperature regimes using a temperature ramp of 5°C s^{-1} and holding at the target temperature (T_{max}) for 10s, 30s, and 80s respectively.

The difference between Sn and Pb loss rates are immediately evident. Even though the melting point of Sn (211.97°C) is significantly lower than that of Pb (327.5°C), the determining factor is the vapour pressure. At room temperature, the vapour pressure of Sn is 10^{20} less than that of Pb.

Kinetic theory calculations provide a useful way of comparing expected behaviour of Si implanted substrates during the annealing process with experimentally derived results. Deviations from calculated results are likely to be explained by physical changes in the Si substrate material either by Si surface recrystallisation of the amorphous implanted area providing a barrier to diffusion of implanted atoms out of the bulk material or by inclusion of implanted atoms into the crystal lattice itself thereby forming novel nanostructured materials.

References

[1] A. Markwitz, *Low energy ion implantation into Si for novel group IV nanomaterials* 15th AINSE Conference on Nuclear and Complementary Techniques of Analysis & 10th Vacuum Society of Australia Congress, 21 – 23 November 2007 Melbourne

[2] S. Johnson, A. Markwitz, M. Rudolphi and H. Baumann, Journal of Apply. Phys. **96** (2004) 605

[3] S. Johnson, A. Markwitz, M. Rudolphi, H. Baumann, S. P. Oei, K. B. K. Teo and W. I. Milne, Applied Physics Letters **85** (2004) 3277

[4] S. Johnson, A. Markwitz, M. Rudolphi, H. Baumann, Applied Physics Letters **89** (2006) 153122

[5] A. Markwitz, S. Johnson, M. Rudolphi, H. Baumann and A. Mücklich, Applied Physics Letters **86** (2005) 013108

[6] Physical Chemistry, P W. Atkins, 3rd edition, Oxford University Press, UK, 1987

[7] CRC Handbook of Chemistry and Physics, Ed.: David R. Lide, 82nd edition, 2001-2002 (pp 4-134)

Porous titanium dioxide materials fabricated by using templating techniques

Rachel A. Caruso
PFPC, School of Chemistry, The University of Melbourne, Melbourne, Vic. 3010, Australia

rcaruso@unimelb.edu.au Phone: +61 3 8344 7146 Fax: +61 3 9347 5180

Abstract

The ability to control the morphology of materials is highly desirable as structure plays an important role in the final properties of the material. This can lead to enhancement of the performance of materials in applications due to changes in characteristics such as the accessible surface area and porosity. A study of the synthesis of titanium dioxide structures with controlled morphology will be presented. The tailoring of both outer morphology and inner porosity will be demonstrated by the use of templating techniques. Characterisation allowed the determination of bulk and intricate structural details, the crystallinity of the particles, the surface area and pore sizes of the structures and the temperatures at which crystal phase changes occurred.

Porous titanium dioxide structures have been produced using a variety of organic templates. The titania precursor, titanium isopropoxide, initially fills the pores of the template. When the infiltrated template is introduced to water hydrolysis and condensation reactions occur, resulting in an amorphous titania coating of the organic structure. The samples are dried and then calcined to achieve the highly porous titanium dioxide structures. The outer morphology is dependent on the form of the template,[1] producing for example, films, spheres or tubes (Figure 1).

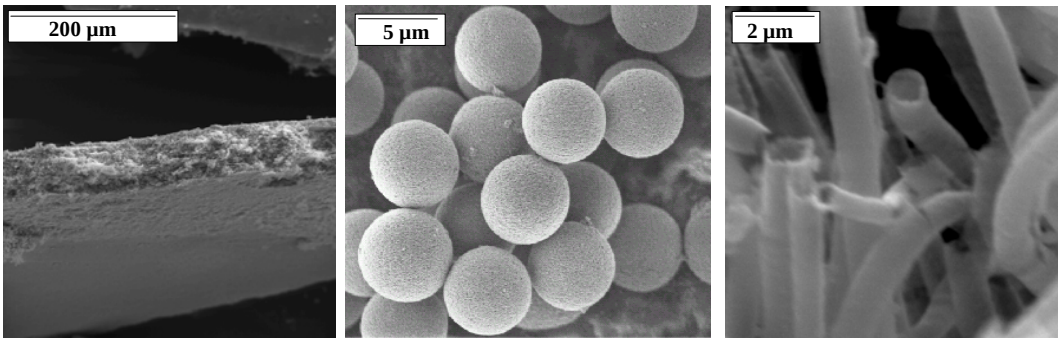

Figure 1. Titanium dioxide porous structures produced using a filtration membrane, chromatography beads or polymer fibres as templates.

The inner porosity of the titania structures is achieved by the coating of the original template with the inorganic. During the sol-gel process the amorphous titania forms at the surface of the template, leaving the open porosity of the template in the final titania structure. For example, although shrinkage occurs during the sol-gel process, the porous structure from a 2 wt % agarose gel can still be observed in the final TiO_2 material fabricated in the presence of the agarose gel template.[2] A smaller pore is also observed when the sample has been calcined to induce crystallisation of the titania. This small pore results from interparticle crevices, and is in the mesopore range when anatase nanocrystals are produced.

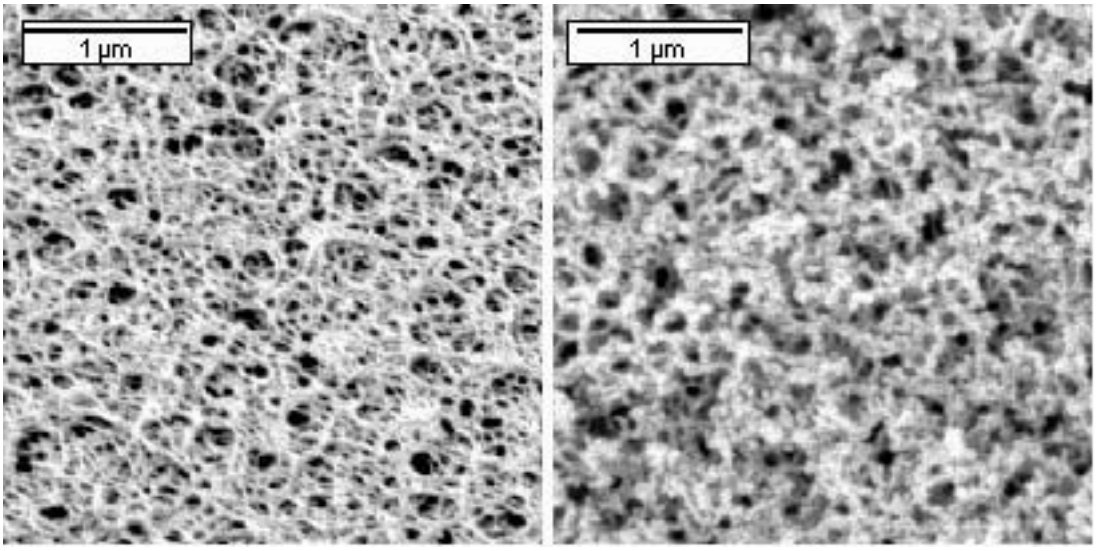

Figure 2. SEM images of the 2 wt % agarose gel and the titania structure fabricated using this agarose gel as a template.

The surface area of the porous titania structure can vary from 30 m^2g^{-1} to over $100m^2g^{-1}$ depending on the crystal size of the titania and the overall porosity of the materials produced. By introducing small quantities of a second metal oxide to the titania synthesis, leading to metal doping of the titania, the crystal phase behaviour of the material can be altered: This influences the final crystal size and therefore the surface area. For example, doping 4 wt % Al into the TiO_2 structure resulted in a decrease in crystal diameter from 30 to 20 nm, and an increase in surface area from 48 to 98 m^2g^{-1}.[3]

Titanium dioxide has a wide range of applications, including as photocatalysts and electrodes in photovoltaic cells. As many of these applications require chemical reactions or physical interactions at the surface of the titanium dioxide, an increase in accessible titanium dioxide surface area would be expected to enhance the efficiency of the materials. We are currently studying how the controlled morphology, porosity and increased surface area influence the performance of the titania materials in the photodegradation of organic pollutants in aqueous solutions, and in photovoltaic devices.

Acknowledgements

This work has received support from the ARC and AINSE Awards (AINGRA07031 and AINGRA07164).

References

1 R. A. Caruso and M. Antonietti *Chem. Mater.* 2001, *13*, 3272-3283; R. A. Caruso *Top. Curr. Chem.* 2003, *226*, 91-118.

2 J. F. Zhou, M. F. Zhou and R. A. Caruso *Langmuir* 2006, *22*, 332-336.

3 F. Z. Huang, M. F. Zhou, Y.-B. Cheng and R. A. Caruso *Chem. Mater.* 2006, *18*, 5835-5839.

Helium ion microscope – high resolution, high contrast microscopy for nanotechnology

D. J. O'Connor
School of Mathematical and Physical Sciences, University of Newcastle, NSW 2308

The Helium Ion Microscope is the marriage of a crystal tip field ionisation source and an electron microscope column to attain high resolution images of surface and interfaces. The high brightness and small spatial distribution of the field ionisation source is used to create a 20keV He ion beam which is refocused onto surfaces. The higher mass of the projectile and the nature of secondary electron emission for energetic ions leads to a potential lateral resolution of 0.25 nm though so far the best obtained is 0.8nm.

The different electron emission resulting from ions compared to electrons leads to greater contrast in secondary electron mode and it is possible to image both surface and subsurface simultaneously. In lithography applications, the incorporation of He into a surface has no chemical impact to the subsurface region compared to other ion beam etching processes.

This instrument is still under development by Carl Zeiss SMT, Inc and new features incorporating chemical identification via elastic particle scattering are expected to be part of future options.

Next generation x-ray microspectroscopy: towards full-spectral XANES and high-throughput fluorescence imaging using massively parallel detector arrays and real-time spectral deconvolution

C.G. Ryan [1,6,7], D.P. Siddons [2], G. Moorhead [3,6], G. De Geronimo [4], R. Kirkham [3], B.E. Etschmann [1,6,7,8], A. Dragone [2], P.A. Dunn [3], A. Kuczewski [2], P. Davey [3], M. Jensen[3], J.M. Ablett [2], D.X. Belton [1,6,7], J. Kuczewski [2], R. Hough [1] and D. Paterson [5]

[1] *CSIRO, Exploration and Mining, Geoscience, Monash University, Clayton VIC, Australia*
[2] *National Synchrotron Light Source, Brookhaven National Laboratory, NY, USA*
[3] *CSIRO Materials Science and Engineering, Clayton VIC, Australia*
[4] *Instrumentation Division, Brookhaven National Laboratory, Brookhaven NY, USA.*
[5] *Australian Synchrotron, Clayton VIC, Australia*
[6] *School of Physics, University of Melbourne, Parkville VIC, Australia*
[7] *CODES Centre of Excellence, University of Tasmania, Hobart TAS, Australia*
[8] *South Australian Museum, North Terrace, Adelaide SA, Australia*

Introduction

Present limits placed on synchrotron X-ray microprobe fluorescence imaging by detectors and data acquisition approaches result in poor image definition, defined as the number of pixels. The approach taken here aims to set the pixel count to suit the needs of the sample (between ~0.2-4 mega-pixels) and use a fast multi-parameter data acquisition approach, with each X-ray event tagged by X,Y position and detector number, and tight coupling with direct stage control, to accumulate full-spectral data for all pixels without imposing dwell time constraints per pixel.

The attraction of energy-dispersive detectors for imaging and trace analysis, which stems from high data-rates and full-spectral data collection, is tempered by the need to unravel the complex overlaps between interfering elemental signatures and detector artefacts, background and scattered beam. A method, called Dynamic Analysis (DA), has been developed [1] to deconvolute these overlapping signatures, which enables the elemental images to be projected successfully, even for trace elements and rare mineral phases. Moreover, the method lends itself to real-time imaging as the underlying matrix transforms can be executed on each X-ray event as it arrives.

The large dynamic range of imaging applications between major elements and trace elements at ppm levels leads to poor statistics for trace element images when a small number of detector elements are used due to the major elements setting the count rate limits in each detector. However, to improve trace element image quality means increasing the collection solid-angle of the detector system which increases overall count rates. This demands a large number of detector elements (hundreds) to maintain a manageable count rate in each detector channel and a data acquisition approach that can handle many millions of events per second.

Demands on fast scanning and high throughput data acquisition is further tested if 3D applications are to be tackled. These include X-ray absorption edge spectroscopy techniques, such as XANES imaging, and 3D fluorescence tomography. In these cases, we need to collect multiple full-spectral image frames, one for each step in E_{photon} (for XANES) or θ (for tomography).

New Detector Concept

A new spectroscopy detector system is under development by BNL and CSIRO that combines a large planar Si detector array, custom pulse-processing ASICs, and a

pipelined, parallel processor with embedded DA image projection, which aims at large solid-angle, close coupling to stage control and count-rates approaching 10^8 events/second, with full real-time processing and deconvoluted image projection [2,3]. The final concept aims for a 384 element detector array. This work reports on a series of tests using 32 and 96 element detector system prototypes.

The detector comprises low-leakage Si pad arrays under development at BNL [2], and CMOS application specific integrated circuits (ASICs) providing a 32 channel integrated low-noise preamplifier plus high order shaper with baseline stabilizer (HERMES [4]), and a 32 channel peak-detecting derandomizer and multiplexer (SCEPTER [5]) to enable time-over-threshold determination for pile-up detection and rejection. The detector pad array is wire-bonded to one or more 32 channel HERMES ASICs. The detector array (water cooled with additional Peltier cooling of the detector array to -35 °C) has demonstrated an energy resolution of 184 eV (Mn K_α).

Pulses from the SCEPTER ASICs representing both energy (E) and time-over-threshold (T) are digitized by dual 14-bit fast synchronous ADCs interfaced to the parallel processing engine HYMOD, developed at CSIRO for high speed instrumentation applications. HYMOD consists of a wide input data interface (128 bit), 166 MHz field programmable gate-array (FPGA) connected to 6 large static RAMs, a 166 MHz Motorola PowerPC co-processor, and ample fast serial (12 x 3.125 Gb/s) and Ethernet ports (2 x 1Gb/s). Code for the FPGA is developed using an in-house pipelined, parallel processing compiler called 3PL, and will handle pile-up rejection, energy calibration mapping, DA projection and directly drive the sample stage. The PowerPC handles image accumulation and display and in the final version will handle external control requests as an EPICS node. Tests of the HYMOD implementation of the DA algorithm, using a second HYMOD to simulate a detector data-source, have demonstrated event processing and real-time DA image projection at 10^8 events per second.

The DA method builds a matrix transform to perform the task of spectral deconvolution of overlapping element spectra and detector artefacts [1]. The method was developed at CSIRO to project quantitative elemental images derived from proton induced X-ray emission (PIXE) data and has been extended to handle Synchrotron X-ray Fluorescence (SXRF) data [6]. The DA approach lends itself to real-time processing of detected X-ray counts on an event-by-event basis. Each event is tagged by detector number and current XY position of the sample stage for imaging (and potentially E_{photon} for XANES and θ for fluorescence tomography). The detector number is used to select energy calibration tables appropriate for the detector to map channel number onto DA matrix column. This column provides the image increments for each elemental image at the current XY position. This close coupling of scan coordinates with data acquisition removes the common constraint of ~second dwell time per pixel, enabling high definition images to be collected with dwells of ~1 ms.

Prototype Tests

Prototype tests in late 2006 at the NSLS, beam-line X27A [8] demonstrated the concept using a 32 element prototype (called Maia-32) with the array wire-bonded to a single HERMES-SCEPTER pair. This experiment provided some illustrative examples, which featured short dwell per pixel (6 ms), mega-pixel images (up to 2000 x 2000 pixels) and real-time deconvolution into separated elemental images [7].

Recent tests in 2007 at X27A used a 96 element prototype (called Maia-96) with the array bonded to 3 HERMES-SCEPTER pairs and a faster stage. The geometry of this prototype test is shown in Fig. 3. These tests demonstrated (i) count rates up to 6 Mcps, (ii) dwell times as short as 0.8 ms (7.5 μm pixels), (iii) further mega-pixel images of geological and biological samples, which show extraordinary detail in major and trace elements (Figs. 1,2), and (iv) schemes designed to compress or filter the raw data-flow in anticipation of even higher rates with larger arrays.

Conclusions

Plans for a 384 detector system, integrating full-spectral data collection with high speed stage control and real-time data processing and image display are on track with successful tests of 32 and 96-channel prototypes at the NSLS, which featured mega-pixel imaging at dwell times as short as 0.8 ms and count rates up to 6 Mcps. Given the capabilities of the new system, the choice of pixel number and dwell time are now dictated by the needs of the applications and adequate counting statistics and not by data acquisition limitations.

Acknowledgements

We acknowledge financial support from the Access to Major Research Facilities Programme, which is a component of the International Science Linkages Programme established under the Australian Government's innovation statement, Backing Australia's Ability, and through the CSIRO Emerging Science Initiative in Synchrotron Science. Research carried out (in whole or in part) at the National Synchrotron Light Source, Brookhaven National Laboratory, which is supported by the U.S. Department of Energy, under Contract No. DE-AC02-98CH10886.

References

[1] C.G. Ryan, "Quantitative Trace Element Imaging using PIXE and the Nuclear Microprobe", *Int. J. Imaging Systems and Technology*, 11 (2000) 219-230.

[2] D.P. Siddons, R.H. Beuttenmuller, P. O'Connor, A.J. Kuczewski, Z. Li, Proc. of SRI-2003, San Francisco, August, 2003, *AIP Conference Proceedings* 705 (2004) 953.

[3] C.G. Ryan, D.P. Siddons, G. Moorhead, R. Kirkham, P.A. Dunn, A. Dragone, G. De Geronimo, "Large detector array and real-time processing and elemental image projection of X-ray and proton microprobe fluorescence data", *Nucl. Instr. Meth.* B 260 (2007) 1-7.

[4] G. De Geronimo, P. O'Connor, R. H. Beuttenmuller, Z. Li, A. J. Kuczewski, and D. P. Siddons, "Development of a High-Rate High-Resolution Detector for EXAFS Experiments", *IEEE Trans. Nucl. Sci*., 50 (2003) 885-891.

[5] A. Dragone, G. De Geronimo, J. Fried, A. Kandasamy, P. O'Connor and E. Vernon, "The PDD ASIC: Highly Efficient Energy and Timing Extraction for High-Rate Applications", *IEEE Nuclear Science Symposium Conference Record* 2 (2005) 914-918.

[6] C.G. Ryan, B.E. Etschmann, S. Vogt, J. Maser, C.L. Harland, E. van Achterbergh and D. Legnini, 2005, "Nuclear Microprobe – Synchrotron Synergy: Towards Integrated Quantitative Real-time Elemental Imaging using PIXE and SXRF", *Nucl. Instr. Meth.* B 231, 183-188.

[7] D. P. Siddons, A. Dragone, G. De Geronimo, A. Kuczewski, J. Kuczewski, P. O'Connor, Z. Li, C. G. Ryan, G. Moorhead, R. Kirkham, P. Dunn, "A High-speed Detector System for X-ray Fluorescence Microprobes", proc. of the 2006 IEEE Nuclear Science Symposium, Medical Imaging Conference and Room Temperature Semiconductor Detector Workshop, San Diego, October 29 - November 4, 2006.

[8] J.M. Ablett, C.C. Kao, R.J. Reeder, Y. Tang, A. Lanzirotti, *Nucl. Instr. Meth*. A562 (2006) 487.

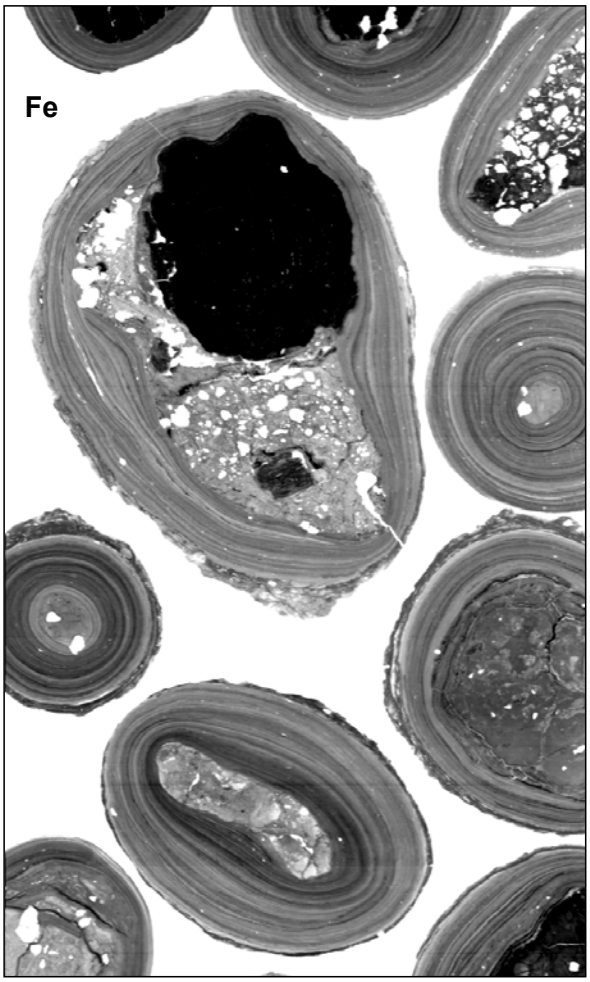

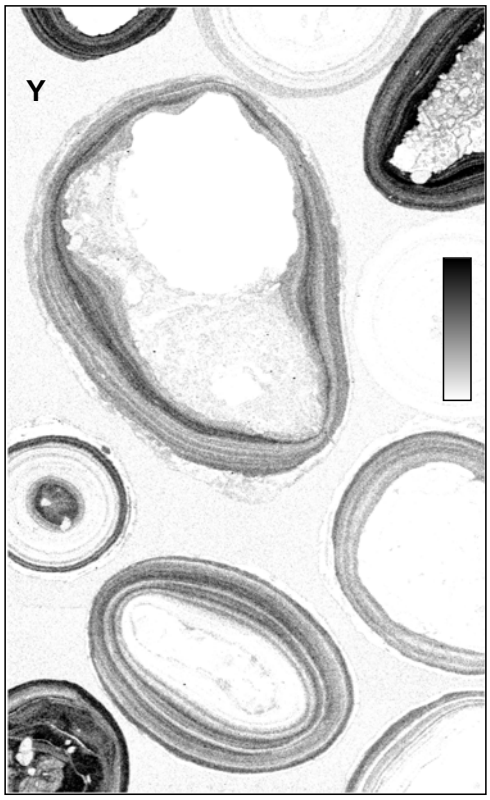

Fig. 1 Fe (left), Y (above) in iron-oxide nodules, Rose Dam, WA, imaged using the Maia-96 prototype detector array, NSLS beam-line X27A [8], 17.2 keV photons, 13 x 21 mm^2, 1625 x 2625 pixels at 5 ms/pixel.

Fig. 2 (right) Ca in stems of *Acacia Aneura* from Western Australia, imaged using the Maia-96 prototype detector array, beam-line X27A, 17.2 keV photons (9 x 17 mm^2; 1200 x 2267 pixels at 7.5 ms/pixel)

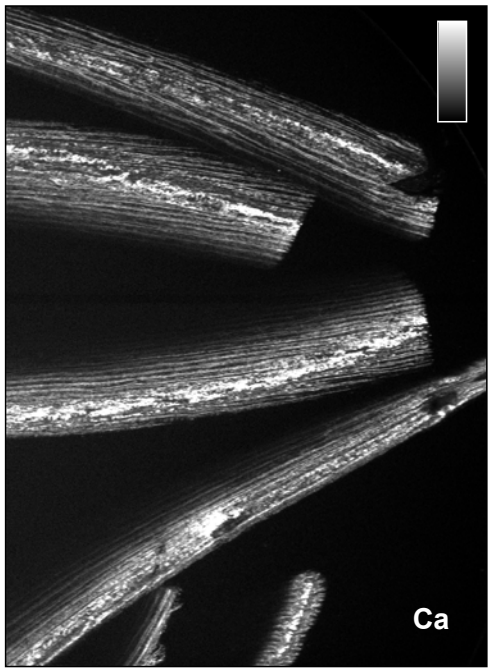

Fig. 3 (below) Layout of the 96 element detector (detector at 90° to the beam, target rotated -45°), showing its solid-angle at 20 mm from target. The final 384-element detector array will have 6-7 times larger effective solid-angle.

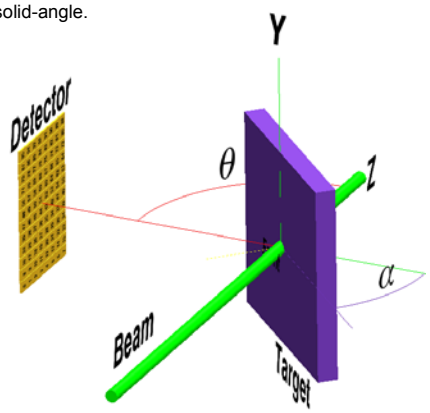

Extended interface analysis using high energy electron scattering

M R Went and M Vos
Atomic and molecular physics laboratories, RSPHYSSE, ANU, Canberra 0200.

Abstract

We demonstrate that high-energy, high-resolution reflection electron energy loss spectroscopy (REELS) can provide unique insights into interface formation, especially for the case where an extended interface is formed. By changing the geometry and/or electron energy the electronic structure is probed over a range of thicknesses. Simultaneously the elastically scattered electrons are resolved into different components, corresponding to scattering of atoms with different mass. Thus these high-energy REELS/elastic scattering experiments obtain information on both atomic composition and the electronic structure of the overlayer formed.

Introduction

Reflection energy loss spectroscopy (REELS) has long been used to study the interaction of electrons with a surface, and is an important tool to help understand photoemission, as the latter necessarily involves the transmission of electrons from the material under investigation into the vacuum. In this paper we present REELS spectra taken at energies up to 40 keV. As the mean free path of electrons increases with energy this allows us to probe rather thick layers. Here we want to demonstrate that high-energy REELS can be used as an in-house technique to study the electronic structure of thick layers. It is in this sense an alternative to high-energy photoemission, and is a method that could quite easily be adapted to even higher energies.

Interest in investigating the possibilities of these high-energy REELS measurement was triggered in part by the realization that the elastic peak splits up at high energies in different components, corresponding to electrons scattering of atoms of different mass [1]. This is because if an electron is scattered over a large angle, it transfers a significant amount of momentum to the scattering atom. If the momentum transferred to the atom is **q**, then the corresponding (mean) recoil energy E_r, transferred from the electron to the atom is given by $E_r=q^2/2M$, with M the mass of the atom. Thus, in favourable cases, the elastic peak splits up into different components, due to scatterers with different mass M and the measured structure can be used to determine the surface composition. This technique is then often referred to as 'electron Rutherford backscattering' (ERBS) (see e.g. [2]), as it resembles (ion) Rutherford backscattering in many ways. REELS at high energies provides complimentary information to ERBS, mainly on the electronic structure, that is obtained simultaneously with ERBS data.

Experimental details

The main spectrometer is shown in Fig. 1. The spectrometer is equipped with two electron guns. Each gun emits electrons with 500 eV energy. The sample is surrounded by a high voltage sphere kept between 4.5 keV and 39.5 keV. Thus electrons with energies between 5 keV and 40 keV are scattered from the sample. After being decelerated and focused by a slit lens stack, the electrons enter a hemispherical analyser. At the exit of the analyser a two-dimensional detector was used allowing electrons in an energy window of ≈30 eV to be detected simultaneously. For more details about the apparatus design see Refs. [3] and [4].

Data were taken with current less than 1 nA. Typically a spectrum was obtained over a 2-hr period. Samples were prepared in a separate UHV chamber by sputtering using Xe^+ ions. Auger spectra taken after cleaning revealed no C or O at the surface. The sample was then transferred under UHV to the main spectrometer for the high-energy REELS measurements. Later aluminium was deposited onto the cleaned (Mo and Pt) surface by thermal evaporation from a boron carbon nitride composite crucible. This was performed in a dedicated evaporation chamber.

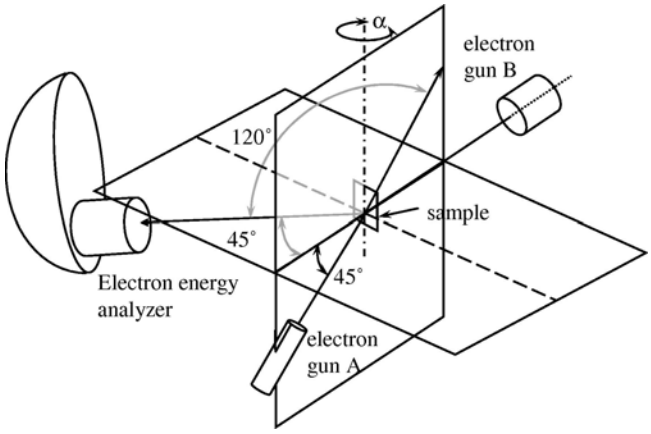

Fig. 1. An overview of the experimental configuration. If gun A is used the sample is positioned as shown and the scattering angle is 120°. Angle between the sample surface normal and incoming and outgoing trajectories is then 45° (but surface normal, incoming and outgoing trajectories are not in the same plane). If gun B is used (scattering angle 45°) the sample is rotated over angle α by 112.5°. The incoming and outgoing trajectories are now more glancing (both 67.5° with the surface normal).

Results and Conclusion

We want to investigate if we can use REELS for overlayer–substrate systems. In REELS one measures the energy distribution of the electronic excitations for an electron backscattered from a material. This distribution is a signature of the electronic structure. In a substrate–overlayer system one can identify two or more phases (overlayer, substrate and possibly one or more phases formed at the interface), each with its own electronic structure and hence loss function. By monitoring the structures of the loss function as a function of overlayer thickness we can probe which phases are present in the sample.

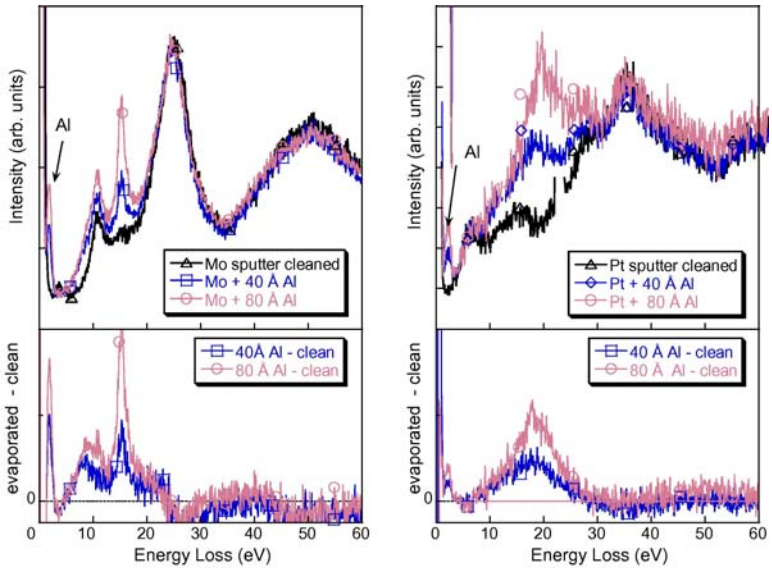

Fig. 2. A comparison of the raw (40 keV) REELS data obtained for Al deposition on Mo and Pt. For the Mo case the Al plasmon is clearly visible at the lowest coverage. However for Pt this is not the case. The difference between the high-energy spectra before and after deposition (lower panels) resembles the Al loss function in the case of deposition on Mo, but is completely different for deposition on a Pt sample . The structure appearing after evaporation near 2 eV energy loss is the Al elastic peak.

The simplest overlayer-substrate system is one where no reaction occurs, and the evaporated layer grows in a layer-by-layer mode. From the work of Kolaczkiewicz et al. it is known that Al grows (at low coverages) on Mo in a layer-by-layer mode [5].

We show spectra of Mo covered with thick (by electron spectroscopy standards) Al layers (40 Å and 80 Å) (Fig. 2). The spectra were, for convenience, normalized in such a way that they largely overlap for large energy loss values. For the Mo substrate the main effect of Al deposition is a sharp peak at 15.2 eV energy loss relative to the Mo elastic peak. 15.2 eV corresponds to the Al plasmon energy and this feature is thus attributed to electrons scattering from Mo for which either the incoming or outgoing electron excited an Al plasmon. The main features of the Mo energy loss spectra are still discernable. Thus the measured energy loss spectra for the Al/Mo system can be described, at least in first-approximation, as the sum of a Mo REELS spectrum and an Al REELS spectrum. Taking the difference of the spectra before and after Al deposition we see that the excess intensity corresponds to the energies of the Al bulk and surface plasmon.

The behaviour of Al deposition on Pt contrasts strongly with that seen for Al deposition on Mo. The Al-Pt system is known to form a surface alloy for thin layers at room temperature [6]. Our Pt results are shown in the right panels of Fig. 2. Now no sign of the Al plasmon is found. Above 30 eV energy loss and below 10 eV energy loss the features of the Pt loss function still stand out. From the difference spectrum it is clear that the excess intensity is centred around 20eV energy loss in a much broader peak (in comparison to the Al plasmon width). Increasing the coverage increases the difference before and after deposition, but the position and width of the peak in the difference spectrum does not change dramatically. We take the difference to be the rough shape of the loss function of an interface compound that is formed.

At very small energy loss (≈2 eV) an additional peak appears after Al deposition in the 40 keV REELS spectra. It is due to electrons scattering elastically from Al, rather than Pt or Mo. This additional peak appears at the recoil energy (E_r) predicted for Al. Thus it is attributed to a feature of the ERBS spectrum, not an additional inelastic energy loss feature. This Al peak appears, for identical coverage, more intense for evaporation on Mo, compared to that on Pt. This is not surprising as the Pt elastic cross section is much larger than the Mo elastic cross section, and the ERBS signal strength is, at least in first order, proportional to the elastic cross section (as all detected electrons have been scattered elastically). Hence the relative strength of the Al peak after 40 Å and 80 Å deposition is larger for the Mo substrate compared to the Pt substrate.

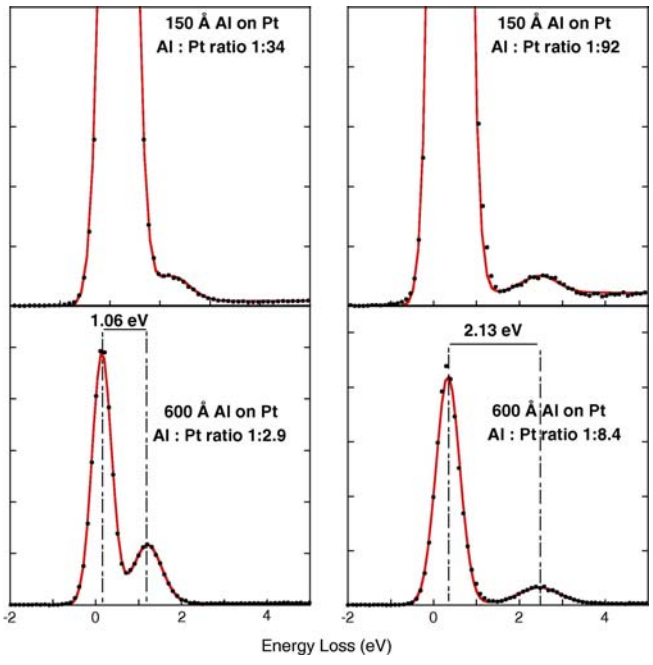

Fig. 3. Elastic region of the spectra taken at 150 Å and 600 Å Al coverage taken with gun A using a 20 keV (left panels) and a 40 keV (right panels) electron beam. The full line is a fit using two Gaussian peaks and a Shirley background. The main peak was aligned with the calculated recoil energy of Pt under these conditions.

To now investigate the ERBS signal we examine the region near the elastic peak in Fig. 3 we show the 150 Å and 600 Å cases as an example. At 150 Å coverage it is possible to get a good fit using two Gaussians separated by the calculated difference in recoil energy. However the area obtained from these fits depends very much on the background choice (we used a Shirley background for these fits). The situation has changed at 600 Å. Not only has the Al signal strength increased, but the Pt signal has become weaker due to attenuation in the Al layer (the latter is evident from the decrease of the total count rate in the elastic peak area for a given beam current). Now the peak separation can be left free in the fit, and indeed values very close to those calculated for the recoil energies are obtained, further confirming our interpretation of this feature at low energy losses. This also suggests that the single-scattering approximation is valid, ie the electrons are deflected over a large angle by one collision only. The relative intensity of the Al peak in the 20 keV measurement is stronger than in the 40 keV case, as at lower energy attenuation in the Al layer is stronger, and the thickness of the Pt layer that contributes effectively to the elastic peak is less.

We have described high-energy reflection electron energy loss experiments and confirm that these experiments are bulk-sensitive. Interfaces formed by evaporation of Al on the substrates were monitored by REELS over a large range of overlayer thicknesses using a range of energies. In this way one can vary the depth probed, and the picture obtained in this way gives clear insights in extended interface formation. Besides the dramatic changes in the REELS spectra it was found that deposition of Al on high *Z* substrates results in a splitting of the elastic peak, due to recoil effects. In general, the spectra are all very dependent on the electron energy, but, at least qualitatively, the spectra can be interpreted as the sum of the bulk loss functions of the materials that contribute (overlayer, substrate and reacted layer). Changes due to energy variations are then a simple consequence of a variation in probing depth. Hence it is clear that REELS at high energies is often a very convenient way of probing surface elemental composition as well as the electronic structure up to considerable depth (≈1000 Å in favourable cases). A prerequisite for this method is that the energy loss spectra of the overlayer and substrate have well-resolved distinguishing features.

[1] M. Vos, *Phys. Rev. A* **65** (2002), p. 12703.

[2] M. Went and M. Vos, *Appl. Phys. Lett.* **90** (2007), p. 072104.

[3] M. Vos, G.P. Cornish and E. Weigold, *Rev. Sci. Intrum.* **71** (2000), p. 3831.

[4] M. Vos, V. Sashin, C. Bowles, A. Kheifets and E. Weigold, *J. Phys. Chem. Solids* **65** (2004), p. 2035.

[5] J. Kolaczkiewicz, M. Hochol and S. Zuber, *Surf. Sci.* **247** (1991), p. 284.

[6] K. Wilson, J. Brake, A.F. Lee and R. Lambert, *Surf. Sci.* **387** (1997), p. 257.

Avalanche detector technology for keV single ion detection and implantation for quantum bits construction

C. Yang [1], D.N. Jamieson [1], T Hopf [1], E. Gauja [2], A.S. Dzurak [2] and R.G. Clark [2]

[1] *ARC Centre of Excellence for Quantum Computer Technology, School of Physics, University of Melbourne, Victoria 3010, Australia*

[2] *ARC Centre of Excellence for Quantum Computer Technology, University of New South Wales, Sydney 2052, Australia*

Abstract

Avalanche photodiode (APD) technology offers high sensitivity in the detection of visible light and x-rays based on the high internal charge gains. It is ideal for the measurement of ionization energies with very high sensitivity. It can potentially be used for the detection of single low-energy-heavy ion particles at keV energy range, especially for the detecting and controlling of 5-10 keV P^+ single ion implantation events for the construction of Si:P based quantum bits. We used the method of ion-beam-induced-charge (IBIC) to investigate the internal charge gain and charge collection efficiency (CCE). We achieved a charge gain larger than 300 in commercial APDs through the IBIC measurement using MeV He^+ ions. A special detector structure is outlined for counting keV single ion implantation events aiming for the construction of Si:P based quantum bits (qubits) and single-donor nano-devices.

Keywords: Avalanche photodiodes (APD), ion-beam-induced-charge (IBIC), charge collection efficiency (CCE), internal charge gain, ionization energy, keV single ion implantation, qubits, nano-devices

Introduction

We have established a single-ion-implantation method for the qubits construction based on the ionization energy measurement of single ion induced charge in silicon through using PIN detector structure [1-4]. The on-going project is aiming for the improvement of the detection limit of the ionization energy measurement by adapting the APD detector technology for the keV single ion detection.

APDs are conventionally configured to work in non-linear Geiger mode in most optical applications. The Geiger mode is for an operation with a maximum gain; the drawback is impossible to tell and reject pile-up events. The work presented here we successfully operated APD detectors in a linear mode with an output of signal pulse height linearly proportional to the ionization energy of the incident particles; this gave us an advantage of being able to distinguish single ion events from two or multiple ions pile-up events. We used the method of ion-beam-induced-charge (IBIC) to measure the internal charge gain and charge collection efficiency (CCE). We observed a strong correlation of internal charge gain with the ions implantation depth in avalanche detectors with a charge gain larger than 300 in commercially available APDs. An avalanche-PIN design structure is outlined for counting keV single ion events aiming for the construction of Si:P based qubits and single-donor nano-devices.

IBIC characterization of single ion detectors

IBIC imaging method in a nuclear Microprobe was applied in the characterization of the detectors. This IBIC method was previously used for a prototype of PIN detector's optimization aiming for keV single ion detection [5]. The PIN detector structure and

its typical IBIC map revealing the charge collection efficiency is displayed in the Figure 1. The PIN detector has constant charge collection efficiency 100% at the device's centre area with a wide range of bias voltages. The IBIC analysis was also applied to a selected commercial APD detector with increased bias voltages up to 160 V. Figure 2 displays a uniform CCE map indicating a charge gain of 2.0 with a bias voltage of 95 V. A structural defect was also evident in the CCE map. A further effort will be focused on modifying an existing PIN device by introducing an avalanche zone into the detector design for achieving a large internal charge gain (>1). IBIC analysis on the new devices will provide key information on the internal charge gain of the future avalanche-PIN (APIN) devices.

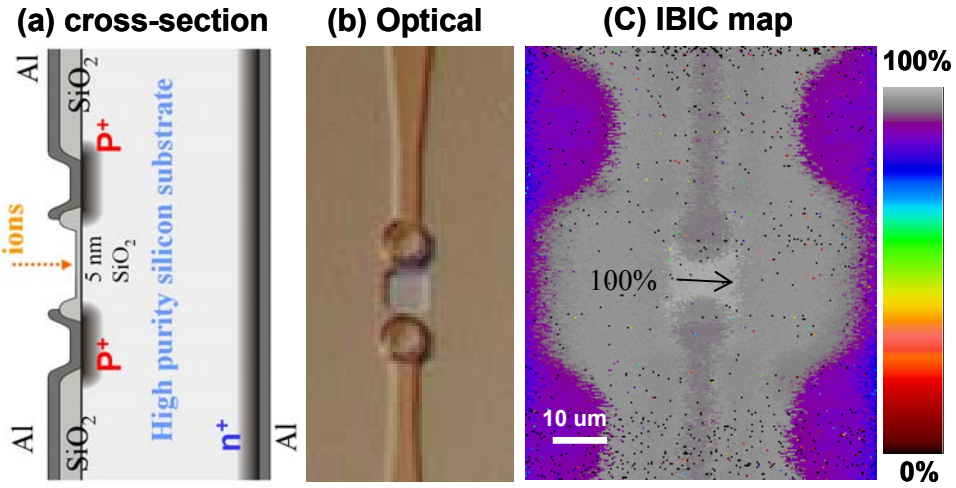

Figure 1. A prototype of PIN detectors used for keV single phosphorus ion implantation. (a) Cross-section of the PIN structure; (b) a micro-photographic image; (c) CCE map obtain by IBIC showing charge collection efficiency of 100% at the centre of the device.

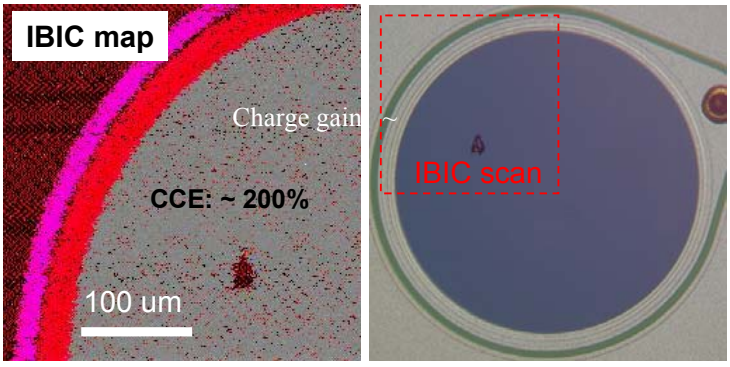

Figure 2. IBIC analysis of an APD device. 0.5 MeV He^+ ion beam was used in the IBIC analysis. The device was biased at 95 V.

Large charge gain for single ions in APD devices

We used MeV He^+ ion to measure the charge gain. The charge gain in the **commercial** APD detector is a strong function of the bias voltage. IBIC analysis using 2.0 MeV He^+ ions was applied to the APD with bias voltages scanned from 10 to 160 V. The result of the charge gain versus bias voltage is displayed in Figure 3. The internal charge multiplication process was evident at a bias voltage above 60 V. The charge gain reaches above 10 at bias voltage of 150 V and larger than 300 at bias voltage above 155 V.

Construction of APIN device for Single ion implantation

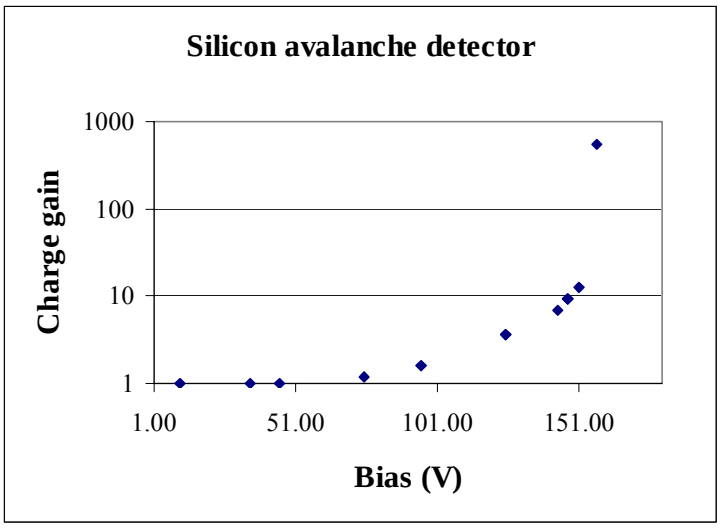

Figure 3. Internal charge gain versus bias voltage. The charge gain reaches 10 at 150 V and a few hundred at above 155 V.

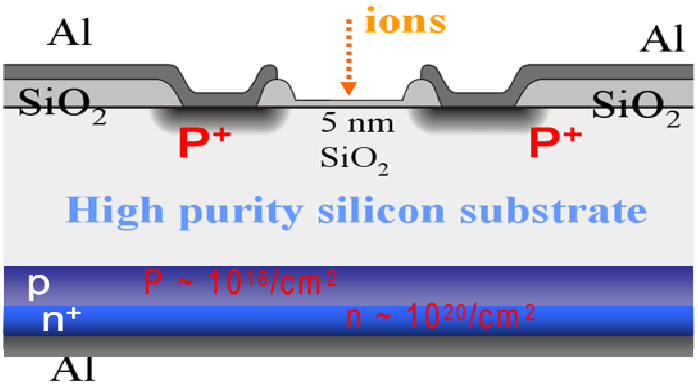

Figure 4. Construction of APIN detectors based on an existing PIN structure. An avalanche zone may be constructed at the backside of the device.

It is not feasible to use commercial APDs for the single ion implantation application due to its metal coating and impurity doping at the device's frontal area. We have developed a prototype of PIN detectors for the keV single ion implantation. It is possible to construct an avalanche zone at the backside of this type of PIN device for achieving a large internal charge gain. Figure 4 displays a layout of a proposed avalanche-PIN structure for the single ion implantation application.

Acknowledgements

This work was supported by the Australian Research Council, the Australian Government and by the US National Security Agency (NSA), Advanced Research and Development Activity (ARDA) and the Army Research Office (ARO) under contracts W911NF-04-1-0290.

References

[1] D.N. Jamieson, C. Yang, T. Hopf, S.M. Hearne, C.I. Pakes, S. Prawer, M. Mitic, E. Gauja, S.E. Andresen, F.E. Hudson, A.S. Dzurak, and R.G. Clark. Applied Physics Letters, 86, 202101 (2005).

[2] R.G. Clark and et al., Philosophical Transactions of the Royal Society of London A 361, 1451(2003).

[3] S.E. Andresen, R. Brenner, C.J. Wellard, C. Yang, T. Hopf, C. Escott, R.G. Clark, A.S. Dzurak and D.N. Jamieson and L.C.L Hollenberg, Nano Letters 7, 2000 (2007).

[4] C. Yang and et al., *Jpn J. Appl. Phys.*, 2003, 42 (6B), 4124-4128.

[5] Changyi Yang and et al., Proc. SPIE 5650, 64 (2005), Volume 5648, Smart Materials III.

Towards a better understanding and prediction of the bremsstrahlung background in PIXE spectra

David D. Cohen, Ed Stelcer, Michael Prior, Rainer Siegele and Mihail Ionescu
ANSTO, PMB1, Menai, NSW, 2234, Australia.

Abstract

Murozono and Ishii et al recently published theoretical QFEB, SEB and AB bremsstrahlung cross sections which, when modified by typical X-ray detection efficiencies, provide excellent predictions of the backgrounds in PIXE spectra for a range of light target matrices.

Introduction

MeV ions impinging on solid targets produce bremsstrahlung radiation. For MeV ions on light to medium atomic numbered targets this radiation has at least three components; quasifree electron (QFEB), secondary electron (SEB) and atomic bremsstrahlung (AB)[1-4]. The QFEB process is represented schematically in Fig. 1. A target electron is scattered by the Coulomb field of the projectile producing bremsstrahlung x-rays. The cross section becomes large when the projectile velocity

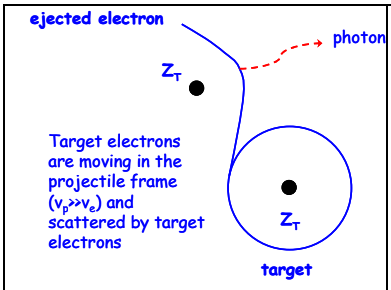

Fig. 1. Schematic QFEB

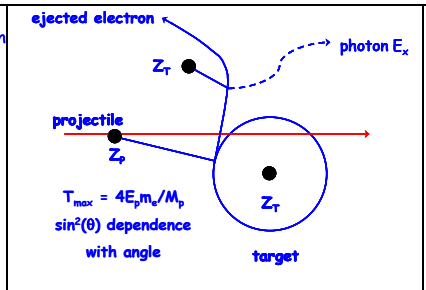

Fig. 2. Schematic SEB.

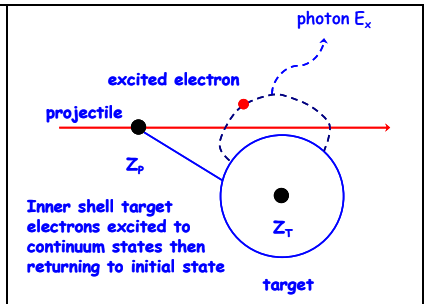

Fig. 3. Schematic AB.

is much larger than the target electron velocity. The maximum energy transferred to the electron at rest is [T_r=m_eE_p/M_p]. The SEB radiation is produced when the projectile ejects a target electron which is then scattered by the Coulomb field of another target nucleus. This process is shown in Fig. 2.

The maximum energy transferred to the target electron in this SEB process is [T_m= $4T_r$= $4m_eE_p/M_p$]. The final bremsstrahlung process we consider here is AB shown in Fig. 3. This occurs when a bound target electron is excited to the continuum, by the projectile and then returns to its original bound state. This results in a continuous spectrum from a few eV to tens of keV depending on the bound state of the electron. Following Murozono et al [4] we only consider K and L shell bound states here. Typical cross sections for 3MeV protons on carbon for these three

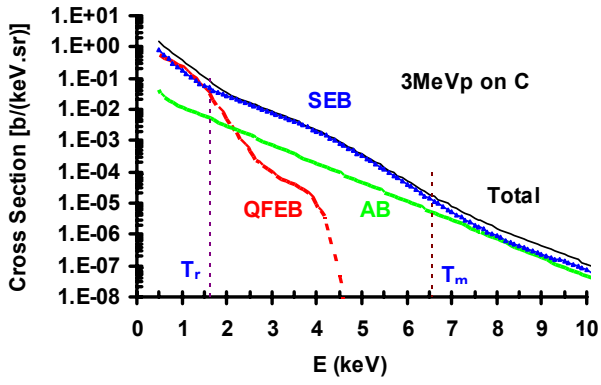

Fig. 4. Typical cross sections for QFEB, SEB and AB processes for 3 MeV protons on carbon after Murozono et al [4].

mechanisms are shown in Fig. 4. The QFEB process is significant below 2keV, SEB dominates the total bremsstrahlung cross sections from 2-8keV and AB becomes significant above 8keV x-ray energies. For 3MeV protons on carbon T_r=1.6 keV and

T_m=6.5keV which is reflected well in the cross section fall off in the QFEB and SEB data of Fig. 4 (see vertical dashed lines). These bremsstrahlung cross sections are monotonic and continuous with X-ray energy and increase significantly with decreasing energies below 10 keV.

Particle Induced X-ray Emission (PIXE) experiments [5,6] are generally performed using 3MeV protons on carbon like matrices with silicon based detection systems. Fig. 5 shows the calculated detection efficiency for a typical Si(Li) detector with 25µm beryllium entrance window thickness and two different crystal dead layer thicknesses of 0.1µm and 0.5µm [7]. Discontinuities are produced in the detection efficiency at the Si K edges and the gold contact M edges as shown [8].

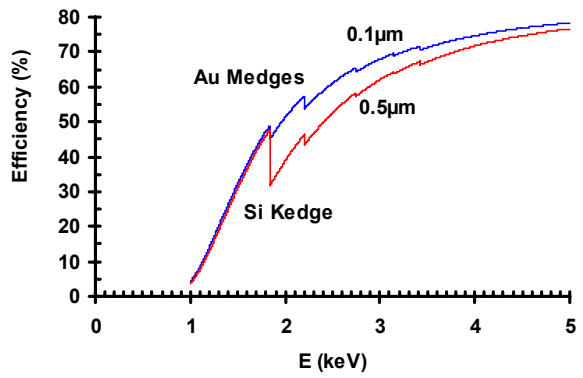

Fig. 5. Typical efficiency for a Si(Li) detector with 25 µm thick beryllium entrance window and dead layer thicknesses of 0.1 and 0.5 µm, after Cohen [7].

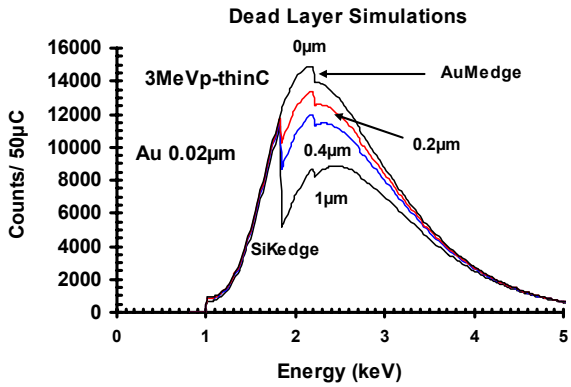

Fig. 6. Bremsstrahlung yield simulations for different dead layer thicknesses for 3 MeV protons on 2.7 mgcm^{-2} thin carbon.

The drop in efficiency from 100% above 10 keV to less than 1% at 1 keV folds the cross section plots of Fig. 4 over below 2 keV, producing the classic measured PIXE bremsstrahlung shapes shown in the simulations of Fig. 6 for 3 MeV protons on thin carbon. The discontinuities at the Si Kedge and the gold contact layer M edges have been used by Cohen et al [8] to estimate the detector silicon dead layer and the gold contact layer thicknesses.

Bremsstrahlung Yields

Scaling the QFEB, SEB and AB cross sections of Murozono et al [4] and convoluting their sum over the 0-15keV X-ray energy region with the detection efficiencies of Cohen [7] we can calculate the total bremsstrahlung yields for different ions on selected targets. Fig. 7.

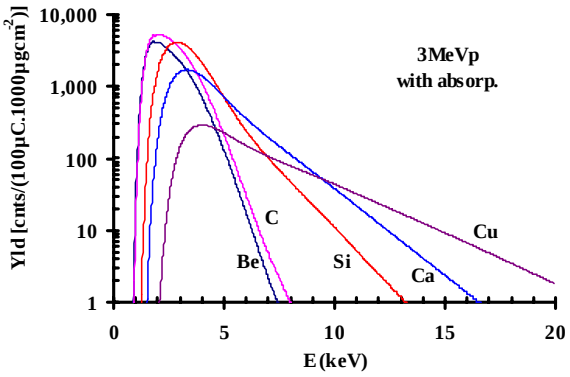

Fig. 7. Calculated bremsstrahlung yields for 100 µC of 3 MeV protons, using a detector with 80 µm Be window and solid angle of 1.3msr. All targets were 1,000 µgcm^{-2} thick.

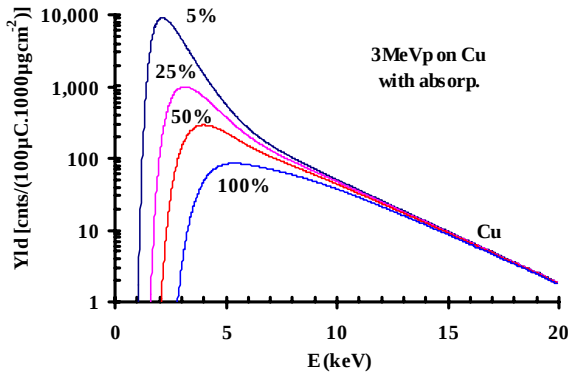

Fig. 8. The variation in bremsstrahlung yields with target self absorption, using 5%, 25%, 50% and 100% of the target thickness for self absorption corrections on a Cu target.

shows such a calculation for 100µC of 3 MeV protons on 1,000 µgcm^{-2} Be, C, Si, Ca and Cu targets. Note the target thickness is much less than the proton range. These yields have been corrected for detection efficiency and self absorption of 3 MeV protons for all targets. As the target atomic number Z_2 increases the X-ray yields increase in the 7-20 keV region. The peak in the bremsstrahlung shifting from 2 keV for Be to 4 keV for Cu targets is produced by self absorption in the target. This is clearly demonstrated by Fig. 8 where yields for 3 MeV protons on 1,000 µgcm^{-2} thick Cu are plotted as a function of the percentage depth at which the self absorption was calculated. Self absorption shifts the low energy cut off and the apparent peak in the yield to higher X-ray energies as the size of the correction increases with depth.

We have measured bremsstrahlung yields from a range of pure thin targets including Be and C. Fig. 9 shows such yields for 200 µC of 2, 3 and 4 MeV protons on 1,767 µgcm-2 thick carbon. For proton energies above 2.2 MeV on carbon an additional Compton scattered gamma ray background component appears in the spectrum above 10 keV. This can be adequately fitted by an exponential function in X-ray energy and subtracted off, leaving the pure bremsstrahlung component, between 0 and 10 keV, see Cohen et al [9].

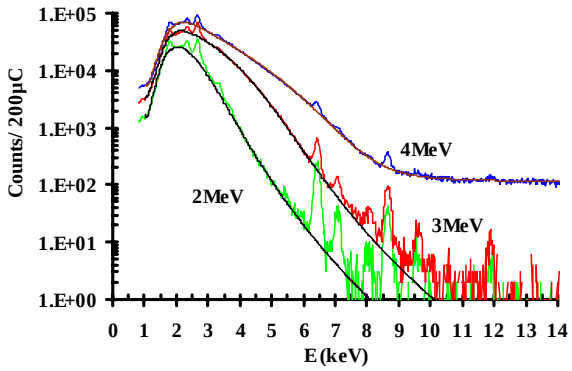

Fig. 9. Experimental yields for 2, 3 and 4 MeV protons on 1767 µgcm^{-2} thick carbon.

The solid curves of Fig. 9 show the background shapes of these PIXE spectra were well fitted by the bremsstrahlung plus gamma ray backgrounds calculated above. Indeed Figs 10 and 11 show that this technique for bremsstrahlung prediction can be used to fit thin targets for compounds as well as pure elements. Fig 10 is the PIXE spectrum for 2.6MeV protons on thin Teflon. The Teflon was relatively very pure and hence the spectrum well represents bremsstrahlung background. The flat continuous background above 10keV was due to Compton scattered gamma rays from F(p,p'γ) reactions and was well fitted by an exponential function in x-ray

energy all the way down to zero keV. The solid curve under the experiment between 1 and 9 keV was the predicted bremsstrahlung background for (CF_2) Teflon with only one extra parameter for scaling its peak height to fit the experiment between 2 keV and 3 keV. Closer inspection shows a good fit to the experimental shape, with significant deviation only above 4 keV where the AB component maybe underestimated by theory.

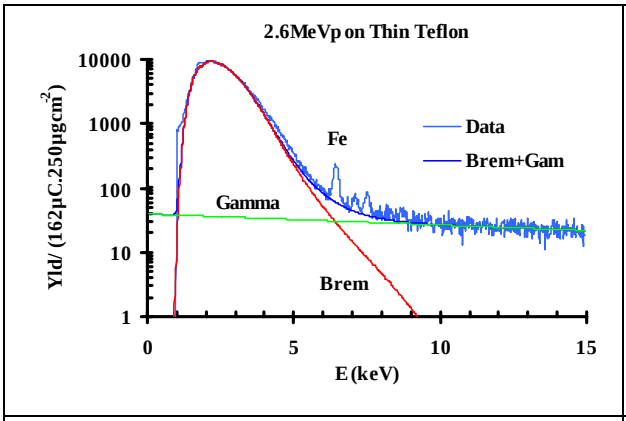

Fig. 10. Comparison of experimental and theoretical bremsstrahlung backgrounds for 2.6 MeV protons on 250 µgcm^{-2} Teflon $(CF_2)_n$ target.

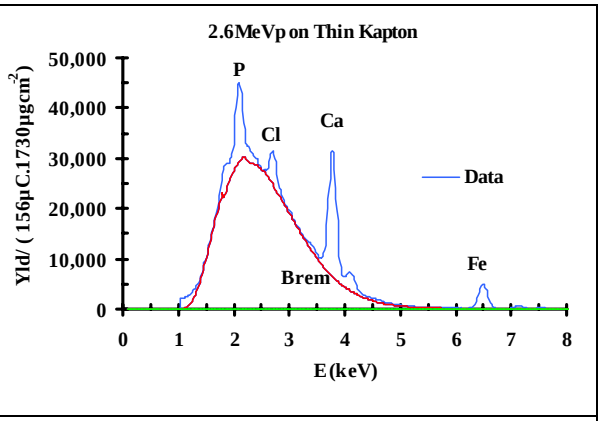

Fig. 11. Comparison of experimental and theoretical bremsstrahlung backgrounds for 2.6 MeV protons on 1730 µgcm^{-2} Kapton $(C_{22}H_{10}N_2O_5)_n$ target.

This may be expected since the AB contributions calculated by Murozono et al [4] only included the K and L shell target electrons and only transitions from these levels to the continuum and back to the K or L shell. Whereas one might expect transitions from inner shell target levels to the continuum (Radiative Ionisation, RI) may also contribute in this X-ray energy region [2]. The excess counts in this region may be due to pileup of the bremsstrahlung radiation with itself although experimental count rates were kept low so that dead time corrections were typically well below 5% for most runs.

Fig. 11 is a similar plot to Fig. 10 except for thin Kapton $(C_{22}H_{10}N_2O_5)_n$, this was plotted on a linear scale so the background fit below the characteristic peaks for P, Cl K and Fe could be better assessed. Again the fit was excellent with the only fitting parameter being a single scaling factor to match theory and experiment in the 3 keV region where there were no characteristic X-ray peaks.

Summary

Theoretical QFEB, SEB and AB cross sections have been used to estimate the experimental bremsstrahlung backgrounds found in typical thin target PIXE spectra of pure elements for proton energies between 1 and 4 MeV. This has been extended, again with good results, to compounds containing lighter elements like carbon, oxygen, nitrogen and fluorine. If the Compton scattered gamma ray background was simulated with an exponential function in X-ray energy, then the total background for most common PIXE spectra were successfully modelled from first principals. These concepts can now be included into standard PIXE analysis codes like PIXAN [10,11], GUPIX [12,13] and GeoPIXE [14].

Acknowledgements

We would like to acknowledge the help of the 2 MV STAR accelerator staff in several aspects of this work. This work was partly performed within the framework of IAEA CRP G.4.20.02 Unification of nuclear spectrometries.

References

[1] F. Folkmann, C. Gaarde, T. Huus, K. Kemp, Nucl. Instr. Meth., 116 (1974) 487-499.

[2] K. Ishii, S. Morita, Nucl. Instr. Meth., B22 (1987) 68-71.

[3] K. Ishii, Radiation Physics and Chemistry, 75 (2006)1135-1163.

[4] K. Murozono, K. Ishii, H. Yamazaki, S. Matsuyama, S. Iwasaki, Nucl. Instr. Meth., B150 (1999) 76-

[5] S. A. E. Johannson and J.L. Campbell, ″PIXE: A Novel Technique for Elemental Analysis″, Wiley and Sons, New York, 1988.

[6] D. D. Cohen and E. Clayton, "Ion Induced X-ray Emission" in "Ion Beams for Materials Analysis", eds.J. R. Bird and J.S. Williams (Academic Press, Sydney, 1989) Chap 5.

[7] D. D. Cohen, Nucl. Instr. Meth., 178 (1980) 481-490.

[8] D. D. Cohen et al, submitted to X-ray Spectrometry 2007.

[9] D. D. Cohen et al, submitted to Nuclear Instr. Meth., 2007.

[10] E. Clayton, D. D. Cohen and P. Duerden, Nucl. Instr. Meth., B22 (1987) 64.

[11] D. D. Cohen and E. Clayton, Nucl. Instr. Meth., B22(1987)59.

[12] J. A. Maxwell, J. L. Campbell, W.J. Teesdale, Nucle Instr. Meth. B43 (1989) 218.

[13] J. A. Maxwell, W.J. Teesdale, J. L. Campbell, Nucle Instr. Meth. B95 (1995) 407.

[14] C. G. Ryan, D. R. Cousens, S. H. Sie, W. L. Griffin, Nucl. Instr. Meth. B49 (1990) 217.

Fully-automated counting of fission tracks in natural minerals for fission track dating and thermochronology

Andrew J.W. Gleadow [1], Stewart J. Gleadow [1], Barry P. Kohn [1] and Michael S. Krochmal [3]

[1]*School of Earth Sciences, University of Melbourne, Melbourne, Victoria 3010, Australia*

[3]*Autoscan Systems Pty Ltd, PO Box 112, Ormond, Victoria 3204, Australia*

The automated counting and analysis of fission tracks in natural minerals has been one of the most long-sought goals in fission track dating. But despite extensive exploration of possible approaches, and some promising developments [eg 1-3], essentially all attempts up to this time have failed in one or more key aspects. There are specific challenges and difficulties to be overcome in the automated image analysis of spontaneous fission tracks in natural minerals. These include discriminating genuine tracks from non-track defects, resolving multiple track overlaps, and identifying small tracks in a background of similar-sized spurious features, such as surface dust particles and fluid inclusions. The optical variability of individual grains of natural minerals also poses challenges for digital image analysis systems that are inherently poor at pattern-recognition tasks compared to the eye and brain combination of a human operator. Developments in computing have largely solved other problems of image quality, lack of sufficient computing power, and of sufficient image storage.

Rapid advances in optical microscopy, such as confocal laser scanning microscopy, have so far had little impact on the imaging of etched fission tracks in minerals. Notwithstanding claims to the contrary [4], confocal microscopy has little benefit for the imaging of fission tracks because it remains inherently a reflected light technology at the present time. Some individual fission tracks are revealed superbly, but others are made almost invisible by this observation mode. This situation is not likely to change until a truly transmitted light confocal imaging system is developed. However, these developments have led to the emergence of a new generation of microscope control systems that now enable the acquisition of digital microscope images of unprecedented quality using conventional imaging modes in transmitted and reflected light.

Our digital image acquisition system is based on a Zeiss Axiotron microscope with motorized stage and focus mechanism, motorised objective nosepiece and light source shutters. All of the main microscope configuration functions are thus under computer control. To this set-up a Physik Instrumente PIFOC piezoelectric microscope-objective nanofocussing device has been added for the 100x objective. The PIFOC device is capable of positioning the objective lens with sub-nanometer resolution over a total scanned range of 100 μm with near-instantaneous response and no mechanical backlash. The motorised stage and focus motor are used for preliminary positioning of the specimen to previously-labelled points of interest. The PIFOC device is then used for precise control of focussing and highly stable image acquisition using an Olympus ColorView 1 CCD digital microscope camera with 3.3 megapixel resolution. Our procedure captures a surface-focussed reflected light image followed by a precisely spaced Z-stack series of images in transmitted light. This image series is then archived to disk before processing using a custom developed image analysis system based initially on the ImageJ cross-platform image analysis program. All custom software has been written in Java to maximise its cross-platform implementation.

We first concentrated attention on the problem of automating the fission track counting and our initial attempts centred on using the information in a Z-Stack sequence to resolve the problem of multiple track overlaps. Various approaches for projecting and analysing the Z-Stack were tried and, whilst some of these produced potentially useful information on track dimensions, they were processor intensive and most were ineffective at resolving overlaps. Our attention then turned to utilising the information in the reflected light image and from this we have developed a remarkably simple digital image analysis system that solves most of the typical track recognition and discrimination problems encountered in routine fission-track analysis in natural minerals.

We have called the method 'Coincidence Mapping' and it involves combining the reflected light image with a single transmitted light image, as shown in Figure 2. The transmitted and reflected light images (Figure 1, (a) and (b) respectively) are segmented by applying a custom developed thresholding routine to give the binary images of features (c) and (d). Inspection of Figure 1 shows that both kinds of binary images include spurious features that are not tracks. However the intersection of these two images obtained using a Boolean AND operation selects for the genuine track features and against spurious objects. The coincidence map, Figure 1(e), shows the selected features and (f) the rejected features from this analysis. The analysis is extremely efficient and takes only a few seconds to complete the analysis of images that may contain hundreds of tracks. Figure 1 illustrates fission tracks etched in a muscovite external detector but experience so far shows that the discrimination obtained with this method is also highly effective for counting spontaneous fission tracks in apatite.

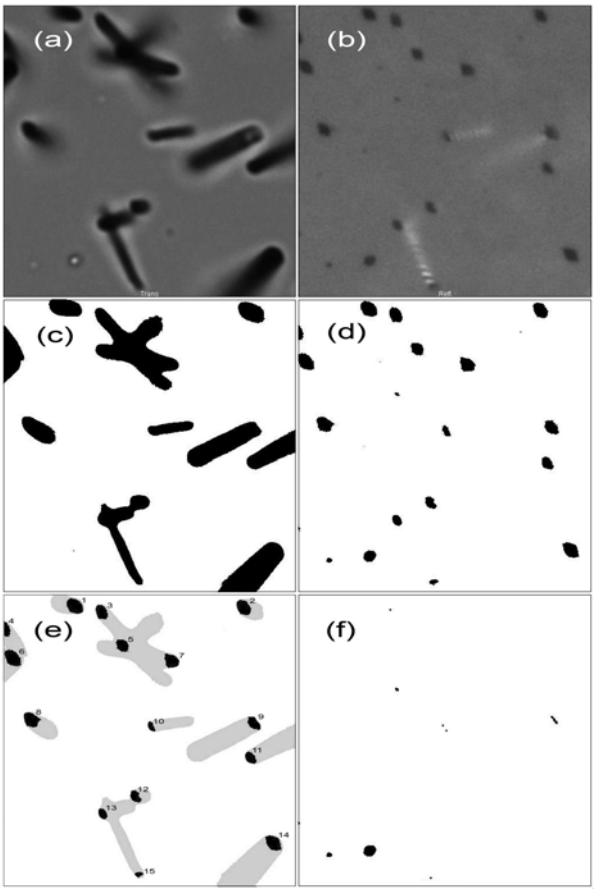

Figure 1. Image analysis sequence of fission tracks in muscovite mica showing (a) transmitted light image, (b) reflected light image, (c) thresholded binary image of tracks in transmitted light, (d) thresholded binary image of tracks in reflected light, (e) the coincidence map showing the 15 counted tracks in black, being the overlap between the two binary images, superimposed on a grey image of the transmitted light tracks and (f) spurious features rejected by the analysis. The counted fission track features are shown as black spots with adjacent identification numbers in (e)

The method is extremely effective at discriminating tracks from surface dirt and dust, polishing scratches, microlites and fluid inclusions. It is also remarkably effective at resolving multiple track overlaps even at track densities well beyond that which a human operator would normally attempt. The system achieves this success in resolving overlaps by capturing the higher spatial resolution of the track entrance pits

in the reflected light image. At even higher track densities, where the reflected light pits themselves begin to overlap, we have used an analysis of the areas of the individual pit features to resolve the number of tracks represented by larger compound track features. In this way we have successfully been able to count track densities up to 5x107 cm-2, well beyond the range that is normally countable in transmitted light by a human operator. We see no reason why this method should not work effectively up to track densities as high as 108 tracks cm-2. The error rate in our experimentation so far is about the same or better than that achieved by a human operator counting in transmitted light. At high track densities the error rate is significantly lower.

We are now very confident that coincidence mapping will provide the first successful image analysis system for the fully-automated counting of fission tracks in natural minerals. Automated counting should significantly improve data quality in fission track dating through better counting statistics, measurement of additional track description parameters not currently collected, and increased objectivity in fission track analysis. The technique is extremely fast and promises a much more rapid sample throughput than can be achieved by a human operator. Combined with direct-uranium determination by laser-ablation ICP-MS [5], coincidence mapping will provide a revolutionary new approach to fission track dating. Automated measurement of track lengths is a more challenging problem that is not yet resolved, although several promising leads are being investigated.

Acknowledgements

We gratefully acknowledge the financial support provided to this project through a Linkage Project Grant from the Australian Research Council with Autoscan Systems Pty Ltd as an Industry Partner.

References

[1] Belloni FF, Keskes N, Hurford AJ, 2000. Strategy for fission-track recognition via digital image processing, and computer-assisted track measurement. (Abstract) 9th International Conference on Fission-Track Dating and Thermochronology, *Geological Society of Australia Abstracts* 58, 15-17.

[2] Petford N, Miller JA and Briggs J. 2003. The automated counting of fission tracks in an external detector by image analysis. *Computers and Geosciences* 19, 585-591.

[3] Wadatsumi K, Masumoto S, 1990. Three-dimensional measurement of fission-tracks: Principles and an example in zircon from the Fish Canyon Tuff. *Nuclear Tracks and Radiation Measurements* 17, 399-406

[4] Petford N and Miller JA, 1990. SLM confocal microscopy: an improved way of viewing fission tracks. *Journal of the Geological Society of London*, 147, 217-218.

[5] Hasebe N, Barberand J, Jarvis K, Carter A and Hurford AJ, 2004. Apatite fission-track chronometry using laser ablation ICP-MS. *Chemical Geology* 207, 135-145

PIXE imaging of a developing corrosion front beneath a protective coating on galvanized steel

David X Belton [a], David N. Jamieson [b], Chris G. Ryan [a], Aaron K. Neufeld [c]
aCSIRO Exploration and Mining, Melbourne, VIC, Australia
bSchool of Physics, MARC, University of Melbourne, VIC, Australia
cBlueScope Steel Limited, Coatings Research, Port Kembla, NSW, Australia

Abstract

Despite their wide application in construction and manufacturing, unprotected metals are largely unsuited to applications where they are exposed to moisture and potentially corrosive agents. This has led to the development of engineering solutions such as pre-painted galvanized steel strip and sheet, which combines chemical and mechanical protection against aggressive environments. However, if the integrity of this barrier is compromised, then the structural element – in this case the steel – may be exposed to progressive and irreversible deterioration leading ultimately to failure of specific performance criteria. In this paper we used the CSIRO-GEMOC nuclear microprobe to investigate in-situ, the nature of chemical reactions at the interface between the outer paint coating and the underlying hot-dipped galvanized layer in a specimen that has been exposed to extreme marine atmospheric conditions. By using 3 MeV protons, we were able to penetrate the outer paint coating, the underlying zinc plating, and the steel substrate below. The combination of layers acted to attenuate the X-ray yields from the Fe-rich substrate while permitting abundant counts from Cl-rich corrosion product compounds and dehydrated electrolyte beneath the paint coating to be detected with only a 125μm Be filter. We present a series of elemental images showing spatially, in extraordinary detail the physical degradation of the paint coating and the effects of corrosion processes.

Keywords: x-ray imaging, corrosion, galvanized steel, PIXE, nuclear microprobe

1. Introduction

Zinc coating is an economical means of protecting steel from the ravages of exposure to the elements. Galvanized steel products resist corrosion in two fundamentally different ways [1]. First, the zinc plating provides a mechanical barrier that prevents exposure of the steel substrate to moisture and potentially aggressive environments. Secondly, zinc acts as an active coating that provides sacrificial or galvanic protection. Modern protection of hot-dip zinc galvanized (HDG) steel products includes a paint coating which provides exceptional resistance to corrosion [2]. However, the finished coating may be damaged either during installation, or subsequently when the material is in use. If the integrity of the barrier system is compromised the steel may deteriorate and ultimately fail. HDG steel coated with an inferior paint or with imperfections, is susceptible to blistering when exposed to a corrosive ambient. Blistering is initiated by cathodic processes at the interface between the paint coating and the zinc layer. Chlorides form here through the corrosion of zinc in the area of the delaminated blister, and if the underlying steel is exposed, additional oxidation of zinc is introduced. The crucial property of zinc is that under these circumstances, it protects the steel from oxidation.

The spatial distribution of the elemental products and reactants provides clues to understanding of corrosion initiation [3] and allows us to better define the key characteristics of an effective paint coating. However, obtaining chemical information

about corrosion reactions buried beneath the paint topcoat (typically >25 μm) is a challenge, since removal of the coating without disturbing the elemental composition and distribution within the corrosion zone is rarely successful. [4]

Nuclear microprobe analysis provides a method for capturing high resolution images of spatial variation in composition without the removal of the paint coating. The ion beam can penetrate through the topcoat to allow Proton Induced X-ray Emission (PIXE) from the "buried" steel substrate, the galvanized zinc layer and the corrosion product compounds. The arrangement of the layering in these samples coincidentally ensured that high X-ray yields resulting from both the Fe-rich and Zn-rich layers were sufficiently attenuated by the intervening paint coating. Use of a 125μm Be filter ensured optimum yield of easily attenuated Cl and Si X-rays.

2. Experimental Method

Panels of prepainted HDG steel sheet were exposed to a severe marine environment for 3 years. During this period, physical imperfections in the paint coating and poor wet adhesion between the zinc layer and the paint coating have formed the initiation points for blistering corrosion. For analysis using the CSIRO-GEMOC Nuclear Microprobe, a sample 1 cm in diameter was cut from the panel. Using the optical microscope capabilities of this microprobe, the scan region was readily positioned over a blister which presents as a distinctive feature resulting from corrosion product build-up under the paint coating. The scan region was selected to image both undamaged and blister regions of the sample. X-ray data for the sample was collected with a Canberra UltraGe X-ray detector fitted with a 125 micron Be filter. The ~1.8 micron, 3 MeV H^+ beam at 0.1 nA was rastered in the Y-direction and the sample stage stepped in the X-direction to achieve a total scan of approximately 4 mm^2. Routine procedures are available within the GeoPIXE software package [5] to determine elemental concentrations from the raw spectra in the undamaged zone.

Layered targets require more detailed treatment to allow for the variation in composition with depth. Nevertheless, it is possible to image, in extraordinary detail, the transition from undamaged to the corroded zinc-paint coating interface whilst leaving the entire multilayer sample intact. For this investigation, we were primarily interested in the reduction of the zinc layer and the chloride distribution. However, regions of poorly constrained thickness (eg. the blister) meant that the PIXE spectrum did not provide sufficient information to model a complete analysis of a multi-compositional, layered specimen. To address this, a suite of experiments using progressively milled (removed) paint coating were conducted to characterise the response of both Zn and Fe X-rays to varying thicknesses of overlying material.

3. Results and Discussion

The organic-rich paint coating is characterised by Si, K, Ti and Cr. The X-ray element map for Ti is reproduced in Figure 4. TiO_2 is used to optimise a whole range of paint properties including colour, opacity, dispersion and durability [6]. With the exception of some small artefacts introduced by the combination of irregularities in the sample surface and the detector geometry (the detector is located to the right of the scan area at 135^o to the beam), the concentration of Ti (and Si, K, Cr) is essentially unvarying over the entire element image. One can infer that the paint coating has not suffered significant wear nor chemical decomposition and thus does not appear to participate as a reactant in the corrosion process.

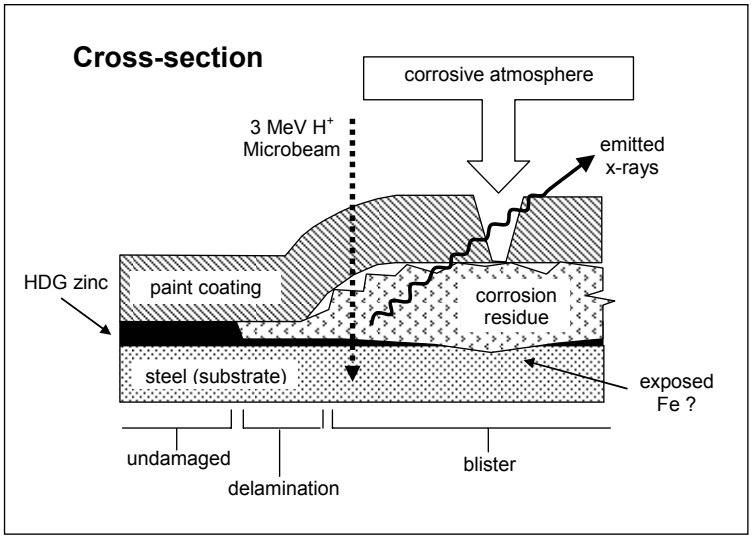

Figure 1: Schematic of the corrosion growth process following a breach in the paint topcoat of hot-dip galvanized steel substrate exposed to a corrosive ambient. The 3 MeV H^+ ion beam is able to penetrate the ~25 micron topcoat and induced X-rays from the elements of interest (Cl and heavier) emerge through the topcoat to be detected.

In contrast, zinc in the HDG layer represented by the element map (Fig. 4) shows a number of features in both the undamaged and corroded regions, not all of which are related to the corrosion reaction. Cl (Fig. 4) is present under the paint coating in the form of corrosion product compounds and dehydrated electrolyte. A first order comparison of the Cl and Zn element maps highlights the significant lowering of Zn X-ray yield in those regions where Cl is present. With higher energy x-rays such as Zn (Kα - 8.64KeV), this reduced yield cannot be explained by attenuation in a modest thickness of corrosion products between the paint coat and an unaffected zinc layer. Modelling in GeoPIXE indicates that within the region of early de-lamination (Fig 1) characterizing the corrosion front, the loss of Zn yield is consistent with a reduction in thickness of the HDG layer on the order of 1.2 μm.

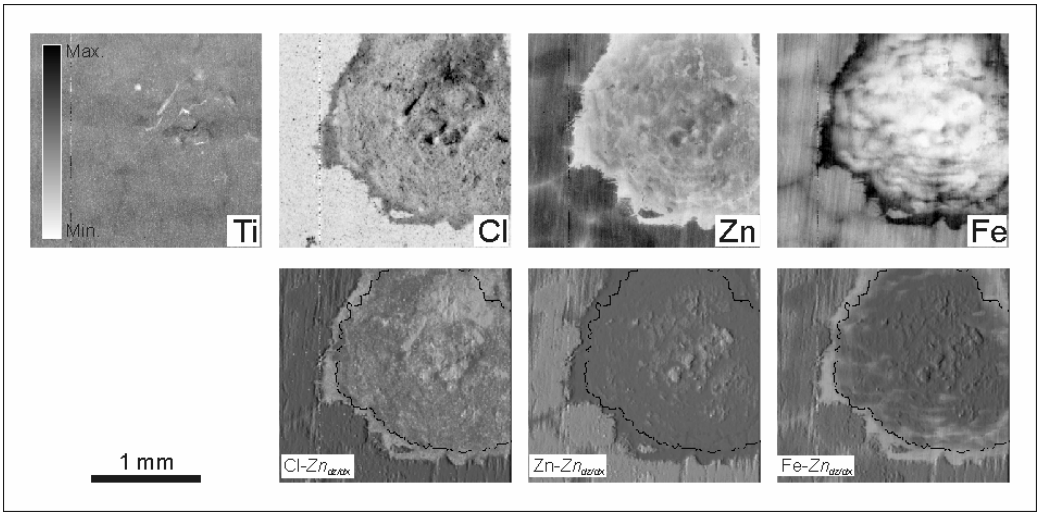

Figure 2: Elemental maps (Ti, Cl, Zn, Fe) of the propagating corrosion front obtained from the characteristic X-ray peaks. Corrosion propagated radially from the approximate centre of the scan region. Note the presence of a sub-vertical fabric in the Zn and Fe images, unrelated to the scan direction (see the single faulty scan line in the Cl image). The lower images are element maps draped over a derivative image generated from the Zn map [7] and highlight the some of the element relationships.

Zinc-hydroxychlorides are formed by oxidation of zinc in aggressive marine atmosphere. Thus, a reduced thickness of zinc will generate a marked drop in Zn X-ray yield in the region coincident with the Cl element map. However, estimates of Zn loss using GeoPIXE are hampered by the variable and irregular thickness of the Cl-rich precipitate. Note that Cl appears in the element maps ahead of the external blister margin (Fig. 2) and may indicate that the maximum extent of delamination of the paint coating. Beyond this interface, Cl is absent. There are narrow zones of reduced Zn yield that might suggest the development of cellular features in the Zn. Enhanced Fe yields observed in Figure 4 would support thinning of the Zn in these areas. Since these regions do not generally coincide with the presence of Cl, it may be inferred that they are unrelated to the corrosion process and the cellular structure may be a result of the hot-dip galvanizing process.

Fe X-ray yields (Fig. 2) from within the steel substrate are sensitive to the amount of absorption represented by the overlying HDG zinc and paint layers (and the Cl-rich precipitate where present). Reduction of the zinc layer by the corrosion reaction generates enhanced Fe yields. The increase in Fe X-ray yield is most emphasised in the boundary zone where delamination has occurred but where there is insufficient space to precipitate large quantities of X-ray absorbing corrosion products such as those seen in the centre of the blister. GeoPIXE analysis, and modelling of varying paint coatings in our test samples, suggests that the variation in Fe yields in the boundary zone can be explained by variations in the thickness of the overlying materials (primarily Zn loss) with no loss of the steel substrate itself.

4. Conclusions

Nuclear Microprobe analysis can be used to rapidly investigate the distribution of key elements in the corrosion reactants and products normally obscured beneath a protective paint coating in layered substrates. For pre-painted, hot-dip zinc galvanized sheet, the layered construction permits high precision analysis over the element range Cl to Zn with minimal filtering to avoid detector saturation. The resultant x-ray element maps can be processed using established image analysis techniques which enable us to generate powerful interpretive images and our “layer thickness” experiments will further constrain quantification within the corroded regions. Characterization of the intact corrosion reaction assemblage through the topcoat using the nuclear microprobe provides a superior method for identifying the structure and spatial distribution of the corrosion reaction products. Precise determination of the spatial relationships between reaction components without disturbing the material is crucial for a deeper understanding of the mechanisms behind the corrosion reaction.

References

[1] Technical bulletin (2003) *CTB-1 Corrosion*, BlueScope Steel Ltd, Australia
[2] Technical bulletin (2003) *CTB-7 Barrier Coatings*, BlueScope Steel Ltd, Australia
[3] K. Neufeld et al. (2002) *Corrosion Science* 44, 555-572.
[4] Symanski et al. (2002) *Nucl. Instr. and Meth. B190*:365-369.
[5] G. Ryan (2000) *Int. J Imaging Systems and Tech.*, 11: 219-230.
[6] Gambogi (1996) Titanium*, Mineral Information*, USGS.
[7] Rasband (2006) *ImageJ 1.37i* National Inst. Health, USA.